Characterizing Hydrodynamic Interactions of Underwater Vehicles in Close Proximity Using an Identical Ellipse Pair

by

Preston W. Rhodes

Submitted to the Department of Mechanical Engineering
in partial fulfillment of the requirements for the degree of

Master of Science in Mechanical Engineering

at the

MASSACHUSETTS INSTITUTE OF TECHNOLOGY

June 2023

Author .....
Department of Mechanical Engineering
May 12, 2023

Certified by .....
Wim M. van Rees
Assistant Professor
Thesis Supervisor

Accepted by .....
Nicolas J. Hadjiconstantinou
Chairman, Department Committee on Graduate Theses

Characterizing Hydrodynamic Interactions of Underwater Vehicles in Close Proximity Using an Identical Ellipse Pair

by

Preston W. Rhodes

Submitted to the Department of Mechanical Engineering
on May 12, 2023, in partial fulfillment of the
requirements for the degree of
Master of Science in Mechanical Engineering

Abstract

The hydrodynamic interactions between two identical 6:1 ellipses in close proximity were investigated using a 2D immersed interface method simulator in a viscous, rotational flow at $Re = 1500$. Interactions in tandem, side-by-side, and staggered arrangements were characterized based on changes to the drag, lift, and yaw moment coefficients experienced by the ellipses. The drag and lift results agreed with existing studies of 2D cylinders performed in subcritical flow regimes. The drag interactions were divided into five regions based on changes to the individual ellipses and the overall system. The lift was repulsive and, for the closest parallel configurations, up to four times the value of drag. An overtaking maneuver was investigated by introducing a relative velocity between the ellipses. When both ellipses were moving, the lift was repulsive throughout the maneuver. The mean drag of the slower ellipse was mostly unaffected; although the largest instantaneous drag increase reached 2.5 times that of an isolated ellipse at the highest relative velocity, this was matched by a similar drag decrease in the second half of the maneuver. The drag of the faster ellipse was relatively unaffected by the overtaking maneuver. When one ellipse was stationary, the lift transitioned from repulsive to attractive as the moving ellipse passed the stationary ellipse. The stationary ellipse experienced a significant increase in mean drag at higher overtaking speeds, reaching more than half the value of an isolated ellipse moving at $Re = 1500$. Its lift also changed significantly and was similar in magnitude to the drag. The overtaking ellipse experienced a three-to-four-fold increase in mean drag at all speeds, a thirty-fold increase in peak drag at the highest speed, and a mean lift similar in magnitude to the mean drag. The findings of this study can be used to inform fuel-efficient swimming configurations for underwater vehicles traveling in formation, as well as to increase safety when maneuvering in close proximity.

Thesis Supervisor: Wim M. van Rees
Title: Assistant Professor

Acknowledgments

I would first like to thank my advisor, Wim van Rees, and the members of his lab group for their guidance and support over the course of this research project. Their time, dedication, and shared passion for computational fluid dynamics have helped to make this experience academically and professionally enriching from start to finish. I would also like to thank the many other wonderful people I have met and worked alongside during my time as a graduate student. I will cherish the camaraderie, friendship, and encouragement I felt from these people for years to come. Last but certainly not least, I would like to thank the friends, family, teachers, and mentors who have helped me each step of the way, including long before I ever set foot in Cambridge. I am truly grateful to have such wonderful people in my life, whether they be near or far.

THIS PAGE INTENTIONALLY LEFT BLANK

Contents

THIS PAGE INTENTIONALLY LEFT BLANK

List of Figures

THIS PAGE INTENTIONALLY LEFT BLANK

List of Tables

THIS PAGE INTENTIONALLY LEFT BLANK

Chapter 1

Introduction

Unmanned underwater vehicles (UUVs) are used for a range of tasks in research, industry, and the military for which it is costly, difficult, or impossible to use humans. Examples of UUV missions are seafloor surveying, exploration, and underwater surveillance. In many cases, multiple UUVs are used simultaneously on missions to improve overall payload, widen survey coverage area, or increase redundancy. On any mission, the duration of UUV operations is limited by battery life, a large proportion of which is spent on propulsion. Reducing hydrodynamic drag on the UUV(s) is therefore of primary importance. The drag of a UUV can be reduced by using a more hydrodynamically efficient hull, but this requires the UUV to be reconfigured or redesigned, which is not always a practical option for the operator. When multiple UUVs are operating in close proximity, an alternative option is to employ a hydrodynamically efficient swimming formation with the aim of saving fuel for one or all of the UUVs in the formation. This option offers the possibility to reduce the drag on one or multiple UUVs during a mission, without any changes to their individual design.

Formation drag reduction is used in a range of applications to improve propulsive efficiency. In nature, dolphin and whale calves often make use of drag-advantaged swim formations [13; 21]. By swimming in certain positions relative to its mother, the calf experiences a decrease in hydrodynamic drag, leading to a reduction in swimming effort as much as 90 percent [30]. Hydrodynamic drafting has also been studied in

fish schooling – although it should be noted that fish schooling is primarily motivated by safety against predators rather than swimming efficiency, and there is no clear consensus on whether fish schooling does [29; 3] or does not [14] produce an actual drag benefit to individuals or the group. Formation drag reduction is also a topic of interest in land-based applications by humans such as cycling [4] and auto racing [19], with a common goal of improving speed and reducing energy expenditure for one or multiple individuals in the formation.

Knowledge of hydrodynamic interactions in UUV formations is desirable because it allows operators to coordinate UUVs to travel in formations that reduce the drag of one or multiple UUVs, and to avoid formations that increase the overall drag of the formation or that increase risk of collision. The hydrodynamics of two UUVs operating in tandem have previously been modeled using numerical simulations and laboratory testing, revealing that UUV interactions can be either beneficial or harmful to overall drag depending on the formation [17; 35; 25]. The desire to increase UUV hydrodynamic efficiency via coordinated swimming formations served as one of the primary motivations for this study.

In addition to drag, it is also desirable for operators to understand the lateral (lift) forces and yaw moments acting on UUVs. These effects are greater when UUVs move in close proximity to each other and threaten to redirect the UUVs away from their course and/or cause a collision. Lift and moment interactions between vessels can also change depending on the position of the UUVs relative to each other. Therefore, if the UUVs are in close proximity (e.g., to reduce drag), it is also important to know the lift forces and moments that will occur at each position so that the UUVs can be steered accordingly.

Previous studies have investigated the lift forces and yaw moments on bodies in a constant formation (zero relative motion). Drag and lift interactions between identical 2D cylinders were reviewed by Zdravkovich [34] and more recently Sumner [23]. The lift force was found to peak when the cylinders were positioned side-by-side; one study measured a repulsive lift of up to $C_L = 0.56$ ($T/D = 0.20$), compared to zero for an isolated ellipse [1; 23]. Other studies that assumed zero relative motion

were performed in 3D, such as Tian et al. [25], who simulated two identical UUVs and found an attractive side-force coefficient of $C_L = 0.014$ at the closest spacing ($y/L = 0.27$) when the UUVs were positioned side-by-side. A study of different-sized UUVs, Zhang et al. [35], found a yaw moment coefficient of $C_M = \pm 0.0015$, peaking when the smaller UUV was half a body length forward or aft of the larger UUV. A division existed between the studies as to whether the lift between two side-by-side bodies was attractive or repulsive, and no data was found for the yaw moment between identical bodies with zero relative motion. The desire to understand lift force and yaw moment behavior to maintain formation and prevent collisions served as another motivation for this study.

Another aspect of the UUV problem is that UUVs often move at different speeds relative to each other, such as during overtaking, refueling, and docking maneuvers. This relative motion produces interactions in addition to those that already occur in close proximity. Most of the existing studies on relative motion focused on ship overtaking maneuvers. For example, in a test of model ships, Vantorre et al. [26] found that the lift force between the ships was repulsive in the far field, then attractive as the faster ship passed the slower ship. The lift coefficient peaked at a value of $C_L = 0.02$ when the ships were side-by-side [26]. The moment started bow-out for the faster ship, then transitioned to bow-in when it came within half a body length of the slower ship [26]. C_M peaked in magnitude with a value of -0.06 shortly after the peak in C_L [26]. Similar to ships, attractive lateral forces between UUVs may result in a collision, and changes in yaw moment must be countered by steering to maintain control of the UUV. These effects are particularly strong during an overtaking maneuver. The desire to understand the effects of relative motion as they apply to an overtaking maneuver between UUVs was also a motivation of this study.

Based on the existing knowledge of interactions between bodies in close proximity – along with the desire to understand the effects of these interactions on UUV operations – UUV hydrodynamic interactions in close proximity were identified as an important topic for investigation. The investigation would characterize the drag, lift, and moment interactions between UUVs, both with and without relative motion

present. In doing so, the investigation would build upon existing knowledge of hydrodynamic interactions, fill gaps left by previous studies of UUV forces, and provide insights about how to increase the safety and efficiency of multi-UUV operations.

1.1 Interactions Between Bodies in Close Proximity

Previous works on hydrodynamic interactions between bodies in close proximity are discussed in this section to provide additional background relevant to the ellipse interactions investigated by this study. Geometries used by previous studies included 2D cylinders, UUVs, ships, and bodies of revolution. Transient motion was presented in some of the studies, albeit to a more limited extent due to the difficulty of performing simulations and experiments that include relative motion. In addition to modeling a variety of different approaches, these studies served as a basis for comparison with the results of the current study.

1.1.1 Identical 2D Cylinders

Interactions between identical 2D cylinders in a steady cross-flow have served as the topic of numerous experimental and numerical studies due to their many engineering applications and the complex interactions that occur between the shear layers, vortices, Karman vortex streets, and wakes of the cylinders [23].

One review with broad coverage of these studies was provided by Zdravkovich [34], who classified the results of several cylinder studies by dividing the configurations into side-by-side, tandem, and staggered arrangements. It was found that introducing an interference force coefficient helped to explain the origin of the different forces experienced by two cylinders in the side-by-side arrangement [34]. It was further found that two different regimes of lift force existed in the staggered configuration: entrainment of flow into the fully developed wake of the upstream cylinder, and an intense gap flow displacing the wake of the upstream cylinder [34]. Using the results of Hori [8], the staggered arrangements were divided into regions based on the lift force experienced by the cylinders and the change in drag force from that of a single

cylinder. A similar representation was created using the ellipse results of this study and is compared to the cylinder results of Hori (1959) (see Figures 4-1 and 4-2 in Section 4.1).

Another, more recent review with greater coverage of numerical studies was provided by Sumner [23]. Although greater attention was paid to intermediate wake structure behavior and Strouhal number in different flow regimes (which were not a focus of this study), the general trends in force coefficients included by Sumner (2010) were compared to the stationary case simulation results (see Chapter 4). Figure 1-1, provided by Sumner (2010) and taken from Alam et al. (2003), shows how the mean drag and lift force coefficients, C_D and C_L, for two side-by-side circular cylinders changed with respect to the gap ratio, T/D, between the cylinders. One characteristic of the side-by-side configuration is that the flow past the cylinders is asymmetric, as evidenced by the presence of a wider wake behind one cylinder and a narrower wake behind the other. This asymmetry occurs because the side-by-side configuration is the limit of two different staggered configurations: one in which the first (or "top") cylinder is upstream, and the other in which the second (or "bottom") cylinder is upstream [23]. Because these limits are reached simultaneously, the flow tends to pick one of the limits randomly and/or oscillates between the two [23]. The results of C_D in Figure 1-1 showed that the cylinder with the narrower wake experienced a greater drag coefficient than the cylinder with the wider wake for $T/D < 1.5$, and that C_D of both cylinders increased at smaller gap ratios. The results of C_L showed an attractive lift between the cylinders and a greater C_L for the wide-waked cylinder compared to the narrow-waked cylinder for $T/D < 1.0$. The cylinders experienced a mutual increase in repulsive C_L at smaller gap ratios. One exception to these trends was observed by Alam et al. [1], who recorded an attractive C_L for the narrow-waked cylinder at the smallest gap ratio, $T/D = 0.10$ [23]. The reversal in C_L occurred on account of the two cylinders behaving as a single bluff body, leading to a highly separated gap flow that produced a small separation bubble [1; 23]. An important takeaway from this result was that body positioning can incur fundamental changes in the flow, influencing behavior such as the attractive or repulsive orientation of

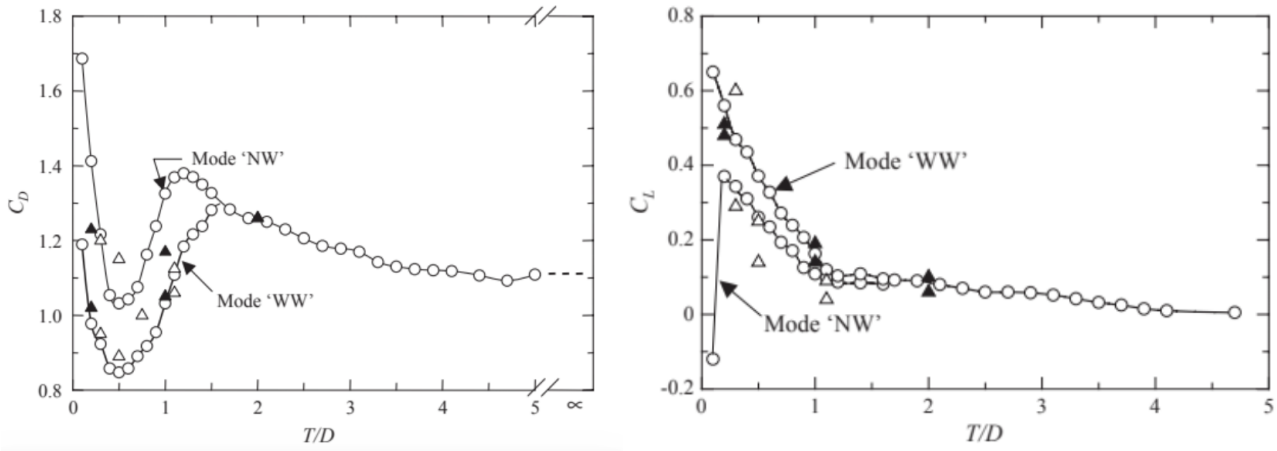

Figure 1-1: C_D and C_L as a function of dimensionless gap ratio: ▲, Hori (1959), $Re = 8000$; △, Zdravkovich & Pridden (1977), $Re = 6 \times 10^4$; ∘, Alam et al. (2003), $Re = 5.5 \times 10^4$. Modes 'NW' and 'WW' denote cylinder with narrow and wide wake, respectively. Taken from Alam et al. [1].

lift interactions. This idea is revisited in Section 4.3 when analyzing lift interactions between ellipses in the stationary case.

1.1.2 UUV Pairs

Previous studies on UUV pairs in viscous, rotational flow attempted to divide the configurations into separate regions based on the force interactions between bodies, with a focus specifically on drag coefficient. Figure 1-2 shows the results of Rattanasiri et al. (2014), who divided the configurations into seven different regions of interaction between two identical 6:1 prolate spheroids in 3D. The interaction regions were determined based on the percentage difference in C_D of each spheroid with respect to the C_D of an isolated spheroid in viscous flow. The percent-difference calculation is shown in equation 1.1:

$$\%\Delta C_D = \frac{C_D - C_{D,iso}}{C_{D,iso}} * 100, \tag{1.1}$$

where C_D is the drag coefficient for the spheroid in the two-body simulation, and $C_{D,iso}$ is the drag coefficient of an isolated spheroid under the same flow conditions.

The results for each position also included the percent change in drag for the

overall system $\%\Delta_{tot}$, which was calculated using equation 1.2:

$$\%\Delta_{tot} = \frac{C_{D,1} + C_{D,2}}{2C_{D,iso}} * 100, \tag{1.2}$$

where $C_{D,1}$ and $C_{D,2}$ are the drag coefficients calculated for bodies 1 and 2, respectively.

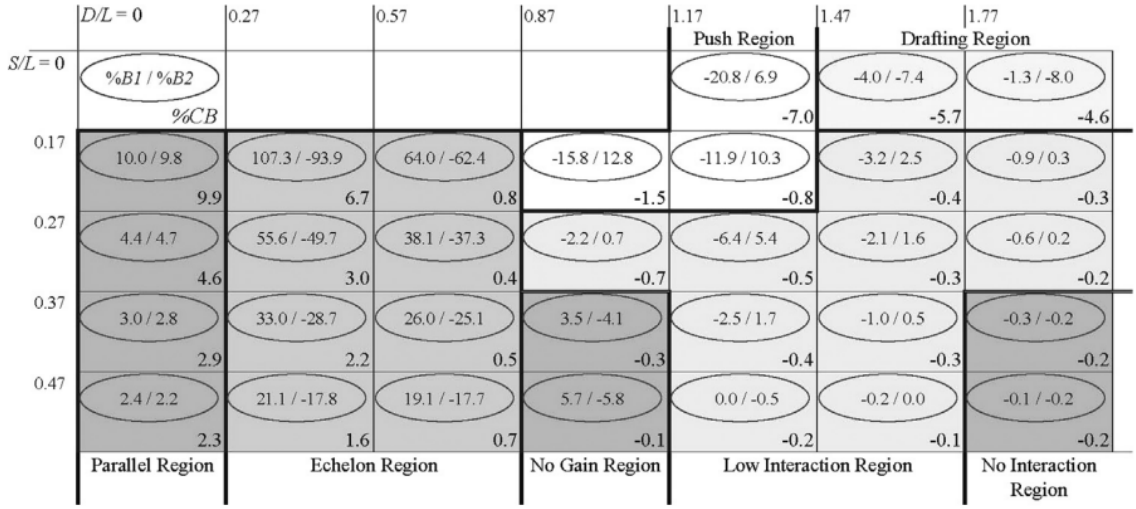

Figure 1-2: Results of Rattanasiri et al. (2014) showing seven different regions of interaction between two identical 6:1 prolate spheroids. Included for each position are the percent change in C_D of the leading and trailing vehicles, respectively, as well as the combined drag coefficient.

Tian et al. [25] performed a UUV study with a similar focus on C_D at different UUV positions. The results of this study are shown in Figure 1-3. The format was slightly different from Rattanasiri et al. (2014) in that the drag coefficient of each vehicle was divided by that of an isolated body (0.0774). A value greater than one indicated a drag increase, and a value less than one indicated a drag decrease. For example, in the tandem position at 1.25 body lengths behind ($a = 0$, $b = 1.25$), the leading vehicle experienced 79.1% of the C_D of an isolated vehicle. Tian et al. divided the interactions into four regions: parallel, pull, push, and tandem. The parallel region caused a drag increase for both bodies; the pull region caused a drag increase for the leading body and a drag decrease for the trailing body; the push region caused a drag decrease for the leading body and a drag increase for the trailing body;

and the tandem region caused a drag decrease for both bodies (with the exception of $(a, b) = (0.00, 1.25)$, where the trailing body experienced a drag increase).

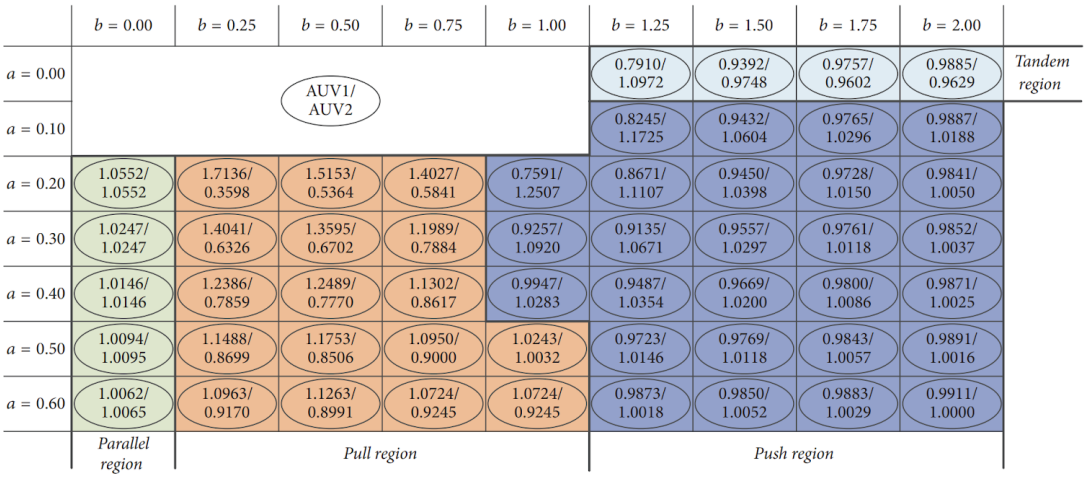

Figure 1-3: Results of Tian et al. [25] showing four different regions of interaction between two identical 6:1 prolate spheroids

A few common patterns were observed between the results of Rattanasiri et al. [17] and Tian et al. [25]:

- The drag of both UUVs increased for side-by-side formations, and this effect became more pronounced as the lateral separation decreased. Rattanasiri et al. [17] found that the drag was increased by about ten percent for both UUVs when they were $y/L = 0.17$ apart, compared to about two percent when the spacing was $y/L = 0.47$. Tian et al. [25] found a 5.5% increase for both UUVs at $y/L = 0.20$, compared to less than one percent at $y/L = 0.60$.

- In staggered formations, where the ellipses overlapped, drag generally decreased for the downstream UUV and increased for the upstream UUV. This area was referred to as the "echelon" region by Rattanasiri et al. [17] and as the "pull" region by Tian et al. [25]. There was generally an overall net drag increase for the system in these formations. For example, at $(x/L, y/L) = (-0.57, 0.17)$, Rattanasiri et al. [17] found that the drag coefficient of the upstream UUV increased by 64% and that the drag coefficient of the downstream ellipse decreased by 62.4%, leading to an overall drag increase of 0.8% for the system. At

$(x/L, y/L) = (-0.50, 0.20)$, Tian et al. [25] observed a 51.5% increase in drag coefficient for the upstream ellipse and a 46.4% decrease for the downstream ellipse, leading to an overall drag increase of 2.6% for the system. Interestingly, the echelon (or pull) region resembled one of the swimming positions documented in biological studies on dolphins: a dolphin calf will often swim slightly behind its mother's flank for ease of swimming effort [21].

- In tandem formations, where the downstream UUV was located fully behind the upstream UUV, the leading ellipse tended to experience a decrease in drag, while the downstream UUV experienced either an increase an drag (known as a "push" region because of the one-sided benefit to the upstream ellipse) or a decrease in drag (known as a "drafting" region because of the mutual benefit to both ellipses). An example of a drafting position in the tandem configuration appears in Rattanasiri et al. [17] at $(x/L, y/L) = (-1.47, 0.00)$, where there was a four percent decrease in the drag coefficient of the upstream ellipse and a 7.4% decrease for the downstream ellipse. Similarly, in Tian et al. [25] at $(x/L, y/L) = (-1.50, 0.00)$, the drag coefficient decreased by 6.1% for the upstream ellipse and by 2.5% for the downstream ellipse. It should be noted that the models of both studies assumed the absence of propeller wake effects, so the tandem configuration results have limited relevance with respect to interactions between real-life UUVs.

The C_D interaction regions presented by Rattanasiri et al. (2014) and Tian et al. (2017) served as a basis for comparison with the results of C_D in the current study that are analyzed in Chapter 4. Particular attention was paid to the regions in which different drag interactions (e.g. pushing, pulling, drafting) occurred. However, unlike these studies, the current study also explored the lateral (lift) forces and yaw moments between ellipses in close proximity. Both lift and yaw moment are consequential in terms of a UUV's ability to remain on its intended course and steer to prevent a possible collision, but they did not receive significant coverage in existing UUV-focused studies of stationary (i.e., zero relative motion) ellipses.

1.1.3 Transient Motion Effects

The fluid dynamic interactions of an overtaking maneuver between two objects are a topic of interest in engineering applications such as race cars and surface ships. A brief summary of studies involving overtaking maneuvers, along with their similarities and differences to the current study, is included to provide additional background on the overtaking case that is presented in Chapter 6.

Differences in Reynolds number across studies of transient motion affected the extent to which their results could be compared to the current study. All of the existing transient motion studies were performed at higher Reynolds numbers ($\mathcal{O}(10^6)$) than were used in the current study ($\mathcal{O}(10^3)$); therefore, it was necessary to consider differences in turbulent versus laminar regimes when comparing the results. It should also be noted that all of the transient motion studies were performed in 3D and used different geometries. As a result, comparison to these results was mainly qualitative in nature.

Race Cars

Romberg et al. [19] used wind tunnel tests to determine the aerodynamic effects of drafting and passing situations on race cars. Due to the limitations of wind tunnel space, the tests were performed in several steady-state configurations which were subsequently compiled together to model interactions during a passing maneuver. The results showed the advantage of the drafting configuration for both cars, particularly the trailing vehicle, by way of reducing drag. The drafting configuration can be used by the cars to increase speed and/or reduce fuel consumption during a race. The lateral forces were also measured and showed the existence of a small attractive force at large longitudinal distances, followed by repulsion when the cars approached one body length apart. The interaction transitioned into an attractive lateral force when the cars came alongside each other. Apart from the obvious difference in body geometry, Romberg et al. (1971)'s study differed from the current study in that it did not account for the time-dependent nature of the passing maneuver and instead

relied on discrete time "snapshots" to depict the body interactions. In this way, the methodology more closely resembled the stationary simulations that are described in Chapter 3.

Ships

The topic of hydrodynamic interactions between ships engaged in an overtaking maneuver shares a common motivation with the current study: understanding lateral force and yaw moment interactions between bodies in close proximity to aid their safe maneuvering. The diagram in Figure 1-4, taken from a review by Muscat-Fenech et al. [12], summarizes the sway and yaw moment interactions during a ship overtaking maneuver, based on predicted areas of high ('+') and low ('-') pressure on the hulls. Although the diagram is a simplification that does not consider surface effects or the changing pressure profile along the hulls of the ships, it serves as an example of classifying the interactions between bodies in an overtaking maneuver and explaining the underlying causes of these interactions. In the current study, a similar depiction of overtaking regions is presented using the results of the overtaking simulations (see Figure 7-1).

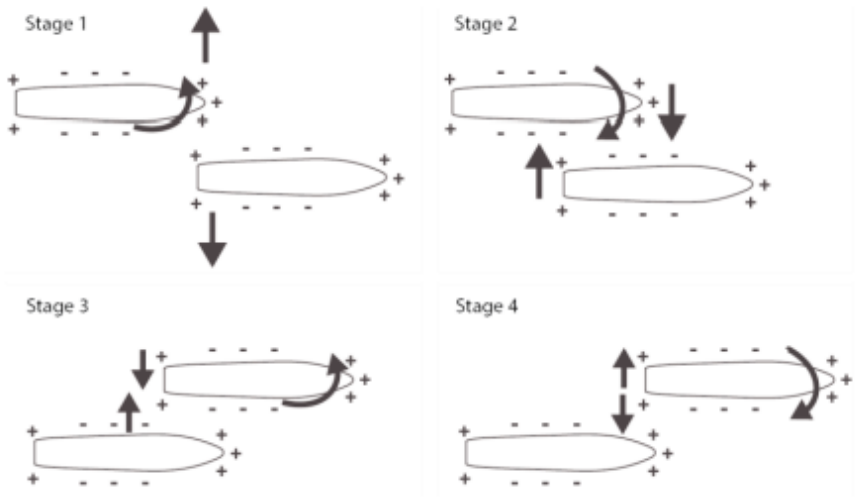

Figure 1-4: Interaction regions during ship overtaking, based on the results of numerical and experimental ship overtaking studies [12]

Ship overtaking has received treatment in both numerical and experimental forms.

The numerical studies generally focused on how closely their simulations resembled experimental results using the smallest amount of computational expense. For example, the numerical investigations by Yuan et al. [33] and Skejic and Faltinsen [22] relied on a potential flow assumption justified by the high Reynolds numbers of ship movements. Although the computational models in these studies successfully reproduced the effects encountered in a ship overtaking maneuver, experimental results tend to provide a more direct representation of actual physical phenomena. Therefore, when comparing the literature to overtaking case simulations in this study, it was important to include experimental studies of ship behavior, including those by Vantorre et al. [26] and Yu et al. [32]. Due in part to the difficulty of testing two ships in forward motion, the experimental studies by Vantorre et al. [26] and Yu et al. [32] tested a subset of the ship overtaking problems, in which a model ship moved past a stationary model ship. Although this test case is more relevant to ships than to UUVs, it has the benefit of isolating the effects of transient motion rather than including the forward motion of both ships. For this reason, the overtaking-stationary case is also simulated in Chapter 6. A previous numerical example of the overtaking-stationary test case is found in Xiang and Faltinsen [31], who simulated a model ship overtaking a stationary model ship in potential flow.

The ship studies were all in agreement regarding the general pattern of interaction behavior between ships. The overtaken ship experienced a drag increase followed by a drag decrease after the overtaking ship passed its beam, and the overtaking ship experienced the opposite effect [26; 12]. The lateral force was repulsive while the overtaking ship was in the far field, then attractive after its bow passed the stern of the overtaken ship, then repulsive again as its stern cleared the bow of the overtaken ship [26; 32; 12]. The moment was directed bow-in for both ships until the overtaking ship passed astern of the overtaken ship, then stern-in until it passed abeam, then bow-in again until it passed the bow and leveled out to zero [26; 32; 12]. Overall, the forces and moments on the overtaking ship were much smaller than those on the overtaken ship, and this difference was more pronounced if the overtaken ship was stationary [26; 32; 12].

A difference between the parameters of the ship studies and those of the current study was that the ships were assumed to be in a relatively narrow channel such as a canal or a tow tank with surface effects present, whereas the current study assumed that the ellipses were deeply submerged and in open water. Possible effects of boundary conditions on the force interactions between bodies are investigated while analyzing the overtaking case in Chapter 7.

UUVs

The transient motion case between UUVs, particularly longitudinal relative motion, has received limited attention. Randeni P. et al. [16] focused on changes in the force and yaw moment coefficients resulting from lateral (sway) motion between UUVs, but they did not test different relative configurations of the vehicles. Leong et al. [10] investigated the interactions between UUVs at different fixed speeds and relative positions, but they relied on time-independent "snapshots" that did not use relative motion to represent the overtaking maneuvers. Zhang et al. [35] performed a similar investigation to Leong et al. [10], but they used only a single fixed speed. Despite these differences in approach, the interactions observed in the UUV studies generally agreed with the results of the ship studies. The UUV drag coefficient transitioned from a net increase to a net decrease as it passed abeam of its neighbor. The lift was attractive when the UUVs were located within one body length of each other longitudinally and was repulsive otherwise. The moment was directed bow-in while the UUV was more than one body length behind; then it became bow-out until the UUV passed abeam of its neighbor; then it switched to bow-in again, before leveling out to zero in the far field. When comparing these results to the current study, it should also be noted that all of the UUV studies investigated UUVs of different sizes rather than identical UUVs and used specific hull designs in lieu of regular geometric shapes.

Slender Bodies of Revolution

A more generalized approach toward the overtaking case was that of Wang [27], who investigated two slender bodies of revolution translating in close proximity. Concerning the lateral force, it was found that the bodies experienced repulsion, attraction, and repulsion again over the course of the passing period. The repulsive phases occurred due to the high-pressure stagnation points pushing the bodies apart, and the attractive phase occurred due to the faster speed of restricted flow between the bodies. Increasing the relative velocity did not change the phases for the slower body, but it significantly increased the duration of the attractive phase for the faster body. Another finding was that when the relative velocity increased, the lateral force on the slower body increased, whereas the lateral force on the faster body decreased. The faster body experienced a small bow-in moment, followed by a larger bow-out moment during the first half of the passing maneuver. Conversely, the slower body changed from a small bow-out moment to a larger bow-in moment over the first half of the passing maneuver. As with the lateral force, the moments on the slower body were larger than those on the faster body and increased with relative velocity. The repulsive phases of the passing maneuver produced smaller moments on the bodies, because the repulsion only increased according to their relative velocity. The attractive phase produced larger moments, because the attraction increased according to the flow velocity between the bodies, which exceeded their relative velocity. Wang (2007)'s study provided useful analysis on the passing maneuver, but because the study was performed analytically (using Newman-Tuck slender body theory), it could only be referenced to gain a basic intuition about interaction behaviors in the overtaking case.

1.2 Potential Flow Case

As seen in various studies referred to above, potential flow has been used by biological [30; 21] and ship [22; 27; 31] studies as a simplified way to approximate flow at turbulent Reynolds numbers. The justification for this approach was that at high

Reynolds numbers, only thin layers of fluid surrounding the bodies (less than 5 percent of the radius) are affected by viscosity. Therefore, assuming the bodies are not located within this small radius, it is equivalent to make the bodies slightly thicker and to ignore viscosity altogether – a simplification known as the displacement thickness model [30]. As with any model, the use of potential flow to represent turbulent flow comes with its own limitations; furthermore, the current study operated at a much lower, subcritical Reynolds number ($Re = 1500$) where a displacement thickness model was not justified. However, the choice of flow regime does not discount the utility of a potential flow investigation altogether. Rather than rely on potential flow to fully represent the flow characteristics, it could be used as a medium through which to understand the pressure-driven interactions between bodies, and possibly to serve as a baseline for comparison to other flow regimes. In this case, accurate simulations of ellipse interactions in potential flow would allow pressure-driven forces to be determined independent of viscous effects. Comparison of these pressure-driven forces to stationary simulations in viscous flow would allow the role of potential flow in the overall ellipse interactions to be determined. Although such an insight would be useful to the present application, simulations of ellipse interactions in potential flow were limited by the knowledge of where to place the stagnation point. The location of the stagnation point is necessary for calculating the pressure along the boundaries of each ellipse to obtain reliable force coefficients, especially lift. Therefore, if numerical simulations of potential flow were performed, the stagnation point of both ellipses would need to be determined experimentally and input as a separate parameter into the simulator. Since the necessary experimental data was not available, the potential flow case was not in included in this study. It is expected that even in a laminar regime where viscous effects dominate, potential flow would play a distinguishable role in the flow characteristics and produce interaction forces that exist independent of viscosity.

1.3 Overview

This study aimed to characterize the hydrodynamic interactions (drag, lift, and yaw moment) between an identical pair of UUVs using 2D numerical simulations. The UUVs were represented by 6:1 (length-to-width) ellipses, and the simulations were performed using a pre-existing computational fluid dynamics (CFD) simulator. The interactions were studied in an incompressible, viscous, rotational flow with the ellipses positioned in tandem, side-by-side, and staggered arrangements. An overtaking maneuver was also simulated at multiple relative speeds and lateral separations to analyze the effects of transient motion on the ellipses.

The numerical simulations performed in this study used the immersed-interface method (IIM) instead of the body-fitted grid approach used by most UUV studies. The IIM code uses polynomial expansions to adapt standard free-space finite-difference schemes near the intersection between the boundary of a body and a fixed cartesian grid. This approach enabled high accuracy while eliminating the need to construct a body-fitted grid, thereby reducing computational cost – especially when studying bodies in relative motion. The methodology of the numerical simulations is described in Chapter 2.

The stationary case simulations, in which both ellipses moved forward at the same speed, were performed at chord-based Reynolds number $Re = 1500$. Many real UUVs operate in higher Reynolds number regimes, but those are beyond the range of the type of high-fidelity numerical simulations performed here. The approach of simulating Reynolds numbers of $\mathcal{O}(1000)$ with full transient behavior and high accuracy leads to insights that are assumed representative of higher Reynolds number systems. This assumption will be tested throughout the thesis through comparisons with other approaches, both numerical and experimental. During each simulation, the drag, lift, and yaw moment coefficients were calculated at regularly-spaced intervals and used to characterize the hydrodynamic interactions at each position. Using these results, a representative map of force and moment interactions was created to identify patterns in ellipse behavior. The stationary case simulations are discussed in Chapter

3. Further analysis of the stationary case – including a comparison of the observed interactions to existing studies of 2D cylinders and UUVs – is provided in Chapter 4.

Chapter 5 describes an investigation of ellipse interactions in an infinitely repeating grid. Ellipse configurations were chosen from the stationary simulations and repeated using unit cells of one or two ellipses, which were made to repeat infinitely through the use of periodic boundary conditions. The results were compared to the stationary case and used to model how UUVs would interact in a large formation such as a fleet or swarm.

The overtaking case, in which one ellipse moved past the other at a constant relative velocity, was also studied. The overtaking case is seen in refueling and docking maneuvers that are performed in UUV operations, but previous studies mainly focused on lateral (sway) motion between an UUV and a much larger vessel such as a submarine [10] [16]. Overtaking case simulations were performed on the ellipse in viscous flow, providing insights about the effects of lateral separation and relative longitudinal velocity on UUV forces. Extensions of the overtaking case were also simulated, including having one ellipse completely stationary. The overtaking case is discussed in Chapter 6. Further analysis of the overtaking case – including a comparison to the stationary case that highlights the individual roles of pressure, viscosity, and relative motion – are provided in Chapter 7.

The study concludes with a summary of findings and recommendations for further study in Chapter 8.

THIS PAGE INTENTIONALLY LEFT BLANK

Chapter 2

Methodology

This chapter describes the approach used for numerical simulations during this study. Although focus was mainly directed toward the application of the simulator rather than the details of its computational methods, a basic explanation is provided to facilitate understanding of the code. A detailed discussion of the numerical methods employed by Cubism-IIM2D is provided by Gabbard et al. [6]. Also included in this chapter are descriptions of the simulation area, flow regime, calculation of force and moment coefficients, and determination of resolution and domain size.

2.1 Immersed Interface Method Code

The CFD simulator used for this study, named Cubism-IIM2D, solves the 2D incompressible Navier-Stokes equations in vorticity-velocity form. The presence of the body is handled with an immersed interface method (IIM). This approach differs from more standard engineering approaches in three aspects. First, the simulations here are classified as Direct Numerical Simulations (DNS) since no turbulence model is used, whereas most engineering approaches rely on a Reynolds-averaged Navier Stokes (RANS) turbulence model (e.g., $k-\epsilon$, $k-\omega$, SST). Consequently, the simulations here are transient and fully resolved, but at a lower Reynolds number than most RANS approaches. Second, IIM permits the use of fixed, Cartesian grids for discretizing stationary and moving bodies of arbitrary geometries, thus eliminating

the need to construct a costly body-fitted grid while retaining high-fidelity of the solution (illustrated in Figure 2-1). Third, using the vorticity-velocity formulation free-space boundary conditions can be imposed on small computational domains, which significantly reduces computational expense when calculating the external flow past embedded bodies.

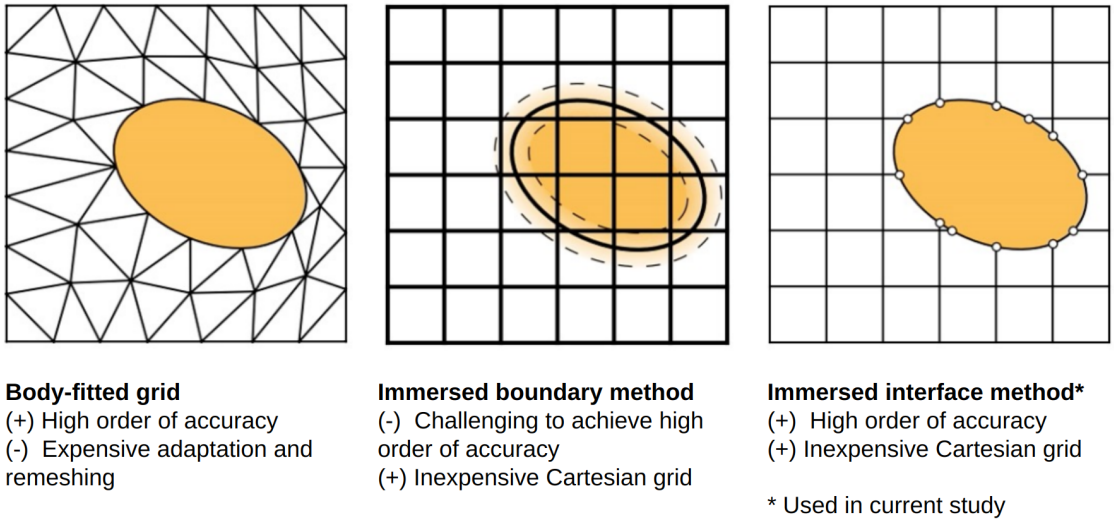

Figure 2-1: Comparison of CFD methods, adapted from Ji [9]

2.1.1 General Computational Approach

Cubism-IIM2D uses the vorticity-velocity form of the incompressible Navier-Stokes equations to calculate flows in 2D. The velocity-pressure form of Navier-Stokes (equation 2.1) is perhaps the most conventional form and represents the conservation of linear momentum for a Newtonian fluid:

$$\rho\frac{\partial\vec{u}}{\partial t}+\rho(\vec{u}\cdot\nabla)\vec{u}=-\nabla P+\mu\nabla^2\vec{u}+\vec{\gamma}\rho. \tag{2.1}$$

The equation features a balance between inertia and the divergence of stress within the fluid. The inertia consists of the variation term $\frac{\partial u}{\partial t}$ and the divergence term $(\vec{u}\cdot\nabla)\vec{u}$, with velocity $\vec{u}$ and time t. Here the flow is assumed incompressible and hence the velocity field satisfies $\nabla\cdot\vec{u}=0$. The stress divergence consists of the pressure gradient

term $-\nabla P$ and the diffusion term $\mu\nabla^2\vec{u}$, where P is the static pressure, ρ is the fluid density, μ is the kinematic viscosity, and $\nabla^2\vec{u}$ is the Laplacian operator applied to the velocity vector, representing a diffusion of momentum between a point in the fluid and its surrounding volume. The term $\vec{\gamma}\rho$ represents an external source, if present.

The vorticity-velocity form of Navier-Stokes is useful because it directly calculates the transport of vorticity via velocity, simplifying the computation of rotational flows. To convert the velocity-pressure form of Navier-Stokes into the vorticity-velocity form (equation 2.2), the curl is taken as shown:

$$\begin{aligned} \nabla \times \left[\rho\frac{\partial\vec{u}}{\partial t} + \rho(\vec{u}\cdot\nabla)\vec{u}\right] &= \nabla \times \left[-\nabla P + \mu\nabla^2\vec{u}\right] \\ \frac{\partial\omega}{\partial t} + \vec{u}\cdot\nabla\omega &= \nu\nabla^2\omega. \end{aligned} \tag{2.2}$$

The second equation above holds in 2D domains where the velocity field is $\vec{u} = \langle u, v, 0\rangle^T$, and hence the vorticity vector reduces to a scalar (i.e., $\vec{\omega} = \langle 0, 0, \omega\rangle^T$). The vorticity-velocity form features an unsteady term $\frac{\partial\omega}{\partial t}$, a convective term $\vec{u}\cdot\nabla\omega$, and a diffusion term $\nu\nabla^2\omega$ (with kinematic viscosity $\nu = \mu/\rho$). At any point in time, the velocity field can be computed instantaneously from the vorticity field by solving a Poisson equation for the stream function ψ as shown in 2.3:

$$\begin{aligned} \nabla^2\psi &= -\omega \\ \vec{u} &= \nabla \times \vec{\psi}, \end{aligned} \tag{2.3}$$

where $\vec{\psi} = \langle 0, 0, \psi\rangle^T$. Further details on the algorithm and implementation of these steps, as well as the IIM boundary treatment, are provided in [6].

2.1.2 Simulator Inputs

Simulation parameters and boundary conditions were given to Cubism-IIM2D in the form of "factory" and "settings" files. Factory files specified characteristics such as the size and position of shapes that were placed in the flow. Settings files specified other information that was needed to run a simulation, such as the flow characteristics and

frequency of data output. Example factory and settings files for several simulations performed in this study are provided in Appendix A. The specific parameters and boundary conditions of each simulation are explained as they appear in subsequent chapters.

2.2 Simulation Area and Flow Regime

The simulation area was arranged as though viewed from above, with the positive x-axis pointing to the left, the positive y-axis pointing upward, and the positive z-axis pointing out of the page and toward the viewer. Due to the study being two-dimensional, the direction of the z-axis was only referenced to orient the moments. Water traveled at a constant velocity $U_\infty = 1$ from left to right. The left, top, and bottom of the domain were treated as free-space boundaries, with no imposed restriction on the velocity or velocity gradient – instead, the velocity is solved so that it decays towards U_∞ far away from the body [6]. The right domain boundary was treated as an outflow condition [6]. For all simulations in this work, the density of the fluid is constant and free-surface effects are ignored as the bodies are assumed to operate at large depth.

A Reynolds number of 1500 was chosen on account of the capabilities of the Cubism-IIM2D simulator being used. Equation 2.4 is the formula for Reynolds number, Re:

$$Re = \frac{U_\infty L}{\nu}, \tag{2.4}$$

where L is the characteristic length of the body (in this case, the length of each ellipse); and ν is the kinematic viscosity of the fluid (equivalent to the dynamic viscosity divided by the fluid density, $\nu = \frac{\mu}{\rho}$). Although the Reynolds number of 1500 did not match the higher Reynolds numbers seen in UUV ($Re = \mathcal{O}(10^6)$) or biological ($Re \leq \mathcal{O}(10^7)$) applications, it provided data on a largely unexplored range for this problem. The lower Reynolds number also fulfilled an interest in delineating the effects of vorticity and viscosity on ellipse forces at a laminar Reynolds number, where such effects tend to dominate.

The two UUVs were represented by a pair of identical, rigid ellipses with a length-to-diameter ratio of 6:1. This ratio was chosen because it was commonly used in all biological and UUV studies featuring elliptical (2D) and ellipsoidal (3D) shapes and was representative of many UUV aspect ratios. A specific UUV hull shape was not chosen so that the results could be more readily compared to a wider variety of geometries (e.g., 2D cylinders, bodies of revolution) and UUV designs (e.g. SUBOFF, Explorer) without loss of generality. The ellipses were oriented as though moving from right to left in the domain such that they moved directly against the inflow of water.

2.3 Calculation of Force and Moment Coefficients

The three values used to indicate ellipse behavior in the flow were drag coefficient C_D, lift coefficient C_L, and yaw moment coefficient C_M. Equation 2.5 shows the calculation for C_D:

$$C_D = \frac{2F_x}{\rho U_\infty^2 L}, \tag{2.5}$$

where F_x is the horizontal force acting on the ellipse, and U_∞ is the reference velocity. Note that due to the two-dimensional nature of the simulations, f_x is defined as force per unit length (i.e., per unit depth into the z direction). C_L and C_M were calculated using equations 2.6 and 2.7, respectively. The equation for lift coefficient is

$$C_L = \frac{2F_y}{\rho U_\infty^2 L}, \tag{2.6}$$

where F_y is the vertical force acting on the ellipse. The equation for yaw moment coefficient of an ellipse with moment M_z is

$$C_M = \frac{2M_z}{\rho U_\infty^2 L^2}, \tag{2.7}$$

with the moment M_z taken around the centroid of each ellipse.

The presence of vorticity and viscosity in the flow caused fluctuations in the force and moment coefficients over time due to the oscillatory behavior of the ellipse wakes.

The variable t^*, or non-dimensional time, was introduced to account for the time dependence of the flow. Equation 2.8 shows the calculation of t^*:

$$t^* = \frac{tU_\infty}{L}, \tag{2.8}$$

where t is the actual (simulation) time, U_∞ is the velocity of the flow, and L is the ellipse length.

Once the ellipse wakes reached a symmetric arrangement (referred to as steady state), the ellipse forces were centered on a value that could be estimated using time averaging. Accordingly, a time-averaged value was calculated for the force and moment coefficients of the ellipses. This was done by identifying the onset of a symmetric wake pattern; determining two peaks in C_L that contained the steady state time period (one toward the beginning and one toward the end); and averaging the values of C_D, C_L, and C_M over this time period. The peaks of C_L were used because they tended to be the most pronounced and therefore the most easily identified. Equation 2.9 shows an example of how the time-averaged coefficient of drag, $\bar{C}_D$, was calculated:

$$\bar{C}_D = \frac{\int_{t^*_{peak,i}}^{t^*_{peak,f}} C_D(t^*)\, dt^*}{t^*_{peak,f} - t^*_{peak,i}}, \tag{2.9}$$

where $t^*_{peak,i}$ and $t^*_{peak,f}$ are the non-dimensional times of the first and last peak of C_L, respectively, and $C_D(t^*)$ represents the value of drag coefficient as a function of non-dimensional time. Figure 2-2 shows a graphical example of how the steady-state peaks in C_L were identified to calculate the time-averaged coefficients.

A useful characteristic of $\bar{C}_D$ is that it correlates directly to the time-averaged

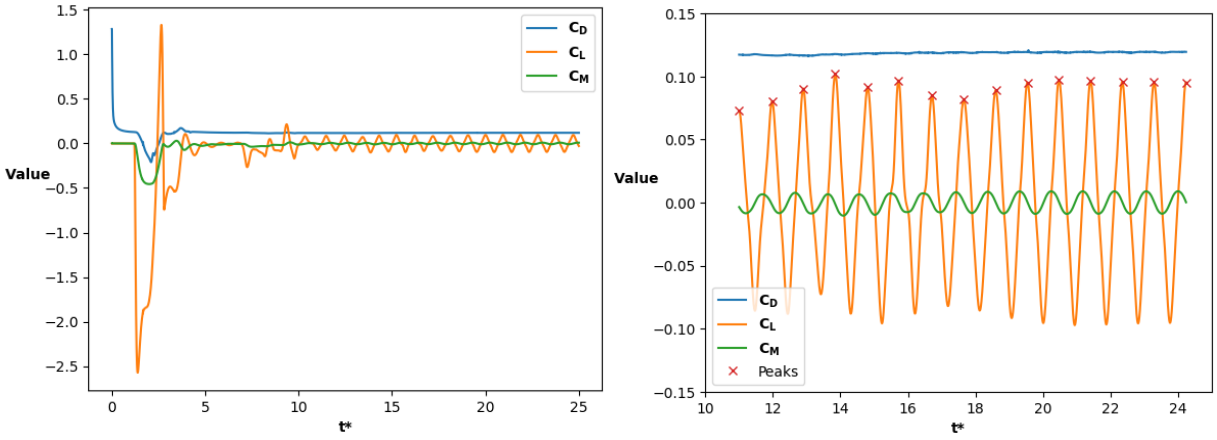

Figure 2-2: Using peaks in C_L to determine range for time-averaged coefficients

coefficient of power $\bar{C}_P$ required to propel the ellipse, as seen in equation 2.10:

$$\begin{aligned} \bar{P} &= \frac{1}{T}\int_0^T F(t)U\,dt \\ \bar{C}_P &= \frac{\bar{P}}{\frac{1}{2}\rho U^3 L} \\ &= \frac{\frac{U}{T}\int_0^T F(t)\,dt}{\frac{1}{2}\rho U^3 L} \\ &= \frac{1}{T}\int_0^T \frac{F(t)}{\frac{1}{2}\rho U^2 L}\,dt \\ &= \bar{C}_D, \end{aligned} \tag{2.10}$$

where $\bar{P}$ is the average power, T is the period of power usage, $F(t)$ is the applied force as a function of time, and U is the velocity of the ellipse.

Another feature of the stationary simulations was the inclusion of an initial perturbation in the free stream velocity. The perturbation consisted of a temporary acceleration of the flow in the y-direction that quickened the onset of a steady state for the ellipse wakes by breaking top-bottom symmetry. This effect was desirable because it reduced the total simulation time without compromising accuracy of the steady-state values. A plot of the free stream perturbation function at the start of the simulation (i.e., $t^* \approx 0$) is shown in Figure 2-3. In the simulations discussed here, the perturbation amplitude peaked in magnitude at $t^* = 1.0$, ended at $t^* = 2.0$, and

never exceeded the value of U_∞.

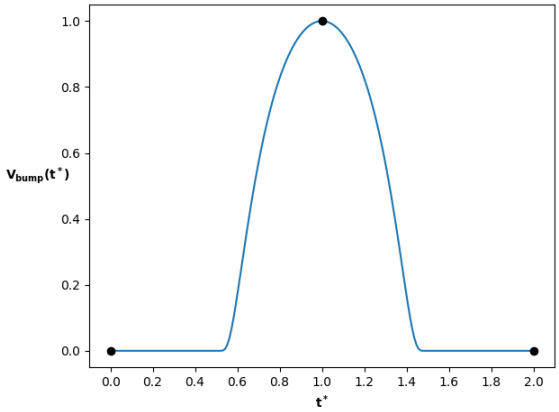

Figure 2-3: Free stream perturbation function to quicken the onset of a steady state for the ellipse wakes. Black dots represent the start ($t^* = 0.0$), peak ($t^* = 1.0$), and end ($t^* = 2.0$) of the perturbation.

2.4 Grid Resolution

To ensure the accuracy of the simulations without incurring undue computational expense, a series of simulations were performed to determine the grid resolution needed for the ellipse simulations. In Cubism-IIM2D, the grid is composed of a set of uniform-resolution blocks, each of $N_b \times N_b$ grid points, arranged in a rectangular domain. In this work, $N_b = 32$ for all simulations. At runtime, the user sets the number of blocks in the x- and y-directions, denoted by *bpdx* and *bpdy* respectively. The user further defines the extent of the domain in the longest direction, denoted with maxextent. In this work, maxextent always refers to the dimension of the domain in the x-direction.

Here the grid resolution was measured in grid points per length of an ellipse (ppl), which was calculated using equation 2.11:

$$\text{ppl} = \frac{N_b * bpdx}{\text{maxextent}} * L. \tag{2.11}$$

In anticipation of adding relative velocity during the overtaking case (see Chapter 6), a Reynolds number of $Re = 3000$ was used when determining the grid resolution and

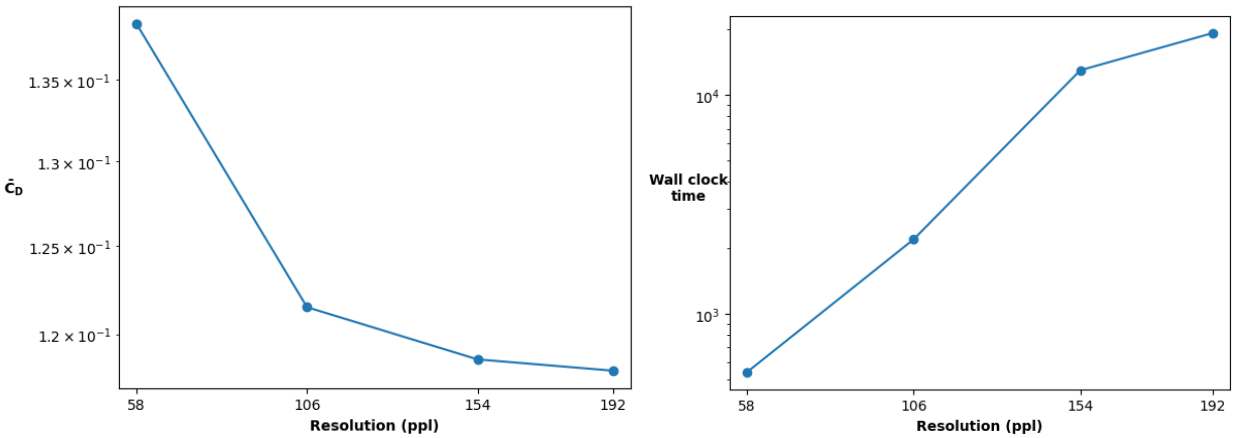

Figure 2-4: Determining grid resolution for a single-ellipse simulation

domain size. This value was used because the relative velocity in later simulations would be increased up to $u_{rel} = 1.00$ against the direction of inflow, $U_\infty = 1.0$, thereby doubling the velocity experienced by the overtaking ellipse. $Re = 3000$ was therefore considered to be the limiting case and served as the basis for the resolution- and domain-finding simulations.

In order to isolate the effects of interactions between two ellipses, the force coefficients on a single, isolated ellipse first needed to be computed. Accordingly, an appropriate grid resolution needed to be determined for the single-ellipse simulations. When determining the resolution, $\bar{C}_D$ served as the value of comparison. Figure 2-4 shows the resolution determination for a single ellipse. The resolution started at $bpdx = 12$ (58 ppl) and was increased in successive simulations by increments of ~ 48ppl (~ 10 $bpdx$ with maxextent $= 8.0$). Based on the results of these simulations, a resolution of 154 ppl gave a value of $\bar{C}_D$ that was within 1% of the next-highest resolution (192 ppl) and was considered to be sufficient for computing the force and moment coefficients of a single ellipse. Table 2.1 shows the numerical results at each resolution.

A similar procedure to the resolution-finding simulations for a single ellipse was repeated for two ellipses. The ellipses were placed at the closest configuration that would be tested in the investigation: side-by-side with a distance of $0.3L$ between their centerlines. In this configuration, there were fewer computational grid points

Table 2.1: Determining grid resolution for a single-ellipse simulation

Resolution, Single Ellipse				
ppl	$\bar{C}_D$	**$\Delta\bar{C}_D$ of next resolution (%)**	**Wall clock time**	**Cost of next ppl increase (%)**
58	0.1386	-12.3	5.4×10^2	305
106	0.1215	-2.4	2.2×10^3	493
154	0.1186	-0.5	1.3×10^4	48
192	0.1180	-	1.9×10^4	-

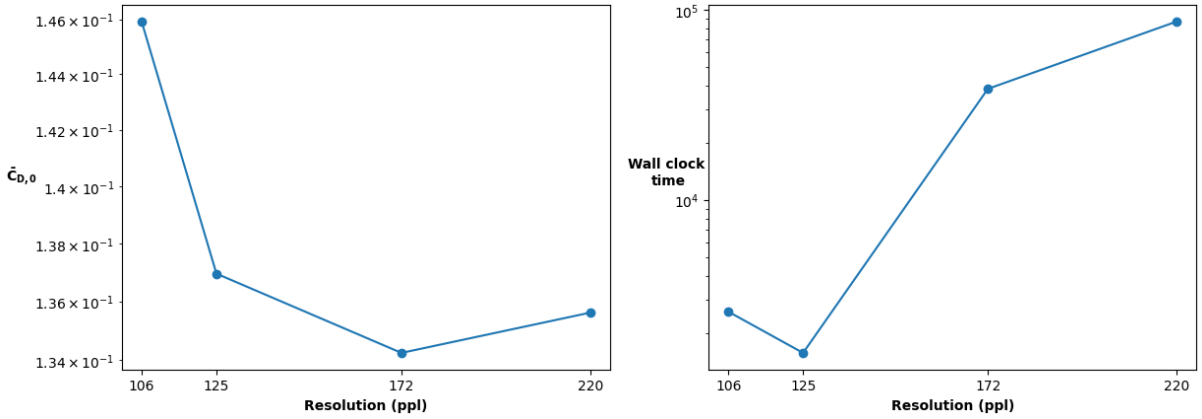

Figure 2-5: Determining grid resolution for a two-ellipse simulation

between the ellipses than in any other configuration that was simulated. It was therefore assumed that a resolution providing an accurate solution at this point would also be sufficient for computing forces in other configurations. Figure 2-5 shows the results of the resolution-finding simulations for two identical ellipses. The resolution started at 106 ppl ($bpdx = 22$ with maxextent $= 8.0$) and was subsequently tested at 125, 172, and 220 ppl. The value was found to converge at 172 ppl ($bpdx = 36$ with maxextent $= 8.0$), which gave a value of C_D that was $\sim 1\%$ different from the next-highest resolution of 220 ppl. Table 2.2 shows the numerical results at each resolution.

Table 2.2: Determining grid resolution for a two-ellipse simulation

Resolution, Two Ellipses				
ppl	$\bar{C}_{D,0}$	**$\Delta\bar{C}_{D,0}$ of next resolution (%)**	**Wall clock time**	**Cost of next ppl increase (%)**
106	0.1459	-6.2	2.6×10^3	-39
125	0.1370	-2.0	1.6×10^3	2345
172	0.1343	1.0	3.8×10^4	126
220	0.1356	-	8.7×10^4	53

2.5 Domain Size

Another step to preparing the simulations was determining the domain size. The resolution of 172 ppl determined in the resolution-finding simulations was maintained, while the domain size was changed based on the number of lengths, L, behind the trailing ellipse. The domain was calculated in this way because during simulations of the staggered and tandem configurations, one ellipse would be located downstream of the other; therefore, the x-position of the downstream ellipse would dictate the minimum distance of wake travel prior to outflow. Although the domain size was not as consequential to accuracy as the resolution (hence why it was determined second), the domain needed to provide sufficient space for the wakes of each ellipse to develop, while also maintaining an acceptable balance of accuracy and computational expense. In order to prevent instabilities in the computations, it was required that the wakes remained within the domain until exiting through the outflow boundary.

Figure 2-6 shows the results of the domain-finding simulations for a single ellipse at $Re = 3000$. Similar to the resolution study, $\bar{C}_D$ was used as the value of comparison between domain sizes. Based on these results, a domain size of seven lengths behind the ellipse was considered suitable. During all of the domain-finding simulations, a length-to-height ratio of 2:1 ($bpdx = 2bpdy$) was maintained for the domain, since this ratio was found to contain the trailing vortices without unnecessarily increasing the computational area. Table 2.3 shows the numerical results at each domain size.

As with the resolution-finding simulations, the domain-finding simulations were

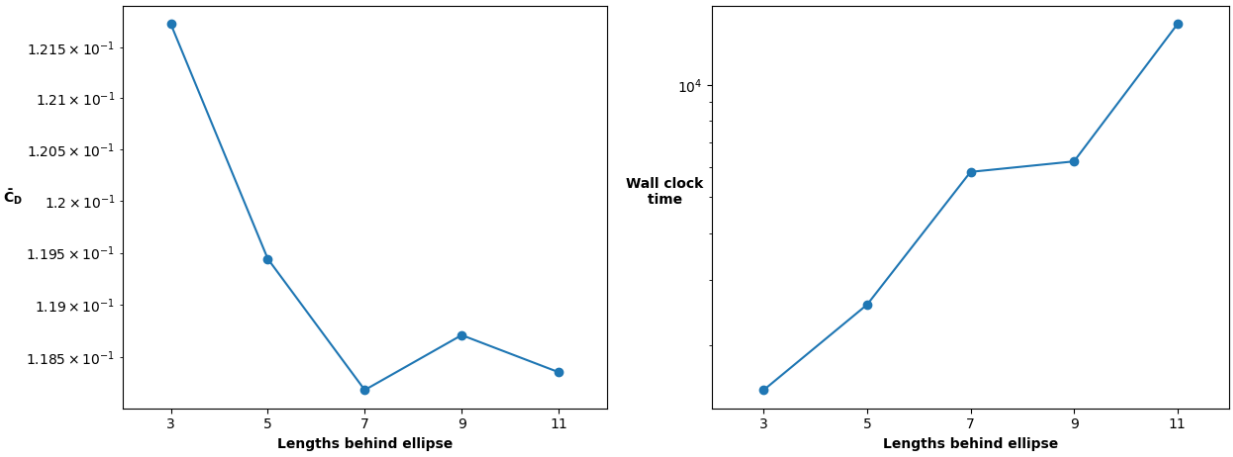

Figure 2-6: Determining domain size for a single ellipse

Table 2.3: Determining domain size for a single-ellipse simulation

Domain, Single Ellipse				
lengths behind	$\bar{C}_D$	**$\Delta\bar{C}_D$ of next increase (%)**	**Wall clock time**	**Cost of next increase (%)**
3	0.1217	-1.9	1.5e3	70
5	0.1194	-1.1	2.6e3	127
7	0.1182	0.4	5.8e3	7
9	0.1187	-0.3	6.2e3	134
11	0.1184	-	1.5e4	-

performed using two ellipses in the same configuration. The results of the domain-finding simulations for two ellipses are shown in Figure 2-7. Based on these results, a domain size of nine lengths behind the trailing ellipse was used for the investigation. Table 2.4 shows the numerical results at each domain size.

Figure 2-8 shows the final setup of the domain for stationary simulations. Note that the diagram is not to scale.

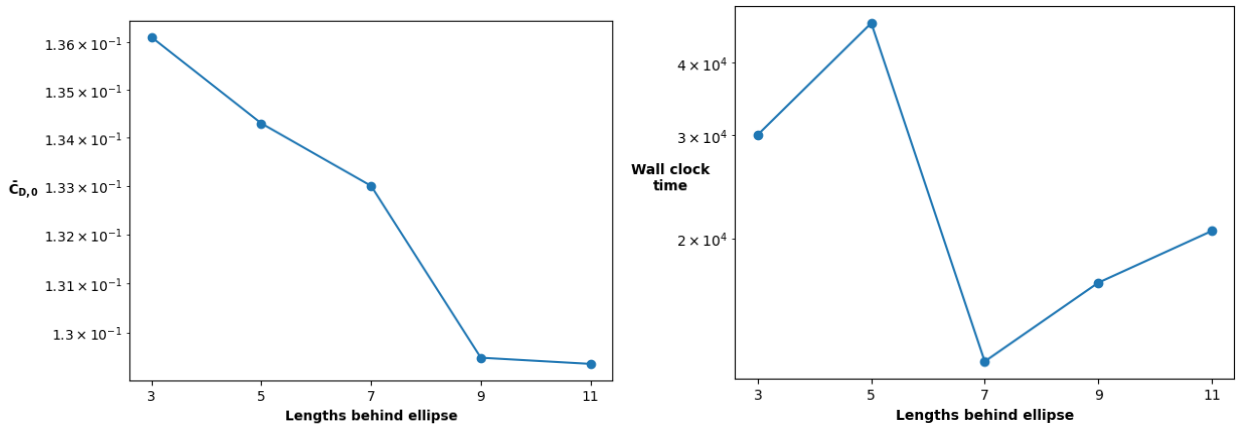

Figure 2-7: Determining domain size for two identical ellipses

Table 2.4: Determining domain size for a two-ellipse simulation

Domain, Two Ellipses				
lengths behind	$\bar{C}_{D,0}$	$\Delta\bar{C}_{D,0}$ **of next increase (%)**	**Wall clock time**	**Cost of next increase (%)**
3	0.1361	-1.3	3.0×10^4	55
5	0.1343	-1.0	4.7×10^4	-74
7	0.1330	-2.6	1.2×10^4	36
9	0.1295	-0.1	1.7×10^4	23
11	0.1294	-	2.1×10^4	-

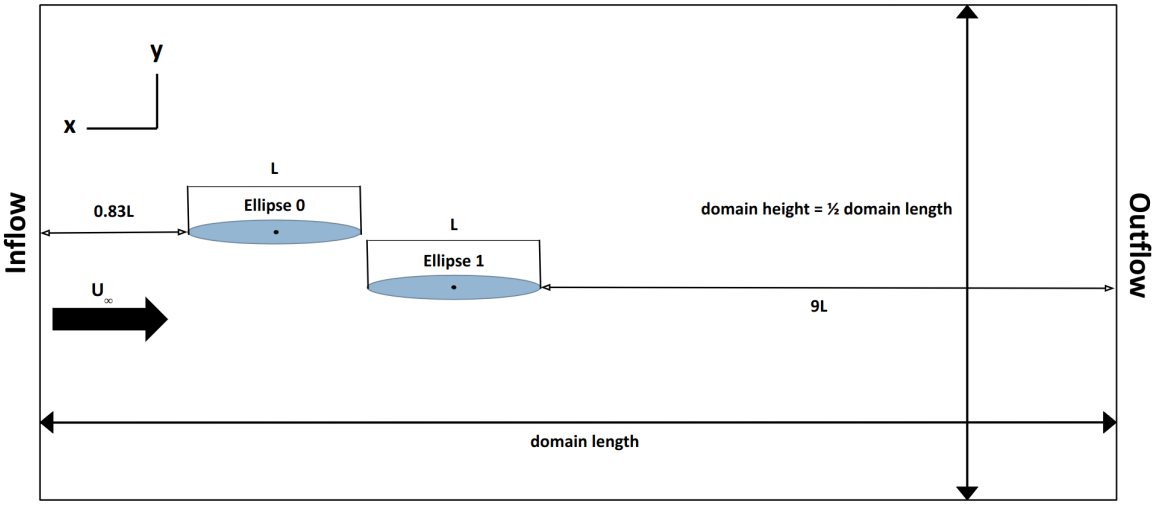

Figure 2-8: Domain setup for stationary simulations (not drawn to scale)

THIS PAGE INTENTIONALLY LEFT BLANK

Chapter 3

Stationary Case

This chapter describes the stationary simulations, in which two identical ellipses moved forward at a constant, matching speed. In Section 3.1, a system is established for positioning the ellipses in various configurations within the domain area. Using these configurations, Section 3.2 presents the results of the stationary simulations.

3.1 Ellipse Positioning

For the simulations of this chapter, the relative position of the ellipses was held constant within each parameter selection to model a constant-velocity cross flow with zero relative motion. Figure 3-1 illustrates the arrangement of the ellipses. The relative position of the centroid of Ellipse 1 with respect to the centroid of Ellipse 0 was measured by the non-dimensional parameters $x^* = x/L$ and $y^* = y/L$.

The configurations chosen for simulations closely resembled those studied in previous works on UUVs – including Molland and Utama [11], Rattanasiri et al. [17], and Tian et al. [25]. The simulated configurations formed a quadrant in the range $0 \leq x^* \leq 1.5$, $0.3 \leq y^* \leq 0.6$. The configurations were spaced $L/6$ apart with respect to x^* and $L/10$ apart with respect to y^*. Based on the results of Rattanasiri et al. (2014) and Tian et al. (2017) (see Section 1.1.2), the ellipses were generally expected to display little to no interaction outside of this range and as such were not considered to be in close proximity. A notable exception is the tandem configuration, as interac-

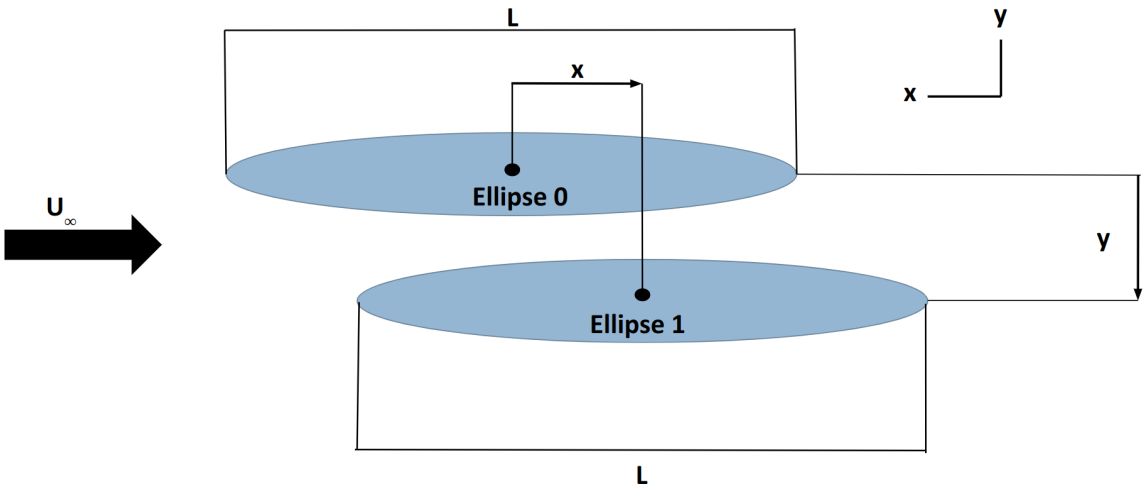

Figure 3-1: Arrangement of the ellipses during simulations

tions for cylinders and ellipses are known to occur at ranges further than $|x^*| = 1.5$. For treatment of interactions in far-field tandem configurations, readers are referred to Rattanasiri et al. [18] for UUVs, Hoerner [7] for foil shapes, and Zdravkovich [34] for 2D cylinders.

Due to the symmetry of the ellipse arrangements, the results of the simulated quadrant could be "reflected" across the $x^* = 0$ axis without loss of accuracy. The symmetry property was valuable because it allowed a more comprehensive picture of the close-proximity interactions to be obtained without performing additional simulations. The results could also be reflected across $y^* = 0$ into the other two quadrants if desired, but a hemispherical view was determined to be sufficient for visualization purposes while also simplifying comparison to the overtaking simulations (see Chapter 7). Obviously, careful attention was paid to the signs of the coefficients and the respective configurations of the ellipses. Figure 3-2 shows how the results of a steady-state simulation in one quadrant could be extended into the other three quadrants using the symmetry property.

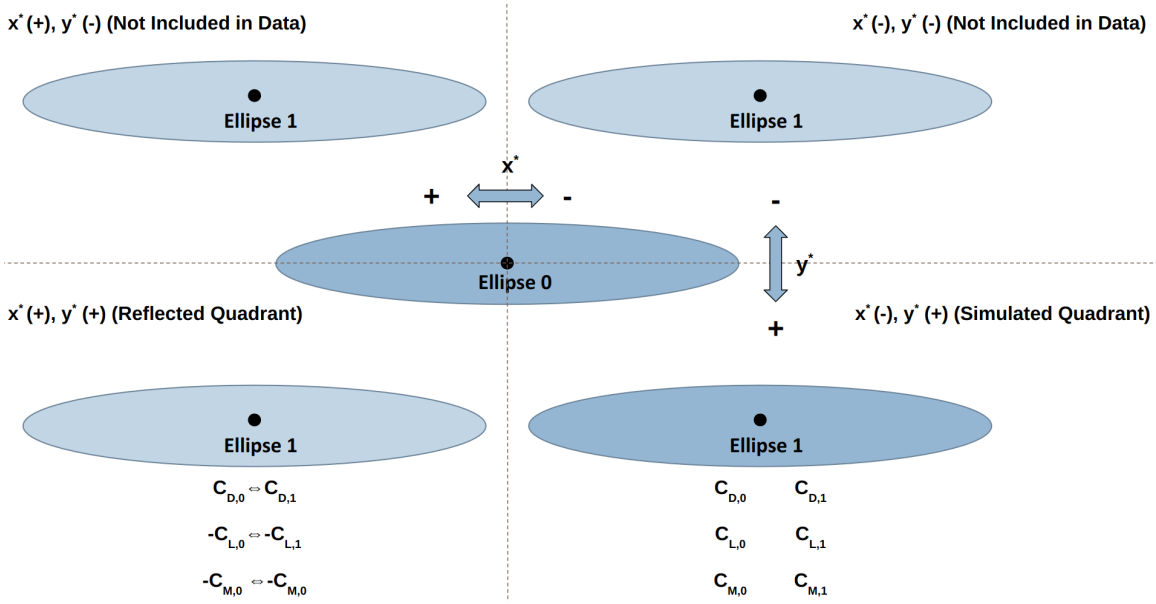

Figure 3-2: Reflection of results due to axisymmetry of the ellipses. When reflecting results across the $x^* = 0$ axis, the results of C_D could be switched between the ellipses when they were in the same respective configuration. The results of C_L and C_M were switched between ellipses and multiplied by negative one.

3.2 Results of Stationary Simulations

Using the resolution and domain size determined in Chapter 2, the investigation proceeded by performing simulations with the two ellipses at each relative position. For these simulations, the time-averaged coefficients of lift ($\bar{C}_L$) and yaw moment ($\bar{C}_M$) were introduced to the calculations.

Each configuration was run for $t^* = 33.3$, and the time-averaged coefficients were calculated for the steady state (symmetric wake) period. Figure 3-3 shows linear plots of $\Delta\bar{C}_D$, $\bar{C}_L$, and $\bar{C}_M$ for Ellipses 0 and 1 across the simulated range of y^*. Here

$$\Delta\bar{C}_D = \bar{C}_D - \bar{C}_{D,iso} \tag{3.1}$$

represents, for each ellipse, the difference in time-averaged drag coefficient from the two-body configuration $\bar{C}_D$, and the time-averaged drag coefficient of the ellipse in isolation $\bar{C}_{D,iso}$. At this Reynolds number $\bar{C}_{D,iso} = 0.117$. A value of $\Delta\bar{C}_D = 0.01$ therefore represents an 8.5% increase in drag from the isolated ellipse value. Note

that for an isolated ellipse, both the mean lift coefficient $\bar{C}_{L,iso}$ and the mean moment coefficient $\bar{C}_{M,iso}$ are zero.

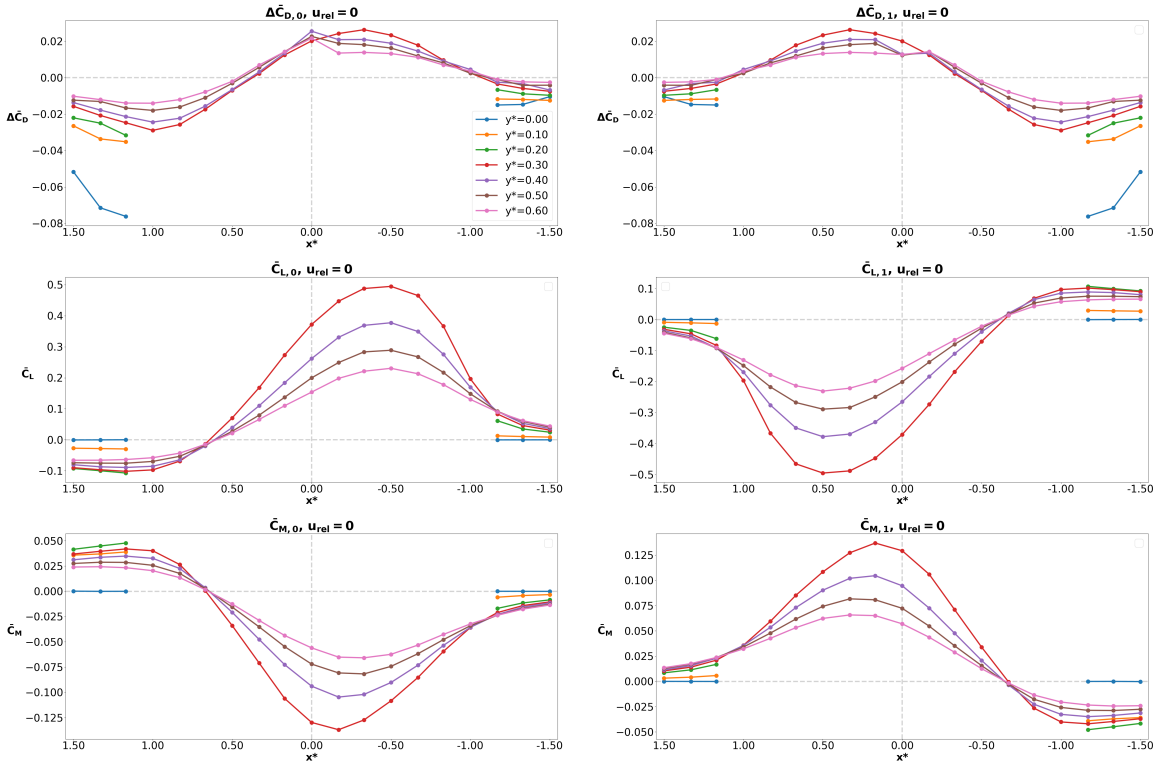

Figure 3-3: Linear plots of the ellipse mapping results

Although the line plots provided a direct representation of the results at discrete positions, a more comprehensive visualization of the interactions was desired. Figure 3-4 shows contour plots of the stationary simulation results, where values between the discrete data points are interpolated via triangulation. Coordinates of x^* and y^* are based on the relative position of Ellipse 1 with respect to Ellipse 0. Areas with positive coefficients are shown in red and correspond to a $\Delta\bar{C}_D$ directed toward the right (drag increase), $\bar{C}_L$ directed upward, or $\bar{C}_M$ directed counter-clockwise. Conversely, areas with negative coefficients are shown in blue and correspond to a $\Delta\bar{C}_D$ directed toward the left (drag decrease), $\bar{C}_L$ directed downward, or $\bar{C}_M$ directed clockwise.

The results of $\Delta\bar{C}_D$ in the plots show that if the ellipses were placed within one body length of each other, the leading ellipse tended to experience a drag increase, while the trailing ellipse tended to experience a drag decrease. When the ellipses approached the side-by-side configuration ($|x^*| < 0.33$), they both experienced a drag in-

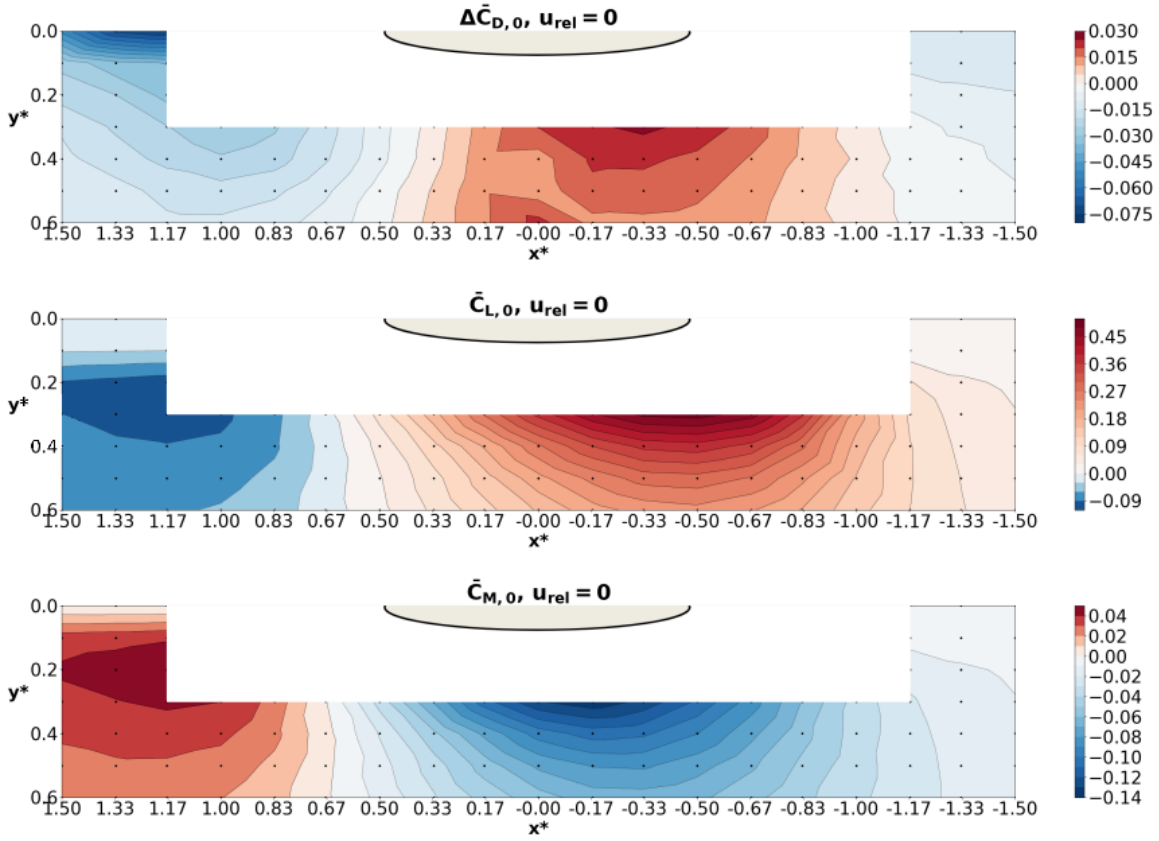

(a) Contour plots for Ellipse 0

Figure 3-4: Contour plots of the ellipse mapping results, using triangulation to interpolate the values between data points

crease. The maximum positive value of $\Delta\bar{C}_{D,0}$ occurred at $(x^*, y^*) = (-0.33, 0.3)$ with a 22.3% increase from the $\bar{C}_{D,iso}$ value of 0.117, and the maximum positive value of $\Delta\bar{C}_{D,1}$ occurred at $(x^*, y^*) = (0.00, 0.3)$ with a 23.7% increase. When one ellipse was placed directly behind the other, both ellipses experienced a drag decrease. The maximum negative values of $\Delta\bar{C}_{D,0}$ and $\Delta\bar{C}_{D,1}$ both occurred at $(x^*, y^*) = (-1.17, 0.0)$ with a 12.8% decrease in $\Delta\bar{C}_{D,0}$ and a 64.8% decrease in $\Delta\bar{C}_{D,1}$.

The results of $\bar{C}_L$ show that there was a slightly attractive lift force between the ellipses when they were more than one body length from each other (i.e., $|x^*| > 1.00$), but that the lift force was otherwise repulsive. The repulsion peaked in magnitude at a value of $|\bar{C}_L| \approx 0.5$ as the ellipses approached the side-by-side configuration. For the closest parallel configuration, the lift force was about four times larger than the total drag force on both ellipses, pointing to the dominance of lift in close-proximity

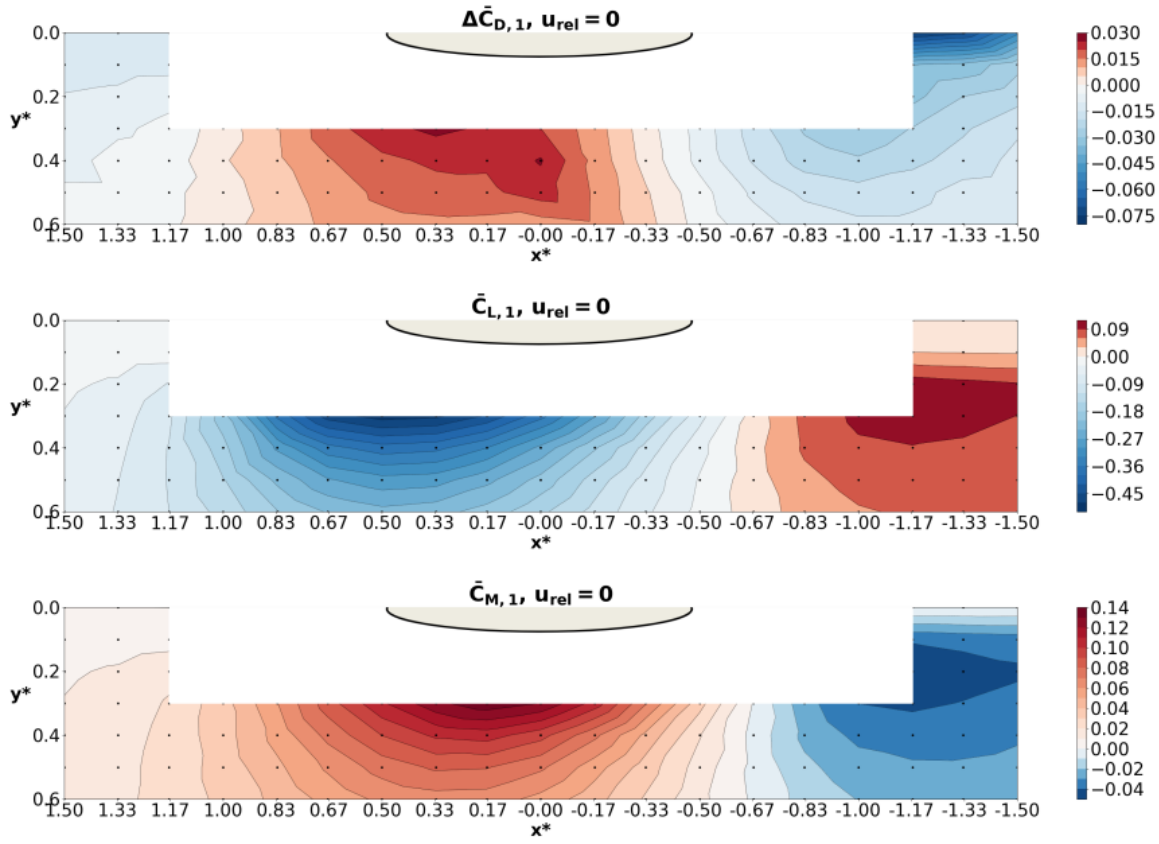

(b) Contour plots for Ellipse 1

Figure 3-4: Contour plots of the ellipse mapping results, continued

interactions.

The plot of $\bar{C}_M$ shows that the yaw moment for Ellipse 0 was directed clockwise (bow-out) for most of the configurations but transitioned to bow-in when Ellipse 1 was beyond one body length ahead ($x^* > 1$). The moment of Ellipse 1 was directed clockwise (bow-in) until it was two thirds of a body length behind Ellipse 1 ($x^* = -0.67$), at which point $\bar{C}_{M,1}$ became counterclockwise (bow-out) for the rest of the configurations. The value of $\bar{C}_M$ was mainly dominated by the pairing of $\bar{C}_L$ and x^*. For example, when Ellipse 1 was located between $-0.50 \leq x^* \leq 0$, $\bar{C}_{M,1}$ was strongly counterclockwise because the repulsive $\bar{C}_L$ acted to push the bow of Ellipse 1 outward. Due to the slender geometry of the ellipses and the value of $\bar{C}_D$ generally being lower than $\bar{C}_L$, changes in the drag force did not produce as large of a response in $\bar{C}_M$. The plots of $\Delta\bar{C}_D$, $\bar{C}_L$, and $\bar{C}_M$ all show that there was a smaller interaction

between the ellipses as the lateral distance between them increased.

Additional analysis of the stationary case simulation results, comparison to other studies, and examination of aspect ratio and lift behavior are provided in Chapter 4.

THIS PAGE INTENTIONALLY LEFT BLANK

Chapter 4

Stationary Case Analysis

This chapter provides further analysis pertaining to the stationary case simulations presented in Chapter 3 by comparing the results to those of previous studies, investigating differences in attractive-versus-repulsive lift behavior between hydrodynamic studies, and examining the role of ellipse aspect ratio on force interactions.

4.1 Comparison to 2D Cylinder Results

Interpreting the ellipses used in this study as elongated 2D cylinders, many of the problem parameters (submerged, free-space boundary conditions, close-proximity shapes) were shared in common with the numerical and experimental 2D cylinder studies introduced in Section 1.1.1. One of these studies, Hori [8], provided a useful visualization of the flow field around a cylinder interacting with an identical cylinder at close proximity in a steady cross-flow. The upper half of Figure 4-1 represents values for the upstream cylinder, and the lower half of the figure represents values for the downstream cylinder. Values of yaw moment coefficient were not included in Hori (1959)'s figure.

For comparison to Hori (1959)'s results, a similar representation was created using the ellipse data of the current study. Figure 4-2 shows the results of the stationary simulations from the current study in the form of a quiver plot. The arrows represent vectors of $\Delta\bar{C}_D$ and $\bar{C}_L$ for each ellipse in a given configuration. The strongly vertical

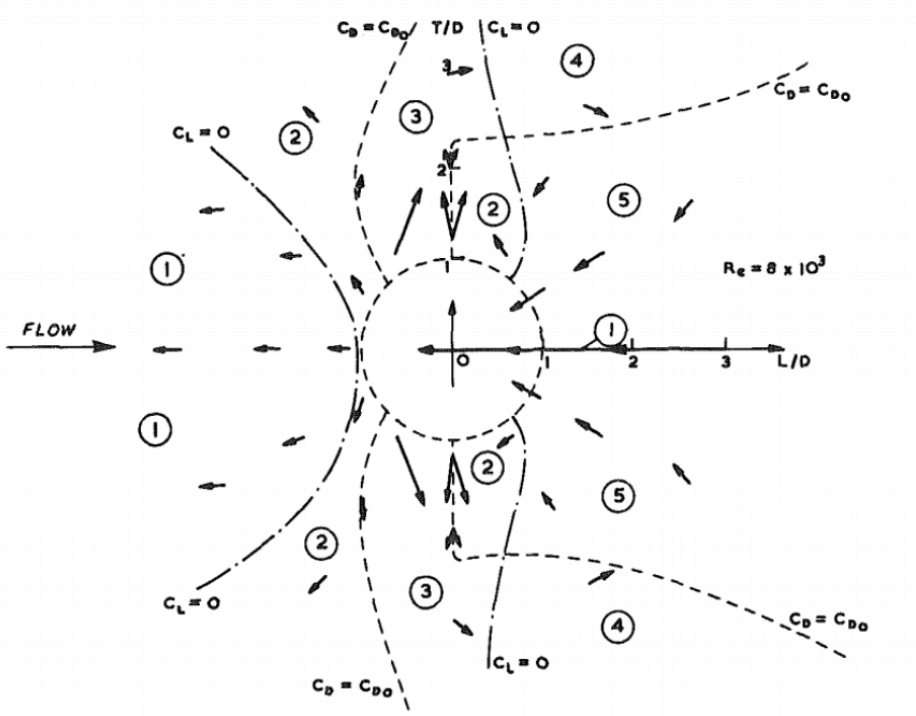

Figure 4-1: Vector plot of lift and drag for all positions from Hori [8], in which two identical cylinders were analyzed in side-by-side, staggered, and tandem configurations

orientation of the arrows at nearly all positions demonstrates the high relative impact of lift interactions in close proximity. The direction of the moment is indicated by the color of the arrow, with red representing $\bar{C}_M > 0$ (counterclockwise) and blue representing $\bar{C}_M < 0$ (clockwise).

Hori (1959) divided the cylinder interactions into five distinct regions, labeled in Figure 4-1. The regions were described as:

1. Negligible lift and reduced drag. Although this region appeared in the current study, it was wider in Hori (1959)'s results. This difference was attributed to the geometry of Hori (1959)'s cylinders, which had a smaller aspect ratio compared to the ellipses used in the current study.

2. Small repulsive lift and reduced drag. This region did not appear in the current study. A repulsive lift force occurred in the echelon region during this study, but it was not accompanied by a reduction in drag as was observed by Hori (1959).

3. Repulsive lift and increased drag. This region also appeared in the current study when the ellipses were located in the side-by-side configuration, along with several neighboring (i.e., nearly side-by-side) configurations.

4. Negligible lift and increased drag. The negligible lift force in this region was consistent with the results of the current study, but the increase in drag was not. The ellipses in the current study exhibited lower interaction in this region compared to the cylinders of Hori (1959)'s study.

5. Negative lift and decreased drag. This region appeared in the current study in the same relative location as in Hori (1959)'s results. The bodies were attracted toward each other in lift, and the downstream body experienced a reduction in drag.

The differences between Figures 4-1 and 4-2 were attributed to two main factors: aspect ratio and Reynolds number. The ellipses used in this study had a higher length-to-width aspect ratio (6:1) compared to the cylinders (1:1), affecting the streamline behavior of the shapes and consequently their drag, lift and yaw moments. For the ellipses, the drag affected the resultant interaction to a lesser extent than it did for cylinders, due to the smaller profile of the ellipses relative to the incoming flow. The lift affected the resultant interaction to a greater extent than it did for cylinders, due to the ellipses having a larger longitudinal surface area over which the repulsive force could act. The effect of the aspect ratio on drag and lift behavior is examined in greater detail in Section 4.5. The Reynolds number used by Hori (1959) was more than five times higher than in the current study (8000 versus 1500, respectively). Although the Reynolds numbers are of the same order of magnitude, viscous characteristics such as vortex shedding are sensitive to changes in Reynolds number and can have a sizeable effect on flow behavior, even within the same order of magnitude [23]. The roles of aspect ratio and Reynolds number can be used to explain differences not just between this study and Hori (1959), but the rest of the 2D cylinder studies (such as those reviewed by Sumner (2010)) as well.

A notable similarity between the results of this study and the 2D cylinder studies

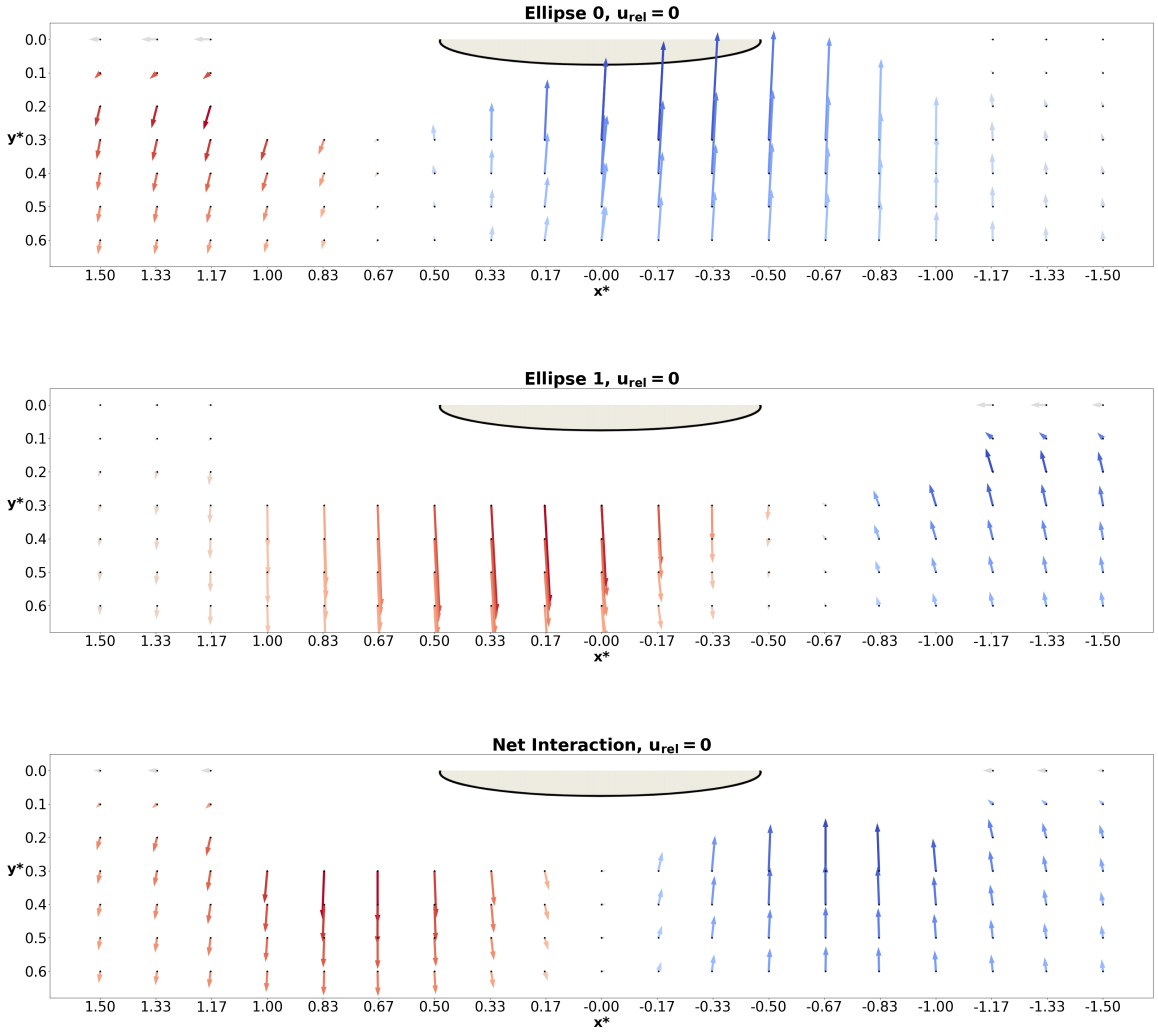

Figure 4-2: Quiver plot of forces and moments. The arrows are force vectors indicating the direction and relative magnitude of the forces acting on each ellipse. Color indicates the moment direction, with red being positive (counterclockwise) and blue being negative (clockwise).

was the behavior of drag coefficient in the side-by-side configuration. Interestingly, this configuration produced a different $\bar{C}_D$ for the two ellipses (a 10.6% increase in $\bar{C}_{D,0}$ and a 23.7% increase in $\bar{C}_{D,1}$ at $y^* = 0.3$). A drag coefficient difference was also noted by Zdravkovich [34] for two identical cylinders arranged side-by-side. Zdravkovich attributed the difference in forces to an asymmetric gap flow that was biased toward one of the cylinders [34]. The cylinder located in the direction of the gap flow bias had a higher drag coefficient compared to the other cylinder, along with a narrower wake and a higher frequency of vortex shedding [34]. In the current study, the gap flow was

always biased toward Ellipse 1, and in accordance with Zdravkovich's observations, Ellipse 1 always experienced a higher $\bar{C}_D$ in the side-by-side configuration. It was expected that the consistent gap flow bias toward Ellipse 1 occurred because the initial free stream perturbation was always in the positive y-direction (i.e., toward Ellipse 0).

Another subject of interest related to the 2D cylinder studies was whether a bistable pattern, in which the gap flow bias spontaneously and irregularly switches direction, would be observed in the side-by-side configuration. A number of studies of side-by-side cylinders (including at least one numerical study, Chen et al. [5]) noted the presence of a bistable pattern [23]. The bias persisted for a long duration (multiple orders of magnitude longer than the vortex shedding period) before switching to the opposite cylinder. Wang et al. [28] showed that the switching of flow bias was related to the build-up and breakdown of a larger gap vortex behind the cylinder opposite the bias [23]. In the bistable arrangement observed by these studies, increasing the flow velocity quickened the onset of switching [23]. A switch in gap flow bias was not observed during the stationary simulations of this study, but the possibility remained that the simulation duration of $t^* = 33.3$ was not long enough to observe a switch. In an attempt to reproduce the switch, the configuration $(x^*, y^*) = (0.00, 0.3)$ was run for three times the duration of a normal simulation ($t^* = 99.9$), and the Reynolds number was increased to 2250, but no switch in flow bias was observed. The lack of a switch in flow bias agreed with the findings of two experimental studies, Peschard and Gal [15] and Sumner et al. [24], who did not observe bistability [23]. The position of the ellipses with respect to the computational grid nodes may have played a role in the lack of a switch: if the ellipse centroids were not perfectly aligned with the nodes, a numerical asymmetry may have occurred in the solution that caused the flow to always be biased in the same direction.

4.2 $\Delta\bar{C}_D$ Regions and Comparison to RANS UUV Results

The results of the stationary simulations were compared to investigations by Rattanasiri et al. [17] and Tian et al. [25] of two stationary UUVs in a constant, viscous flow. The UUV studies were similar to the current study in their motivation to characterize interactions between bodies in close proximity at different configurations. One difference was that the UUV studies performed RANS simulations using 3D shapes (prolate spheroids) instead of 2D shapes (ellipses) to represent UUVs. Another difference was that the UUV studies used turbulent Reynolds numbers ($Re = \mathcal{O}(10^6)$) that were three orders of magnitude higher than the laminar Reynolds number used in the current study ($Re = \mathcal{O}(1000)$). The dimensional and Reynolds number differences limited the usefulness of direct quantitative comparison, but similar qualitative patterns of drag interaction behavior were observed between studies.

In a manner similar to Figures 1-2 and 1-3 provided by Rattanasiri et al. (2014) and Tian et al. (2017), respectively (see Section 1.1.2), the results of the various ellipse configurations were divided into regions based on the $\Delta\bar{C}_D$ of each ellipse, as well as the overall effect on $\Delta\bar{C}_D$ of the system. Figure 4-3 shows the drag interaction regions determined by the current study.

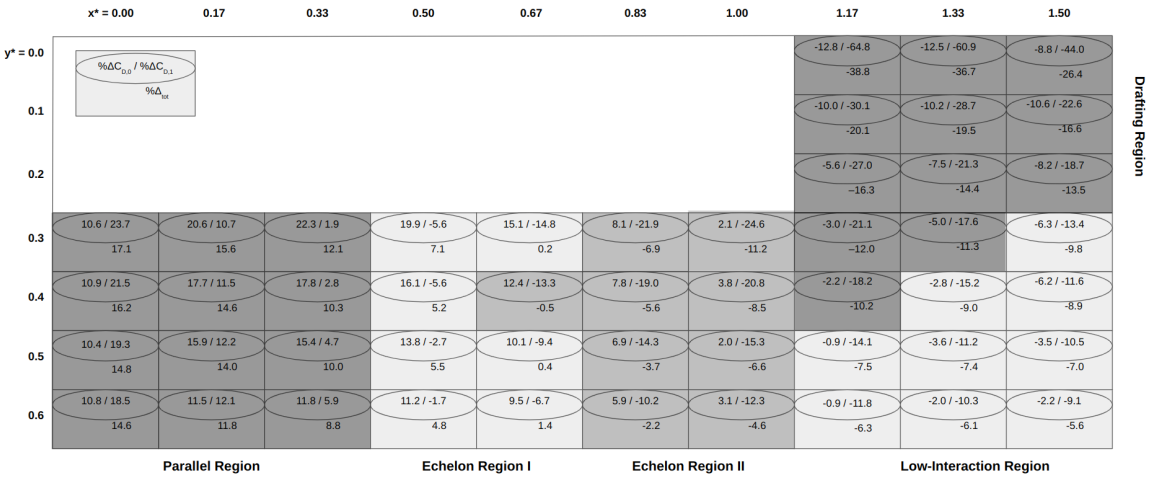

Figure 4-3: Regions of interaction with respect to $\Delta\bar{C}_D$ for the current study

Table 4.1 lists the name, location, and description of each interaction region. Figure 4-4 shows an image of one configuration from each interaction region. A discussion of each region is provided in the sections below.

Table 4.1: Interaction regions with respect to $\Delta\bar{C}_D$

Stationary Case					
Region	$\boldsymbol{x^*}$	$\boldsymbol{y^*}$	$\boldsymbol{\Delta C_{D,0}}$	$\boldsymbol{\Delta C_{D,1}}$	$\boldsymbol{\Delta_{sys}}$
Parallel	0,-0.33	0.3-0.6	+	+	+
Echelon I	-0.50 -0.67	0.3-0.5 0.3, 0.5-0.6	+	-	+
Echelon II	-0.67 -0.83 -1.00	0.4 0.3-0.6 0.3-0.6	+	-	-
Drafting	-1.17 -1.33 -1.50	0.0-0.4 0.0-0.3 0.0-0.2	-	-	-
Low-Interaction	-1.17 -1.33 -1.50	0.5-0.6 0.4-0.6 0.3-0.6	-	-	- (<10%)

Parallel In the parallel region, where the ellipses were side-by-side (or nearly side-by-side), both ellipses experienced an increase in $\Delta\bar{C}_D$, and there was a corresponding increase in $\Delta\bar{C}_D$ for the system. This region saw the maximum increase in $\Delta\bar{C}_{D,0}$ (22.3% at $(x^*, y^*) = (-0.33, 0.3)$) and $\Delta\bar{C}_{D,1}$ (23.7% at $(x^*, y^*) = (-0.00, 0.3)$), as well as the maximum drag increase for the overall system (17.1% at $(x^*, y^*) = (0.00, 0.3)$) out of all configurations. The round, streamlined shape of the ellipses caused the average velocity outside of the boundary layer to increase, producing a positive pressure gradient along the rear that increased drag. The gap between the two ellipses functioned as a nozzle whose expansion ratio increased as the lateral separation decreased, causing flow separation to occur further upstream. This effect was similar to what was described by Hoerner [7] for a pair of struts.

Echelon I In the echelon region, where one ellipse trailed at least half a length behind the other but remained overlapped, the upstream ellipse experienced an

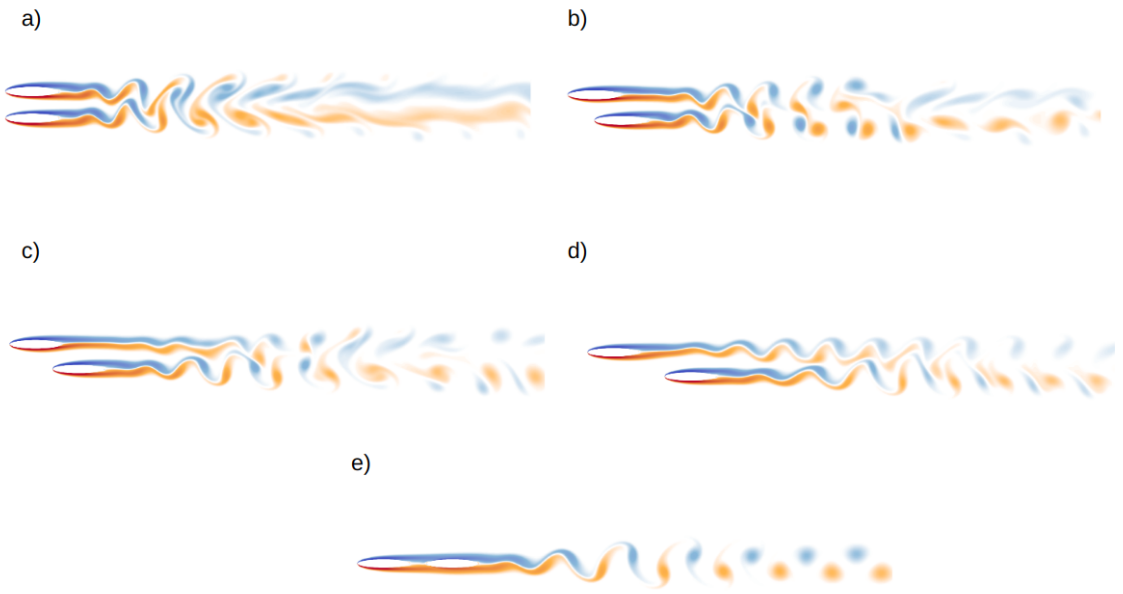

Figure 4-4: Image of one configuration from each interaction region, ordered as follows: (a) Parallel, $(x^*, y^*) = (0.00, 0.5)$ (b) Echelon I, $(x^*, y^*) = (-0.50, 0.5)$ (c) Echelon II, $(x^*, y^*) = (-0.83, 0.5)$ (d) Low-Interaction, $(x^*, y^*) = (-1.50, 0.5)$ (e) Drafting, $(x^*, y^*) = (-1.33, 0.0)$

increase in $\Delta\bar{C}_D$, while the downstream ellipse experienced a decrease in $\Delta\bar{C}_D$. The largest increase in the Echelon I region in $\Delta\bar{C}_{D,0}$ was 19.9% and occurred at $(x^*, y^*) = (-0.50, 0.3)$, while the largest decrease in $\Delta\bar{C}_{D,1}$ was 14.8% and occurred at $(x^*, y^*) = (-0.67, 0.3)$. In the Echelon I region, there was a net increase in $\Delta\bar{C}_D$ for the overall system, meaning that the drag increase on Ellipse 0 was greater than the drag decrease on Ellipse 1. The largest overall increase of 7.1% occurred at $(x^*, y^*) = (-0.50, 0.3)$ (coinciding with the maximum increase in $\Delta\bar{C}_{D,0}$), and the smallest overall increase of 0.2% occurred at $(x^*, y^*) = (-0.67, 0.3)$ (coinciding with the maximum decrease in $\Delta\bar{C}_{D,1}$). The echelon region occurred due to the pressure and skin friction distributions around the ellipses creating a net attraction, resulting in the ellipses being "pulled" toward each other. The upstream ellipse was pulled slightly backward, and the downstream ellipse was pulled slightly forward. The echelon region is a common position for dolphin and whale calves to swim with their mothers, because it provides the calf with a swimming advantage and pulls it closer toward

the mother's flank to prevent the two from being separated [21]. For UUVs, the echelon position may be useful if one UUV is damaged or low on power and the other is fully operational.

Echelon II The second echelon region was similar to the first echelon region, except that there was a net decrease in $\Delta\bar{C}_D$ for the overall system, due to the drag increase for Ellipse 0 being less than the drag decrease for Ellipse 1. This effect was most pronounced at $(x^*, y^*) = (-1.00, 0.3)$, where $\Delta\bar{C}_{D,0}$ increased by 2.1% and $\Delta\bar{C}_{D,1}$ decreased by 24.6%, giving an overall drag decrease of 11.2% for the system. The Echelon II region may be viewed as a transitional area between one-sided drag benefit to the downstream ellipse (as in the echelon region) and mutual drag benefit to both ellipses (as in the drafting region and most of the low-interaction region).

Low-Interaction In the low-interaction region, the ellipses were spaced relatively far apart, causing the magnitude of interaction to be smaller. There was generally a small drag benefit to both ellipses (and, by extension, the overall system), as seen in the drafting region. In the furthest-spaced configuration that was simulated $(x^*, y^*) = (-1.50, 0.6)$, $\Delta\bar{C}_{D,0}$ decreased by 2.2%, $\Delta\bar{C}_{D,1}$ decreased by 9.1%, and the overall system drag decreased by 5.6%. The low level of interaction was attributed to the fact that there was less overlap between the ellipse bodies and wakes, causing the trailing ellipse to lose much of the benefit experienced via the "pull" interaction in the echelon and drafting regions. If spacing were to increase further, it is expected that this region would transition toward what Rattanasiri et al. [17] referred to as a "no-interaction" region. In this region, the forces on each ellipse would begin to exhibit "far-field" behavior resembling a single, isolated ellipse in a free stream.

Drafting In the drafting region, where one ellipse was located fully behind (and in some configurations, tandem to) the other ellipse, both ellipses experienced a decrease in $\Delta\bar{C}_D$, and there was an overall $\Delta\bar{C}_D$ decrease for the system. The mutual drag benefit was most pronounced at $(x^*, y^*) = (-1.17, 0.0)$, where the

maximum decreases in $\Delta\bar{C}_{D,0}$ (12.8%), $\Delta\bar{C}_{D,1}$ (64.8%), and the system (38.8%) across all configurations occurred. The downstream ellipse was located within the wake of the upstream ellipse, increasing the static pressure between the two and "pushing" the upstream ellipse forward. Meanwhile, the downstream ellipse was located in a lower-pressure region compared to the free stream, causing it to be "pulled" forward. The flow tended to separate from the rear of the downstream ellipse due to the momentum deficiency within the wake of the upstream ellipse, causing the wake to behave as though it were coming from a single, extended body [23]. The tandem configuration in particular provides the largest mutual drag benefit and has served as the topic of previous UUV studies such as Zhang et al. [36]. However, it should be noted that despite their apparent drag advantage, the drafting configurations are not necessarily the most conducive to efficient UUV operations; the simulations assumed the absence of any propeller effects, which may inhibit maneuverability or eliminate any hydrodynamic benefits in this region.

The drag interactions observed in this study qualitatively resembled those found in Rattanasiri et al. (2014) and Tian et al. (2017). A notable exception was that the push region identified by Rattanasiri et al. (2014) in the closest tandem configuration of $(x^*, y^*) = (-1.17, 0.0)$ was not observed in the results of this study. Apart from the large difference in Reynolds number (which did not otherwise affect the drag interaction regions in a significant way), the lack of a push region could be attributed to limitations in the chosen grid resolution between ellipses at the closest spacing, or a small difference in the flow characteristics of 2D versus 3D at this location. However, the inconsistency at this configuration is not particularly relevant to the UUV application because neither simulation accounted for propeller effects, which are expected to make a sizable difference in the flow characteristics when one UUV is positioned in the wake of the other.

It should be noted that the drag interaction results did not account for the cost of maneuvering the ellipses to maintain a constant relative configuration. It is expected that any drag benefits observed in the results would be reduced due to the need to

counteract the lift force that repels or attracts the ellipses. Steering would create a change in the angle of attack, which is known to increase drag coefficient [20]. On account of its relevance to real-life UUV operations, the cost of maneuvering problem is recommended in Section 8.1 as a topic for further study.

The comparison to UUV studies so far has been focused on drag coefficient. Rattanasiri et al. (2014) and Tian et al. (2017) focused mainly on drag, but other RANS studies such as Zhang et al. (2019a) (UUVs) and Yuan et al. (2015) (ships) included lateral (lift) force, and their results differed markedly from the results of lift coefficient in the current study. The differences in lift behavior between various stationary studies serve as a topic of discussion in Section 4.3.

4.3 $\bar{C}_L$: Attraction Versus Repulsion

The results of lift force coefficient in the stationary case created a divide between the 2D studies (including the current study), which were performed using free-space boundaries and laminar flow regimes, and the results of the 3D studies, which were performed using either smooth or standard wall conditions and turbulent flow regimes. The characteristics and possible causes of attractive versus repulsive behavior are explored in this section.

4.3.1 $\bar{C}_L$ Behavior at Different Reynolds Numbers

The lift interactions observed in the current study tended to agree with experimental and numerical studies of 2D cylinders that were performed at similar Reynolds numbers (generally $\mathcal{O}(10^3 - 10^4)$, with a few studies at $\mathcal{O}(10^2)$). Comparing the quiver plot in Figure 4-2 to the results of Hori (1959) in Figure 4-1, there generally existed a repulsion between the two bodies when they were side-by-side, and an attraction when the bodies were staggered by more than half a body length in the x-direction. The cylinder studies reviewed by Sumner [23] also observed repulsion in the side-by-side configuration, with the exception of one configuration in Alam et al. [1], where an attractive force was detected for an extremely small gap ratio of $T/D = 0.10$

(see Section 1.1.1). Repulsion in the side-by-side configuration at lower Reynolds numbers may be attributed to the presence of low velocity, high-pressure points on the inward side of the ellipses. These points are located both at the opening of the nozzle between the ellipses and at the separation point, which occur further upstream due to the gap flow. The gap flow between the ellipses also causes the flow velocity around the outside of the ellipses to increase, creating a low-pressure area that pulls the ellipses outward and away from each other.

In contrast to the 2D cylinder studies, the lift results of RANS studies performed at higher (turbulent) Reynolds numbers ($\geq \mathcal{O}(10^6)$) [35; 33] were nearly opposite to those observed in the current study. In the RANS studies, the lateral forces in the side-by-side configuration tended to be attractive. If differences in Reynolds number are considered in isolation from other effects, the attraction may be attributed to the later flow separation at higher Reynolds numbers, which eliminates the source of repulsion seen at lower Reynolds numbers and results in the Bernoulli effect dominating the lift force:

$$P_1 + \frac{\rho v_1^2}{2} + \rho g h_1 = P_2 + \frac{\rho v_2^2}{2} + \rho g h_2. \tag{4.1}$$

In equation 4.1, P is the pressure, v is the flow velocity, g is acceleration due to gravity, and h is the vertical elevation. The subscripts 1 and 2 denote separate positions along a streamline in steady flow. Considering the so-called "Bernoulli effect," the small gap size at parallel configurations such as $x^* = 0$ caused the velocity to reach a maximum and the pressure to reach a minimum, producing a peak in attractive lift.

Comparing the results of lift coefficient from this study to higher-Re studies suggests the presence of a transition in lift interactions between the laminar and turbulent regimes. A study of ellipses or ellipsoids at Reynolds numbers between $\mathcal{O}(10^4 - 10^5)$ could help to identify and characterize this shift. Although the 2D cylinder studies cover this range of Reynolds numbers and do not observe a shift toward attractive lift forces, acquiring data for ellipses at this range would help to rule out any possible effects of body geometry (i.e., aspect ratio). A Reynolds number-related transition in lift interactions would be relevant to UUV operations, as the transition may overlap

with Reynolds numbers that are encountered by small UUVs moving at low speeds. With this in mind, it is proposed that future studies aim to simulate a wider range of Reynolds numbers up to and including turbulent regimes (see Section 8.1).

4.3.2 $\bar{C}_L$ Behavior Under Periodic Boundaries

Apart from differences in Reynolds number, another possible source of the difference in lift behavior between studies was the type of boundary conditions that were imposed on the flow. The results of the 2D cylinder studies and the current study – both using free-space boundary conditions – showed a repulsive lift in the side-by-side configuration. Conversely, the results of the stationary UUV studies showed an attractive lateral force when the UUVs were side-by-side. The wall boundaries used both in tow tank tests [10] and in numerical simulations [10; 25; 17] of the UUV studies may have constrained the flow such that it affected the lift forces. To investigate the role of boundary conditions on lift behavior, a series of "constraint test" simulations were performed. The goal of these simulations was to determine if the attractive lift observed in the side-by-side configuration by the UUV studies could be reproduced by introducing periodic boundary conditions and changing the lateral spacing between the ellipses. If the attractive lift could be reproduced, an additional goal was to characterize the transition between attractive and repulsive lift.

Consider the case of the stationary simulations, except that the ellipses are now in a constrained channel as shown in Figure 4-5. The boundary conditions of the channel are periodic, so that the domain is considered to infinitely repeat itself in all directions. The two ellipses are arranged side-by-side ($x^* = 0$), and there is an inflow of U_∞ in the negative x-direction (left to right) so that the Reynolds number $Re = U_\infty L/\nu = 1500$. The gap size between the ellipses is denoted as d_1 and the ellipses are vertically centered on the domain. The space between each ellipse and the nearest (top or bottom) boundary is $d_2/2$, where d_2 is the distance between the ellipse and the "mirrored" ellipse in the next periodic cell. Therefore, when $d_1/d_2 = 1$, the ellipses are equidistant to each other and their mirrored images.

The flow was run under these conditions until the ellipse wakes reached a sym-

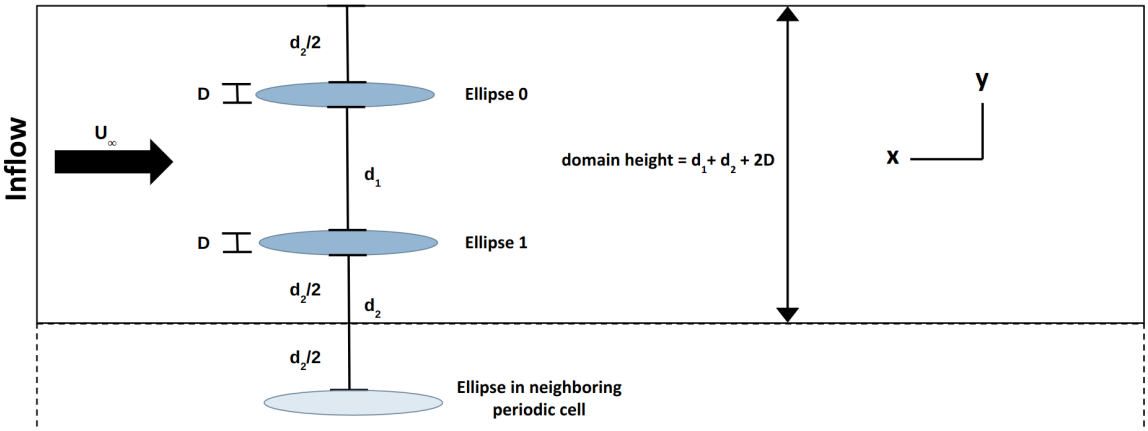

Figure 4-5: Setup of a constrained channel for the two ellipses, using periodic boundary conditions

metric, steady state. The lift coefficients were averaged over time, as in the original stationary simulations. Particular attention was paid to the signs of of $\bar{C}_{L,0}$ and $\bar{C}_{L,1}$, as the attraction or repulsion between ellipses served as the focus of these simulations. Figure 4-6 shows the results of the constraint test at several values of d_1/d_2. When the gap size between the ellipses was smaller (i.e., $d_1/d_2 < 1$), there was an attractive lift force ($\bar{C}_{L,0} < 0$ and $\bar{C}_{L,1} > 0$). The constrained flow was forced to move through the space between the ellipses to a greater extent than in previous simulations, where there were no such boundary constraints. This redirection of flow resulted in a higher velocity and lower pressure between the ellipses that produced attraction. A transition in the lift interactions occurred at $\sim d_1/d_2 = 1$, after which $\bar{C}_L$ became repulsive ($\bar{C}_{L,0} > 0$ and $\bar{C}_{L,1} < 0$). The results of these simulations suggest that periodic boundary conditions are capable of changing flow behavior to produce either an attractive or repulsive lift – even at the relatively low Reynolds number of 1500 used in this study. These observations may help to explain differences between the lift coefficient results of the stationary UUV studies and the results of this study. The lift behavior of several stationary studies is summarized in Table 4.2.

Although the constraint test results show that boundary conditions play a role in lift behavior for this problem, the effect of periodic boundaries on lift behavior at higher Reynolds numbers remains unknown. It is possible that increasing the Reynolds numbers simply magnifies the attractive or repulsive forces, or that it affects

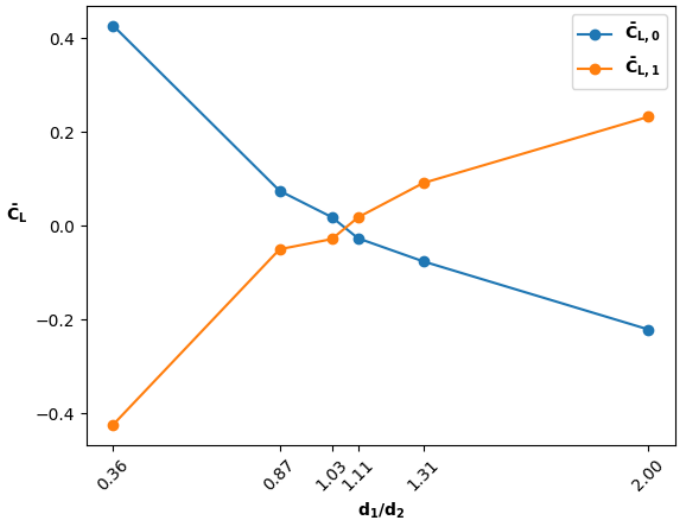

Figure 4-6: Lift behavior of side-by-side ellipses under periodic boundary conditions

where the shift between attractive and repulsive forces occurs with respect to d_1/d_2. A set of simulations similar to the constraint test would be useful to determine the role of periodic boundaries at different Reynolds numbers with greater certainty.

4.4 $\bar{C}_M$ and Implications for Maneuvering

Based on Figure 4-2, the orientation of the moment was clearly driven by the vector direction and ellipse position. The moment was reduced to zero and reversed direction in areas where the lift of one ellipse changed direction, including at $x^* = 0.67$ for $\bar{C}_{M,0}$ and at $x^* = -0.67$ for $\bar{C}_{M,1}$. There was a shift in moment when the ellipses passed abeam of each other ($x^* \approx 0$), since the change in relative position caused the interactions to be biased toward the opposite side of the ellipse (forward instead of aft for Ellipse 0, and aft instead of forward for Ellipse 1). This shift created a peak in the magnitude of $\bar{C}_{M,0}$ (-0.130 at $x^* = -0.17$) and $\bar{C}_{M,1}$ (0.130 at $x^* = 0.17$, on account of symmetry).

In the way of comparison to existing findings, the yaw moment was not generally included in the 2D cylinder studies, but it did appear in Zhang et al. (2019a)'s study of UUV overtaking, which was performed using a stationary approach as in Chapter 3. In Zhang et al. [35], the yaw moment for the "passing" UUV (akin to Ellipse 1) was

Table 4.2: Comparison of lateral force results for bodies in the side-by-side configuration from various studies

Author	**Description**	**Re**	**Boundary Type**	$\boldsymbol{C_L}$ **at** $\boldsymbol{x^* = 0}$
Current Study	Identical ellipses (2D)	$\mathcal{O}(10^3)$	Free	Repulsive
Hori (1959)	Identical cylinders (2D)	$\mathcal{O}(10^3)$	Free	Repulsive
Sumner (2010)	Identical cylinders (2D)	$\mathcal{O}(10^2 - 10^4)$	Free	Repulsive
Current Study	Identical ellipses (2D)	$\mathcal{O}(10^3)$	Periodic; narrow channel	Attractive
Romberg et al. (1971)	Race cars (3D)	$\mathcal{O}(10^7)$	Standard Wall (Wind Tunnel)	Attractive
Tian et al. (2017)	Two identical UUVs (3D)	$\mathcal{O}(10^6)$	Smooth Wall (no shear)	Attractive
Leong et al. (2013)	UUV & larger submarine (3D)	$\mathcal{O}(10^6)$	Standard Wall (Tow Tank)	Attractive
Zhang et al. (2019a)	UUV & larger UUV (3D)	$\mathcal{O}(10^6)$	Smooth Wall (no shear)	Attractive

driven by the low pressure created between the two bodies, which was also responsible for the attractive lift force. Accordingly, when the bodies were located within half a length of each other ($|x^*| < 0.5$) and experienced attractive lift, the passing UUV was pulled bow-in for $x^* < 0$ and then stern-in for $x^* > 0$. Differences between the yawing behavior in Zhang et al. (2019a) and the current study were mainly attributed to the attractive-versus-repulsive differences in lift (see Section 4.3) and the fact that $\bar{C}_M$ was dominated by $\bar{C}_L$ due to the elongated, streamlined shape of the UUVs and ellipses.

The yaw moment behavior of the bodies was also a subject of interest in studies of ship overtaking. Comparison to these ship studies will be reserved for the overtaking simulations in Chapters 6 and 7, on account of their inclusion of relative velocity.

4.5 Aspect Ratio Effects

Analysis of the stationary case and comparison to studies of 2D cylinder pairs raised questions about the role of ellipse aspect ratio in hydrodynamic interactions. It was not known if changing the aspect ratio would affect the velocity of flow around and between bodies or the location of the separation point – both of which impact drag and lift. Although the cylinder studies and the current study largely agreed on interaction behaviors, differences between the results – such as those between Hori (1959) and the current study – warranted explanation. As noted in Section 4.1, it was suspected that a relationship existed between aspect ratio and $\bar{C}_D$ or $\bar{C}_L$ that accounted for some of the differences between results.

A series of simulations were performed at different lateral separations in the side-by-side configuration. The value of aspect ratio was manipulated by changing the length of the ellipses while keeping the diameters equivalent. Equation 4.2 shows the calculation for aspect ratio:

$$AR = L/D, \tag{4.2}$$

where L is the length of the ellipse (subject to manipulation) and D is the diameter (kept constant for all simulations). The lateral separation values were kept constant between aspect ratios and were based on the values of y^* for $AR = 6$. The explicit values used were $y = \{0.36, 0.48, 0.60, 0.72\}$, which corresponded to $y^* = \{0.3, 0.4, 0.5, 0.6\}$ at $AR = 6$, respectively.

Figure 4-7 shows a plot of aspect ratio AR versus time-averaged drag coefficient $\bar{C}_D$ for side-by-side ellipses at various lateral separations. The first plot uses L as the principal dimension to normalize drag coefficient ("L-norm"), as in the rest of the simulations of this study. The second plot uses a normalizing dimension of diameter D ("D-norm"), which remained constant as the length was varied to manipulate aspect ratio. The D-norm value was obtained by multiplying the L-norm result by the aspect ratio: $\bar{C}_D * AR$. The D-norm plot shows that the drag scaled asymptotically at higher aspect ratios when normalized with the diameter. This relationship occurred due to an increase in the length over which the incoming flow came into contact with the

ellipse, causing the drag to shift from bluff-body characteristics (pressure drag) to flat-plate characteristics (friction drag). The L-norm plot shows that the greater lengths at higher AR caused $\bar{C}_D$ to approach zero.

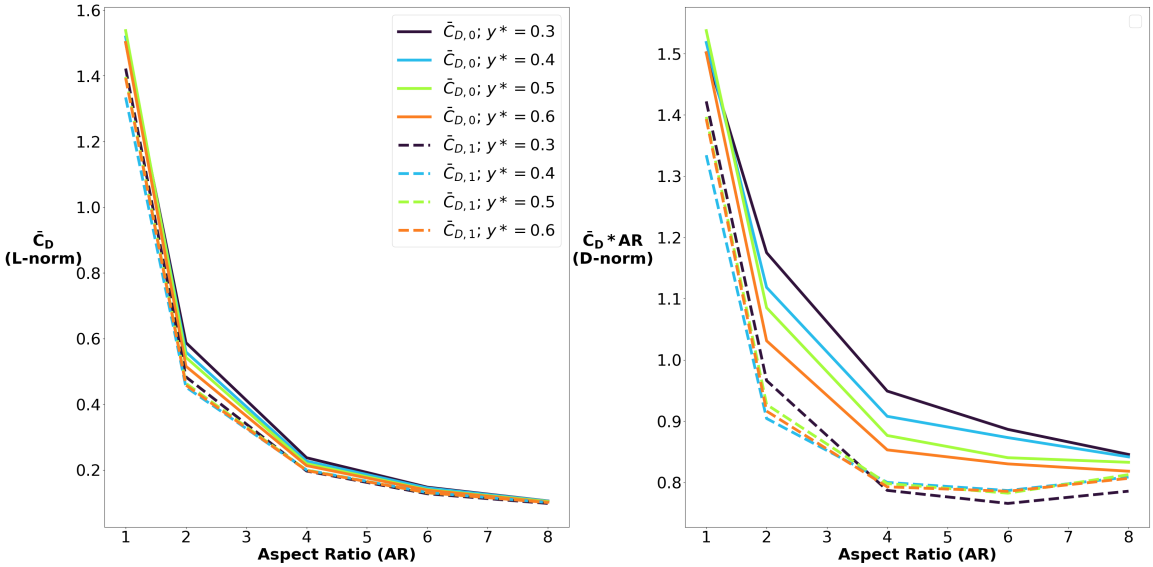

Figure 4-7: Plot of aspect ratio versus $\bar{C}_D$ for side-by-side ellipses at various values of lateral separation y^*.

Figure 4-8 shows a plot of aspect ratio AR versus time-averaged lift coefficient $\bar{C}_L$ for side-by-side ellipses at various values of y^*. The plot uses data from the same simulations as Figure 4-7. The L-norm plot shows that the lift scaled asymptotically at higher aspect ratios when normalized with length. This occurred because the greater surface area led to an increase in lift that stabilized at higher AR. The D-norm plot shows that the lift scaled linearly at higher aspect ratios when normalized with diameter. This relationship served as evidence that the flow-rate distribution between the ellipses did not change between values of AR. If the rate of flow between the ellipses did not change, then there was no change in pressure; therefore, the only variable affecting lift force that changed between values of AR was the surface area (length) of the ellipses. By the relationship $F = P/A$ – where F is the applied force, P is the pressure, and A is the surface area (or the length in 2D) – the applied lift force (and, by extension, $\bar{C}_L$) changed linearly with respect to the aspect ratio of the ellipses. $\bar{C}_L$ was repulsive in all of the simulations.

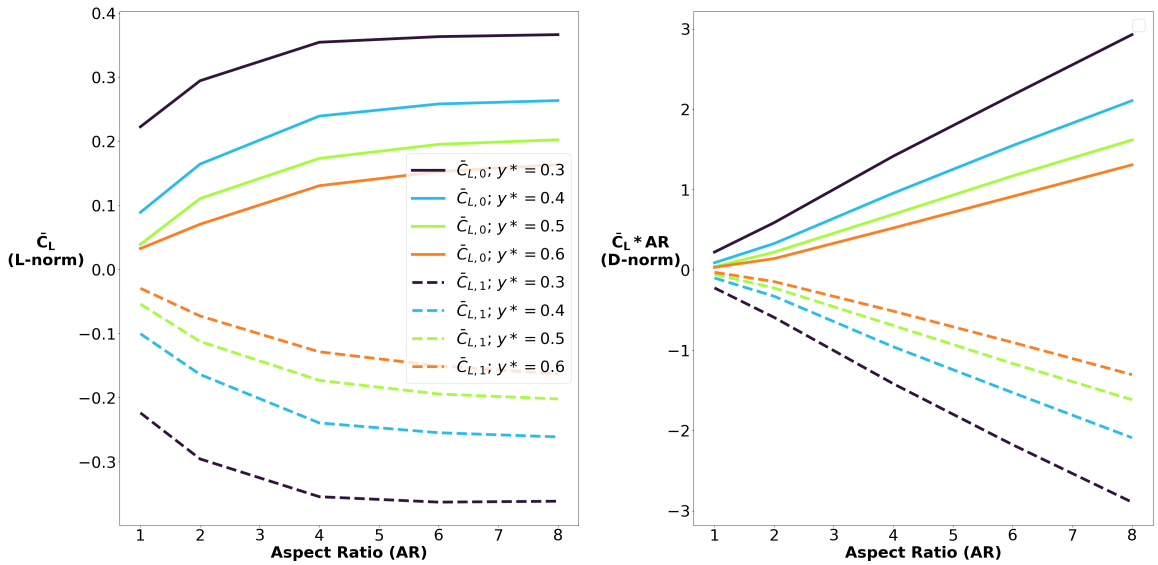

Figure 4-8: Plot of aspect ratio versus $\bar{C}_L$ for side-by-side ellipses at various values of lateral separation y^*.

The aspect ratio simulations showed that under constant flow conditions, there existed a predictable relationship between the drag and lift coefficients and the aspect ratio of an ellipse. $\bar{C}_D$ scaled asymptotically when normalized with the ellipse diameter, due to the dominance of friction drag at higher AR. $\bar{C}_L$ scaled asymptotically when normalized with the ellipse length, as the greater surface area led to an increase in lift that stabilized at higher AR. The results also showed that changing the aspect ratio on its own did not change the direction of lift interactions between ellipses in the side-by-side configuration. Although the attraction-versus-repulsion phenomenon was not explained by aspect ratio, the simulations helped to connect the well-characterized cylinder results of drag and lift with those of the current study.

4.6 Stationary Case Takeaways

The stationary case simulations served to characterize ellipse force interactions in a rotational, viscous flow at constant velocity. The force and moment interactions between the ellipses were mapped at several close-proximity configurations and compared to existing studies of UUVs and 2D cylinders that shared a similar approach. The drag interactions between ellipses were largely consistent with UUV studies per-

formed in turbulent regimes, and showed that depending on the positions of the ellipses, the drag interaction was either mutually beneficial (drafting), detrimental (parallel), benefited one ellipse (echelon), or did not produce a significant on either ellipse (low-interaction). The echelon configuration led to as much as a $\sim 20\%$ drag decrease for the downstream ellipse at the cost of a similar increase for the upstream ellipse. In most configurations, the lift force on both ellipses was significantly (up to four times) larger than the drag force. In a practical application, this means that the lift will dominate the force interactions, which has strong implications in terms of having to maneuver the ellipses to maintain their formation.

The drag and lift behaviors were largely similar to the findings of Hori (1959)'s 2D cylinder study at a Reynolds number of the same order ($\mathcal{O}(1000)$). The effect of viscosity on ellipse interactions in the subcritical ($Re = 1500$) regime was evident, with the lift behavior differing from observations of studies at turbulent Reynolds numbers, where pressure-driven phenomena tended to dominate. A divide existed between the results of the RANS UUV/ship studies and the 2D cylinder/ellipse studies regarding whether the lift interaction between bodies was attractive or repulsive. The divide may be attributable to differences in Reynolds number and boundary conditions that dictated how much of the flow was directed between the ellipses (causing attraction via Bernoulli suction) versus around the ellipses (causing repulsion due to lower pressure on the outboard side). Indeed, a set of simulations using a narrow domain width and periodic boundary conditions showed that in a constrained flow, the interaction between the ellipses was either repulsive or attractive depending on how far the ellipses were separated from each other and from the domain boundary. A similar set of simulations at higher Reynolds numbers would help to ascertain whether the lift interactions are a function of boundary conditions, Reynolds number, or both.

Chapter 5

Periodic Array Simulations

This chapter describes a set of simulations that investigated ellipse interactions in an infinitely repeating grid. Ellipse configurations were chosen from the stationary simulations and repeated using unit cells of one or two ellipses, which were made to repeat infinitely through the use of periodic boundary conditions. The results were compared to the stationary case results and used to model how UUVs would interact in a large formation such as a fleet or swarm.

5.1 Approach

A similar set of parameters to the stationary case simulations were used, except that periodic boundary conditions were enforced instead of free-space boundary conditions. The reference domain that was repeated infinitely in the simulations was referred to as the unit cell. To make the configuration repeat infinitely, the spacing between ellipses in adjacent cells was kept consistent. This was done by sizing the domain length and width to match the desired relative spacing between ellipses in adjacent cells. As a result, the spacing between the ellipses and the domain boundary was significantly smaller than in the stationary case, and it was necessary to increase the grid resolution used for calculations to maintain numerical accuracy. Sample "factory" and "settings" files for the periodic array simulations are included in Appendix A.

The configurations used in the periodic array simulations were chosen to represent

a variety of possible drag interactions and to more easily compare results to the stationary case. Note that the echelon region could not be reproduced, because for the periodic cell to be repeatable, the ellipses had to be placed greater than one body length apart in the x-direction, so that the unit cell could be repeated while maintaining equal spacing between all ellipses without overlap. The sections below discuss the two main arrangements that were used: axis-aligned and staggered.

5.2 Axis-Aligned

In the stationary case, the parallel region produced a drag increase for both ellipses, an effect that was most pronounced when the ellipses were located side-by-side. Conversely, the drafting region produced a drag decrease for both ellipses, especially when the ellipses were located tandem to each other. There was an interest in which of these drag effects would outweigh the other in an infinitely repeating arrangement. In the periodic array simulations, the side-by-side and tandem configurations were represented simultaneously by using a single ellipse in the unit cell. This arrangement was referred to as "axis-aligned."

To prepare the axis-aligned simulations, a single ellipse was placed at the center of the domain in the unit cell. The domain was sized to produce the desired spacing between ellipses in adjacent cells. The effect was an infinite fleet of identical ellipses spaced at the same distance (x^* and y^*) from each other. For example, if the unit cell was sized $x^* = 1.50$ in length and $y^* = 0.3$ in width, then the individual ellipses at the center of each cell were also spaced this far apart. Figure 5.1 provides a generic illustration of the axis-aligned approach. The simulated configurations were: $(x^*, y^*) = (-1.50, 0.3)$, $(x^*, y^*) = (-1.50, 0.6)$, $(x^*, y^*) = (-1.17, 0.3)$, and $(x^*, y^*) = (-1.17, 0.6)$.

Table 5.1 shows the results of the axis-aligned simulations. $\bar{C}_D$ was found to be higher at larger longitudinal offsets ($x^* = -1.50$) and smaller lateral offsets ($y^* = 0.3$). The values of $\bar{C}_L$ and $\bar{C}_M$ were found to be less than 0.005 in all simulations due to the symmetry of the vertical spacing between ellipses in adjacent cells.

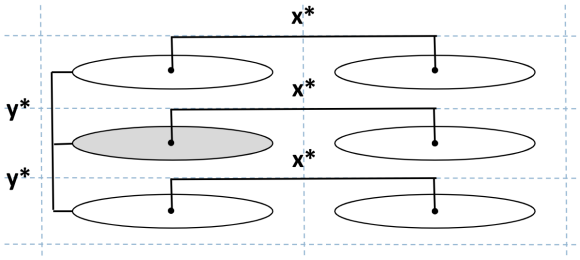

(a) Axis-aligned arrangement, featuring a single-ellipse unit cell (darker ellipse) and adjacent periodic image cells (lighter ellipses)

(x^*, y^*)	$\bar{C}_{D,fleet}$
$(-1.17, 0.3)$	0.495
$(-1.17, 0.6)$	0.072
$(-1.50, 0.3)$	0.770
$(-1.50, 0.6)$	0.203

(b) Drag coefficient results of axis-aligned simulations

Figure 5-1 & Table 5.1: Illustration and results of axis-aligned simulations

5.3 Staggered

In the stationary case, the drafting region produced a drag decrease for both ellipses. The low-interaction region produced a similar effect as the drafting region, albeit with an overall drag benefit to the system of less than ten percent. There was an interest in whether the ellipses would interact in a similar manner when placed in drafting and low-interaction configurations within an infinitely repeating system. In the periodic array simulations, these configurations could be represented by placing two ellipses within the unit cell. This arrangement was referred to as "staggered."

To prepare the staggered simulations, two ellipses were placed at the desired relative spacing (x^* and y^*) within the unit cell. As in the axis-aligned simulations, the domain was sized to produce the desired spacing between ellipses in adjacent cells. Figure 5.2 provides a generic illustration of the staggered approach. The simulated configurations were: $(x^*, y^*) = (-1.50, 0.3)$, $(x^*, y^*) = (-1.50, 0.6)$, $(x^*, y^*) = (-1.17, 0.3)$, and $(x^*, y^*) = (-1.17, 0.6)$.

Table 5.2 shows the results of the staggered simulations. The value of $\bar{C}_{D,fleet}$ is the average of the two ellipses from the simulation, as the values of $\bar{C}_{D,0}$ and $\bar{C}_{D,1}$ varied slightly in the simulations at $x^* = -1.17$ due to domain size inaccuracies and flow bias. The values of $\bar{C}_L$ and $\bar{C}_M$ were found to be less than 0.005 in all simulations due to the symmetry of the vertical spacing between ellipses in adjacent cells.

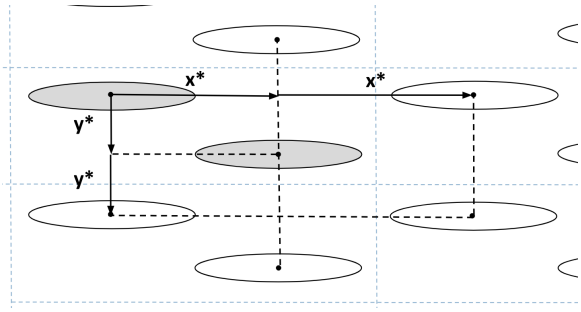

(a) Staggered arrangement, featuring a two-ellipse unit cell (darker ellipses) and adjacent periodic image cells (lighter ellipses)

(x^*, y^*)	$\bar{C}_{D,fleet}$
$(-1.17, 0.3)$	0.225
$(-1.17, 0.6)$	0.116
$(-1.50, 0.3)$	0.249
$(-1.50, 0.6)$	0.122

(b) Drag coefficient results of staggered simulations

Figure 5-2 & Table 5.2: Illustration and results of staggered simulations

5.4 Comparison to Stationary Simulations

A comparison between the results of the axis-aligned simulations and their most similar configurations in the stationary case is provided in Table 5.3. The results are compared using the corresponding side-by-side ($x^* = 0$) and tandem ($y^* = 0$) configurations. For example, the first row under $\%\Delta\bar{C}_{D,0}$ ($x^* = 0$) shows the percent difference between $\bar{C}_{D,fleet}$ from the axis-aligned simulation at $(x^*, y^*) = (-1.17, 0.3)$ and $\bar{C}_{D,0}$ from the stationary case at $(x^*, y^*) = (-1.17, 0.0)$.

Table 5.3 highlights the effects of the fleet arrangement on drag compared to what an ellipse experiences in a lone pair. The drag was larger in nearly every axis-aligned simulation. The largest differences between $\bar{C}_{D,fleet}$ and $\bar{C}_D$ from the stationary simulations occurred to Ellipse 1 at $y^* = 0.3$. During the stationary simulations at $(x^*, y^*) = (-1.17, 0.0)$, Ellipse 1 was located in the drafting region and experienced a drag benefit of 64.8% ($\bar{C}_{D,1} = 0.041$) compared to an isolated ellipse moving at the same speed. During the axis-aligned simulations, the drag coefficient was $\bar{C}_{D,fleet} = 0.495$, an increase of more than two orders of magnitude (1107%) compared to the stationary simulation value. This increase occurred because in the fleet arrangement, more ellipses occupied the same amount of space, which served to constrain the path of the flow. A more constrained path meant that the flow had to move faster between the ellipses to conserve mass, creating a larger pressure gradient and increasing drag (see Figure 5-3. There was one configuration where the drag benefit appeared to improve

compared to the stationary case: $(x^*, y^*) = (-1.17, 0.6)$. In this configuration, $\bar{C}_{D,fleet}$ was 0.072, which was a 44.6% improvement upon $\bar{C}_{D,0}$ from $(x^*, y^*) = (0.00, 0.6)$, a 50.3 % improvement upon $\bar{C}_{D,0}$ from $(x^*, y^*) = (0.00, 0.6)$, and a 29.4% improvement upon $\bar{C}_{D,0}$ from $(x^*, y^*) = (-1.17, 0.0)$. This improvement was aided by the fact that the fleet was not as densely occupied at $y^* = 0.6$ compared to $y^* = 0.3$, and the stationary simulation values were all drag increases.

Table 5.3: Comparison of axis-aligned, periodic array $\bar{C}_D$ results to those of a similar arrangement from the stationary case.

(x^*, y^*)	$\bar{C}_{D,fleet}$	$\%\Delta\bar{C}_{D,0}$ $(x^* = 0)$	$\%\Delta\bar{C}_{D,1}$ $(x^* = 0)$	$\%\Delta\bar{C}_{D,0}$ (tandem)	$\%\Delta\bar{C}_{D,1}$ (tandem)
$(-1.17, 0.3)$	0.495	+281	+241	+385	+1107
$(-1.17, 0.6)$	0.072	−44.6	−50.3	−29.4	+75.6
$(-1.50, 0.3)$	0.770	+492	+431	+620	+1067
$(-1.50, 0.6)$	0.203	+46	+56	+89.7	+208

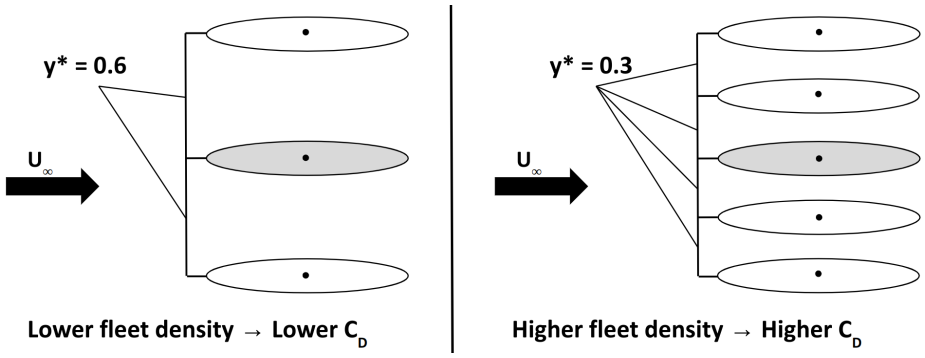

Figure 5-3: Effect of fleet density on drag coefficient observed in the periodic array simulations

A comparison between the results of the staggered simulations and their corresponding stationary case configurations is provided in Table 5.4. The $\bar{C}_{D,fleet}$ experienced by the ellipses in the infinite fleet was higher for all of the staggered simulations, except for at $(x^*, y^*) = (-1.17, 0.6)$ where there was no change for Ellipse 0. As with the axis-aligned simulations, the largest increases occurred when the lateral separation was smaller ($y^* = 0.3$). The maximum increase occurred at $(x^*, y^*) = (-1.50, 0.3)$, where $\bar{C}_{D,fleet}$ was 145% higher than in the stationary simulations. As in the axis-aligned simulations, the smaller x^*-value of -1.17 appeared to be

more beneficial to fleet drag compared to $x^* = -1.50$, as seen by the smaller $\%\Delta\bar{C}_D$ at $(x^*, y^*) = (-1.17, 0.3)$ compared to at $(x^*, y^*) = (-1.50, 0.3)$. An important difference between the axis-aligned and staggered configurations was that in the staggered configurations, there was an "empty space" where an ellipse had been present in the axis-aligned simulation. This meant that the fleet of ellipses in the staggered simulations was not as dense. Therefore, due to the tendency of higher fleet density to increase $\bar{C}_D$ as noted previously, the drag coefficients in the axis-aligned simulations tended to be higher.

Table 5.4: Comparison of staggered, periodic array $\bar{C}_D$ results to those of a similar arrangement using a single, free-space boundary domain (stationary case).

(x^*, y^*)	$\bar{C}_{D,fleet}$	Ellipse	$\%\Delta\bar{C}_D$
$(-1.17, 0.3)$	0.225	0	+97.4
		1	+143
$(-1.17, 0.6)$	0.116	0	−0.00
		1	+12.1
$(-1.50, 0.3)$	0.249	0	+126
		1	+145
$(-1.50, 0.6)$	0.122	0	+6.27
		1	+13.7

5.5 Takeaways

The results of the periodic array simulations showed that placing ellipses in an evenly spaced, infinitely repeating arrangement generally caused their drag coefficients to increase compared to the stationary case. When the ellipses were axis-aligned, an interplay between side-by-side and tandem configuration effects was observed. A smaller lateral offset (y^*) served to increase the drag, due to the higher fleet density constraining the area through which flow could travel between them. A smaller longitudinal offset (x^*) served to decrease the drag due to the advantages of drafting that were identified in the stationary case simulations. The lift and moment interactions remained near zero due to the symmetry of vertical spacing between neighboring ellipses. The staggered simulations were compared to stationary case results in the

low-interaction region, and similar trends to the axis-aligned arrangement were observed in terms of x^* and y^* effects. The capability of the Cubism-IIM2D software to efficiently implement periodic boundary conditions makes this the first known model of an infinitely sized UUV fleet.

THIS PAGE INTENTIONALLY LEFT BLANK

Chapter 6

Overtaking Case

The overtaking case, in which one ellipse moves past the other at a constant relative velocity, occurs during refueling and docking maneuvers that are performed during UUV operations. Overtaking case simulations were performed under similar conditions to those used in the stationary simulations of Chapter 3, with the addition of relative motion between the ellipses. The goal of these simulations was to determine the effects of lateral separation and relative longitudinal velocity on the forces experienced by each ellipse. An extension of the overtaking case – having one ellipse completely stationary – was also simulated to discern the effects of transient motion independent of an inflow.

6.1 Introducing Relative Motion

Separate simulations for the overtaking case were necessary because the results of the stationary case could not simply be compiled together to accurately represent the overtaking case. The introduction of relative velocity meant that as the relative positions between the ellipses changed, so did their interactions between each other and with the external flow.

Another consequence of introducing relative velocity was that equivalence between the relative positions of ellipses (i.e., symmetry) could not be assumed. This meant that the results could not be reflected across the $x^* = 0$ axis, such as they were in

the stationary simulations (see Figure 3-2). Consequently, the overtaking simulations were run for the full range of $-1.5 \leq x^* \leq 1.5$, instead of computing results for just one quadrant and translating them to other quadrants.

Introducing relative motion also caused the faster ellipse to move with respect to the frame of reference, which was taken to move with the slower ellipse. Because the simulator only recorded the initial position of the ellipses and the simulation time, the x-position of the faster ellipse was back-calculated using the kinematic relation

$$x(t) = x_0 + u_1 t,$$

where $x(t)$ is the position as a function of time, x_0 is the initial position, and u_1 is the velocity of the faster ellipse within the reference frame. Section 6.2 provides further information on the arrangement of ellipses within the test domain.

6.2 Simulation Setup

The parameters of the overtaking simulations were largely the same as those used in the stationary case, with the main difference being the introduction of relative motion in the positive x-direction (right to left) for Ellipse 1. As in the stationary case, Ellipse 0 moved with an absolute velocity of $U_0 = |U_\infty|$ while having zero velocity within the reference frame ($u_0 = 0$). Ellipse 1 moved with an absolute velocity of

$$U_1 = u_1 + |U_\infty|,$$

where u_1 is the velocity of the faster ellipse within the reference frame (i.e., with respect to the slower ellipse), and U_∞ is the inflow from left to right (as in the stationary case). U_∞ was maintained such that $Re = U_\infty L/\nu = 1500$. The relative velocity was taken as

$$u_{rel} = \frac{U_1}{U_0}.$$

Because the ellipses moved at different velocities, they had different Reynolds

numbers. Equation 6.1 shows the calculation of Reynolds number for each ellipse in the overtaking case:

$$\begin{aligned} Re_0 &= \frac{U_0 L}{\nu} = \frac{U_\infty L}{\nu} \\ Re_1 &= \frac{U_1 L}{\nu} \end{aligned} \tag{6.1}$$

The difference in ellipse velocities also made the calculation of force and moment coefficients slightly different from the stationary simulations. Equation 6.2 shows the calculation of C_D, C_L, and C_M for both ellipses in the overtaking case:

$$\begin{aligned} C_{D,0} &= \frac{2F_x}{\rho U_0^2 L} & C_{D,1} &= \frac{2F_x}{\rho U_1^2 L} \\ C_{L,0} &= \frac{2F_y}{\rho U_0^2 L} & C_{L,1} &= \frac{2F_y}{\rho U_1^2 L} \\ C_{M,0} &= \frac{2M_z}{\rho U_0^2 L^2} & C_{M,1} &= \frac{2M_z}{\rho U_1^2 L^2} \end{aligned} \tag{6.2}$$

The overtaking simulations were initiated by allowing the flow to develop for a predetermined amount of time, so that the wakes reached a symmetric arrangement (as in the stationary simulations). A delay of $t^* = 16.7$ was introduced at the start of each simulation for this purpose. During the delay, the ellipses remained fixed in their initial relative positions. After the delay, Ellipse 1 began an initial "ramp-up" velocity. The ramp-up velocity was used so that Ellipse 1 would reach the desired relative velocity by the time it crossed the starting position of $x^* = -1.50$, while avoiding an abrupt start that might interrupt the flow field and/or inhibit data accuracy. The velocity of the ellipse during the ramp-up stage followed a cosine-bump function (equation 6.3) to limit the time and space needed for the ramp-up:

$$u_{ramp}(t^*) = \frac{1}{2}\left(1 - \cos\left(\frac{\pi(t^* - t_0^*)}{T^*}\right)\right) u_{rel}. \tag{6.3}$$

The function $u_{ramp}(t^*)$ is the ramp-up velocity of Ellipse 1 with respect to non-dimensional time; t_0^* is the start time of the ramp-up stage; t^* is the time elapsed during the ramp-up stage; T^* is the total duration of the ramp-up stage (a pre-set

value); and u_{rel} is the desired relative velocity for the overtaking simulation (also a pre-set value). In addition to equation 6.3, the distance covered during the ramp-up stage was determined so that the ellipse would be positioned exactly at the start of the formal "overtaking region" ($x^* = -1.5$). The total ramp-up distance, d_{ramp}, was found by integrating the ramp-up velocity function with respect to time, as shown in equation 6.4:

$$d_{ramp} = \int_{t_0^*}^{t_0^*+T^*} u_{ramp}(t^*)\, dt^* = u_{rel}\frac{T^*}{2}. \tag{6.4}$$

Additionally, the position at any point in the ramp-up stage, $d_{ramp}(t^*)$ could be calculated using equation 6.5:

$$d_{ramp}(t^*) = \int_{t_0^*}^{t_0^*+t^*} u_{ramp}(t^*)\, dt^* = \frac{1}{2\pi}T^* u_{rel}\left(\frac{\pi t^*}{T^*} - \sin\frac{\pi t^*}{T^*}\right). \tag{6.5}$$

Figure 6-1 shows the values of $x - x_0$ (the position with respect to the starting point) and u_{rel} as a function of non-dimensional time. The dots indicate the start and end of the ramp-up stage. Prior to $t^* = 16.7$, there was no relative velocity introduced (i.e., $u_{rel} = 0$). At the end of the velocity ramp-up period from $16.7 \leq t^* \leq 19.2$, the relative velocity reached the prescribed value of $u_{rel} = 1$ moving right to left through the domain.

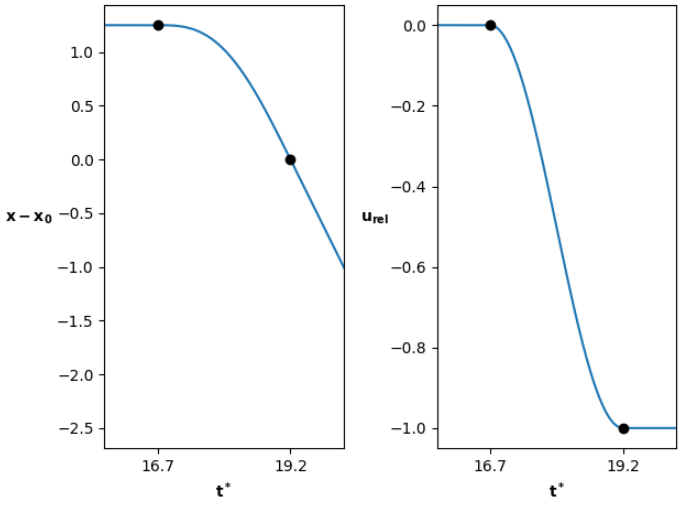

Figure 6-1: Plot of the ramp-up function for the overtaking ellipse with respect to time. Dots indicate the start and end of the ramp-up period.

At the end of the ramp-up stage, Ellipse 1 was positioned at exactly $x^* = -1.5$ and moved with the desired relative velocity of u_{rel}. Force data was gathered while Ellipse 1 traveled across the range $-1.5 \leq x^* \leq 1.5$ (i.e., the overtaking region). Figure 6-2 shows the setup of the overtaking simulations, including the velocity ramp-up and overtaking regions. The domain size was set to $9L$ behind the stern of the faster ellipse, measured from the start of the overtaking region ($x^* = -1.5$). The value of $9L$ was used based on the domain size determined for two ellipses in Section 2.5.

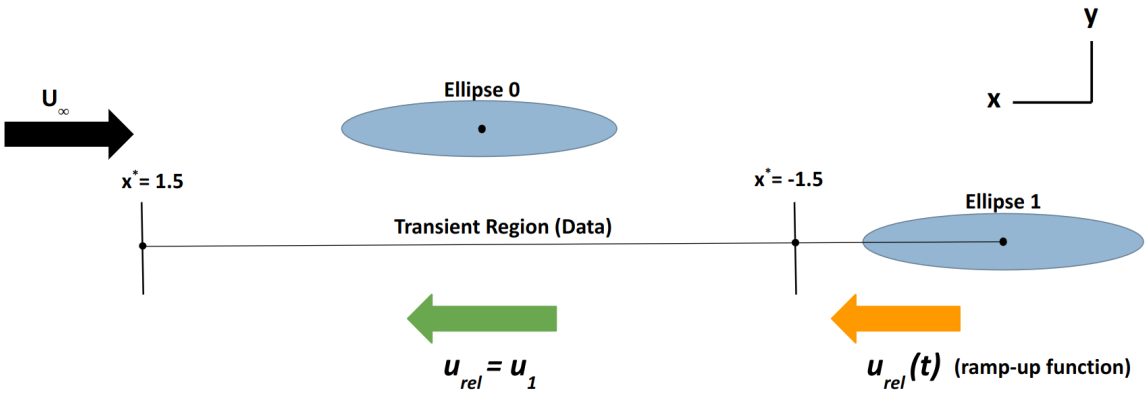

Figure 6-2: Setup of the overtaking simulations, including the velocity ramp-up region and the overtaking region

6.2.1 $\bar{C}_D$ of an Isolated Ellipse at Various Speeds

A series of simulations were performed to determine the time-averaged drag coefficient of an isolated ellipse in a free stream at different velocities. These values were used to normalize the drag coefficient for the faster ellipse at different values of u_{rel}, so that the net change in $\bar{C}_D$ due to ellipse interactions could be more accurately determined. In a similar manner to the stationary simulations, the wake was allowed to reach a symmetric, steady state before a time-averaged drag coefficient $\bar{C}_{D,iso}$ was calculated. Figure 6.1 shows the results of $\bar{C}_{D,iso}$ at $Re = 1500$, 1875, 2250, 2625, and 3000. These Reynolds numbers corresponded to the values of U that occurred in the overtaking simulations: $Re = 1500$ corresponded to Ellipse 0 in the free stream, and $Re = 1875$, 2250, 2625, and 3000 corresponded to Ellipse 1 with an added relative velocity ($u_{rel} =$ 0.25, 0.50, 0.75, and 1.00, respectively). The numerical results are shown in Table

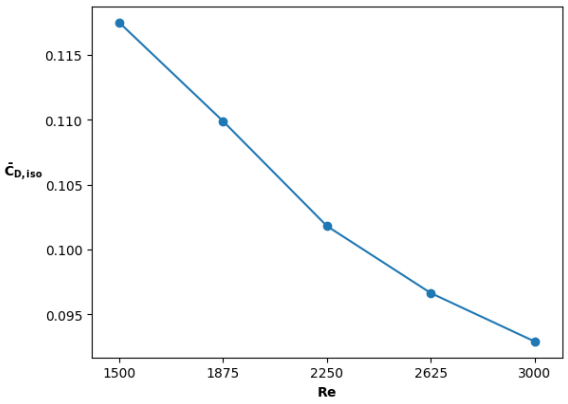

(a) Plot of $\bar{C}_{D,iso}$ at different Re

Re	$\bar{C}_{D,iso}$
1500	0.1175
1875	0.1099
2250	0.1018
2625	0.0966
3000	0.0929

(b) Values of $\bar{C}_{D,iso}$ at different Re

Figure 6-3 & Table 6.1: Time-averaged drag coefficients of an isolated ellipse in a free stream at different Reynolds numbers

6.1. The fact that $\bar{C}_{D,iso}$ decreased with increasing Reynolds number was an expected result based on the known negative relationship between C_D and Re in this range. The isolated ellipse simulations were not analyzed for C_L and C_M, as their mean values are zero for an isolated ellipse in a free stream.

6.3 Results of Overtaking Simulations

Figure 6-4 shows the progression of an overtaking simulation in which $(y^*, u_{rel}) = (0.3, 1.00)$, with images taken one time unit apart. Image a) shows the ellipse after the $t^* = 16.7$ delay to reach steady-state for the ellipse wakes. Ellipse 1 experiences a ramp-up in velocity between images a) and d), until it reaches a longitudinal separation of $x^* = -1.5$ from Ellipse 0. Between images e) and g), Ellipse 1 overtakes Ellipse 0 at a constant relative velocity of $u_{rel} = 1.00$.

The overtaking simulations were performed for lateral separations $y^* = 0.3$, 0.4, 0.5, and 0.6 at relative velocities of $u_{rel} = 0.25$, 0.50, 0.75, and 1.00 for Ellipse 1. Figure 6-5 shows the results for a single relative velocity, $u_{rel} = 1.00$, at all of the different lateral separations ($y^* = 0.3$, 0.4, 0.5, and 0.6). This plot illustrates the effect of increasing lateral separation on ΔC_D, C_L, and C_M of the two ellipses. ΔC_D was calculated as $\Delta C_D = C_D - \bar{C}_{D,iso}$, using the value of $\bar{C}_{D,iso}$ in Table 6.1

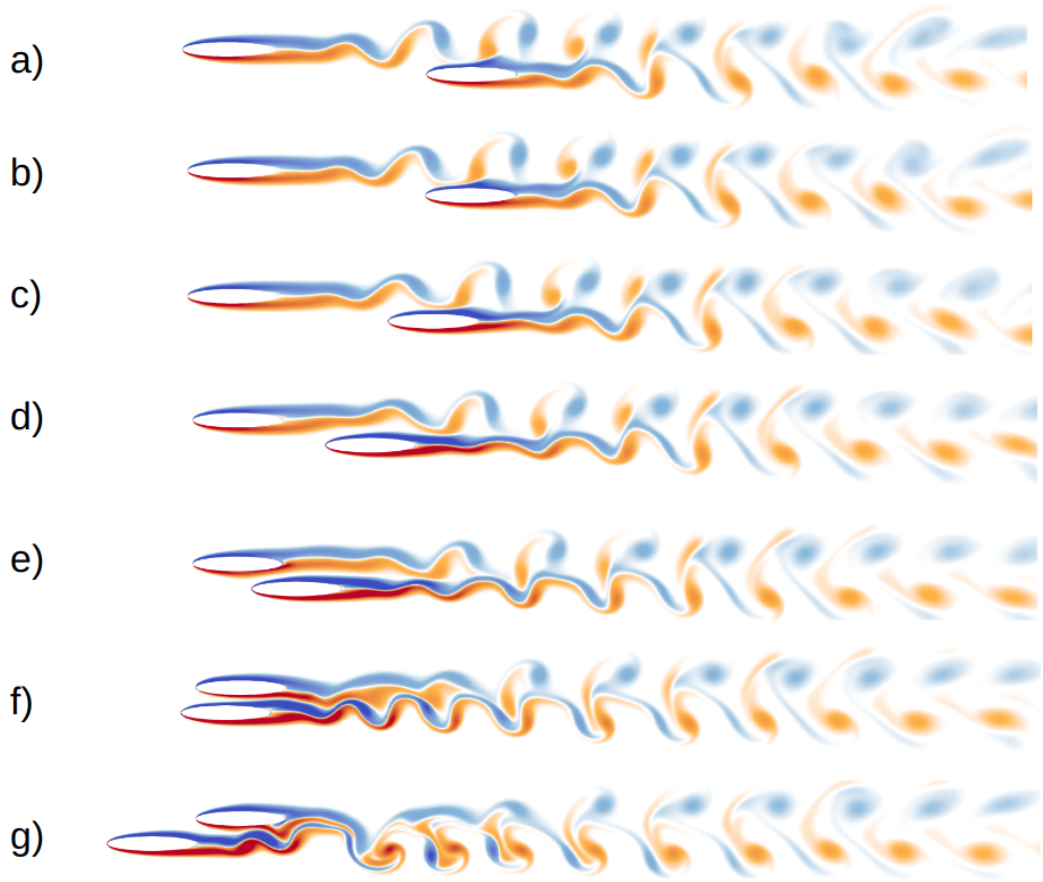

Figure 6-4: Images from an overtaking simulation where $y^* = 0.3$ and $u_{rel} = 1.00$, taken one time unit apart each. Parts a) through d) show the ramp-up in velocity, and parts e) through g) show the overtaking maneuver.

that corresponded to the absolute velocity of the ellipse. The trend observed for all simulated u_{rel} was that increasing the lateral separation decreased the magnitude of the force and moment coefficients of both ellipses. $\Delta C_{D,0}$ was positive for $x^* < 0$ and negative for $x^* > 0$, with peaks occurring at or near $x^* = \pm 0.5$. $\Delta C_{D,1}$ transitioned from negative to positive over the same period. The lift was repulsive for almost the entire overtaking period, with $C_{L,0}$ peaking at $x^* = -0.5$ and $C_{L,1}$ peaking at $x^* = 0$. The increase in $C_{L,0}$ toward the end of the simulation likely occurred due to trailing-wake vortex effects produced by the faster ellipse that pushed the slower ellipse outward. The moment was bow-out for Ellipse 0 and bow-in for Ellipse 1 for $x^* \leq -0.67$, after which the bow of $C_{M,1}$ was pushed outward. $C_{M,0}$ became bow-out

after $x^* > 0$.

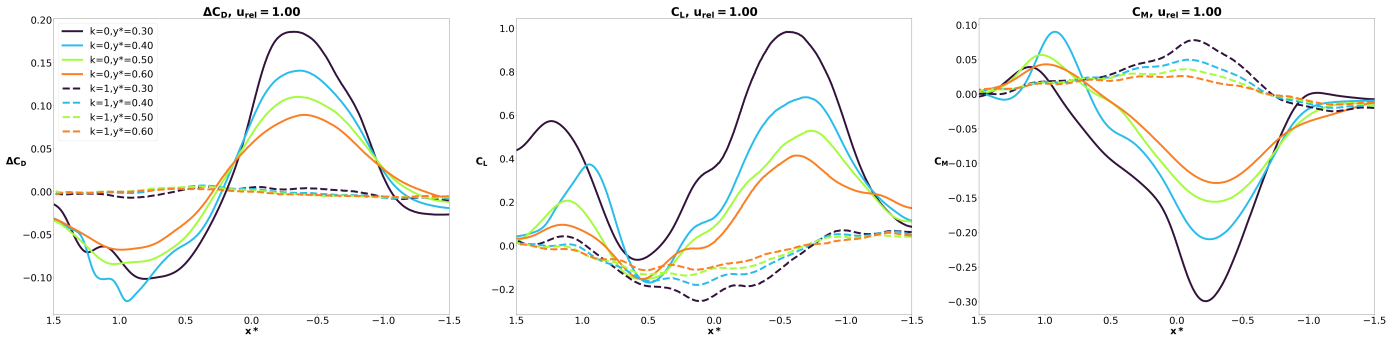

Figure 6-5: Results of $u_{rel} = 1.00$ at $y^* = 0.3$, 0.4, 0.5, and 0.6 for the overtaking simulations

Figure 6-6 shows the average force and moment values and how they changed with respect to y^* for the relative velocity $u_{rel} = 1.00$. The plots reinforce the negative correlation between lateral separation and the magnitude of forces and moments on the ellipses. They further show that the difference between lift and moment values of Ellipse 0 and Ellipse 1 became smaller at greater lateral separations. For all simulations, the slower ellipse (Ellipse 0) experienced a lower drag force and moment but a slightly higher lift force compared to the faster ellipse (Ellipse 1). The drag and lift of the ellipses varied similarly between different y^*, while the moment of the faster ellipse responded more to changes in y^* compared to the slower ellipse. In the plot of drag force, the dotted lines indicate the drag on an isolated ellipse moving at each corresponding velocity. The similarity between the dotted and solid lines shows that the drag on an ellipse was affected very little by the presence of the other ellipse when both were moving.

Figure 6-7 shows the results for one lateral separation, $y^* = 0.3$, at all of the different relative velocities that were simulated ($u_{rel} = 0.00$, 0.25, 0.50, 0.75, and 1.00). The plot represents data from the same simulation case but highlights the effect of increasing relative velocity on ΔC_D, C_L, and C_M. It was found that increasing u_{rel} resulted in an increase of all coefficients for the slower ellipse. The higher flow interference from the faster ellipse increased the values of $F_{x,0}$, $F_{y,0}$, and $M_{z,0}$ experienced by the slower ellipse. On the other hand, a higher u_{rel} resulted in a decrease of $\Delta C_{D,1}$,

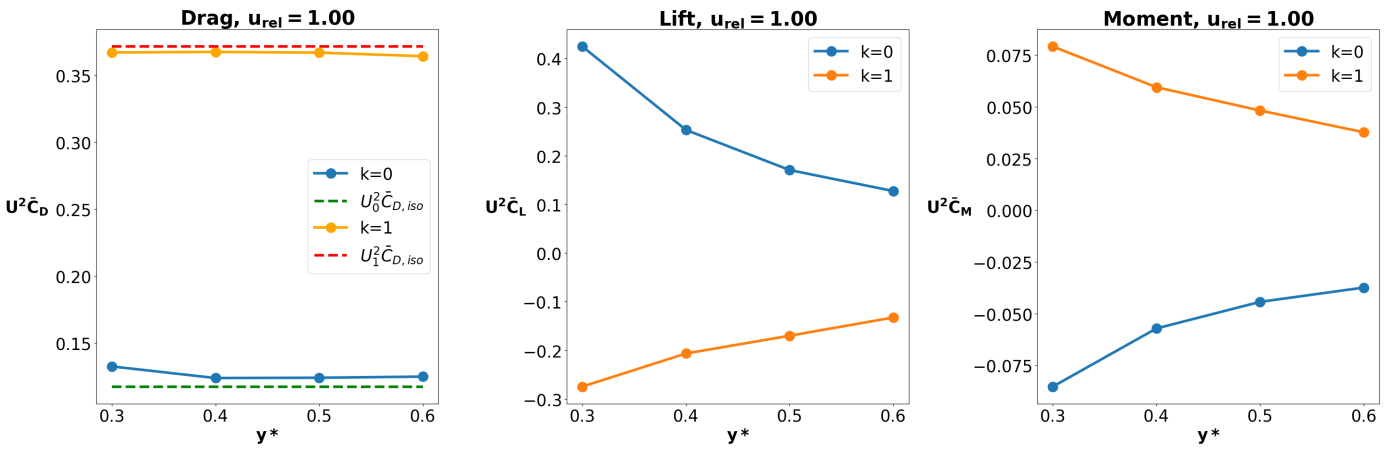

Figure 6-6: Change of average forces and moments with respect to y^* during the overtaking simulation at $u_{rel} = 1.00$

$C_{L,1}$, and $C_{M,1}$ for the faster ellipse, despite an increase in $F_{x,1}$, $F_{y,1}$, and $M_{z,1}$ on the faster ellipse at higher speeds.

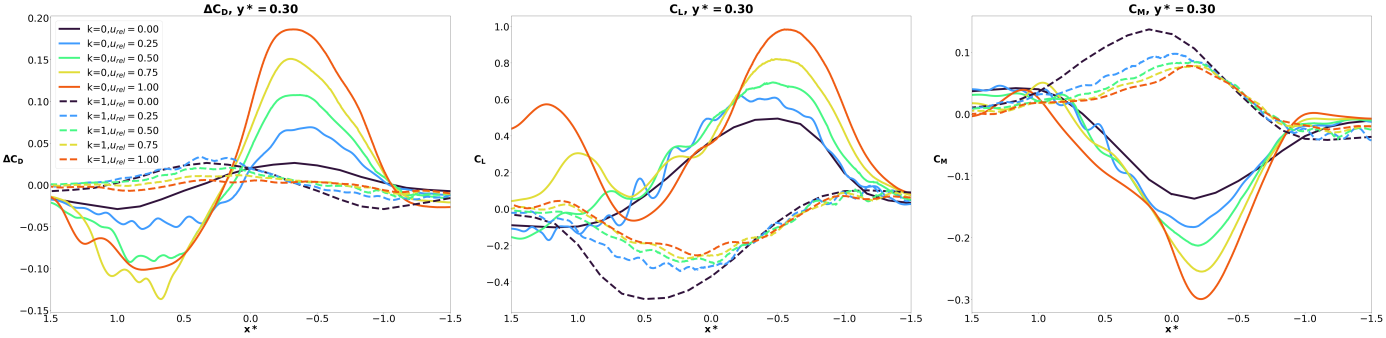

Figure 6-7: Results of $y^* = 0.3$ at $u_{rel} = 0.25$, 0.50, 0.75, and 1.00 for the overtaking simulations, as well as $u_{rel} = 0.00$ from the stationary case

Using the results from Figure 6-7, Figure 6-8 shows the average force and moment values and how they changed with respect to u_{rel} at the lateral separation $y^* = 0.3$. The plots show that increasing u_{rel} served to increase the average drag, lift, and moment of the slower ellipse. For the slower ellipse, increasing u_{rel} resulted in an increase of the average drag and a decrease of the average lift. The moment of the slower ellipse did not change significantly with respect to u_{rel}. A divergence in the values of drag, lift, and moment with increasing u_{rel} is also apparent from the plots. The dotted lines once again show that the drag was affected very little by ellipse interactions when both ellipses were moving.

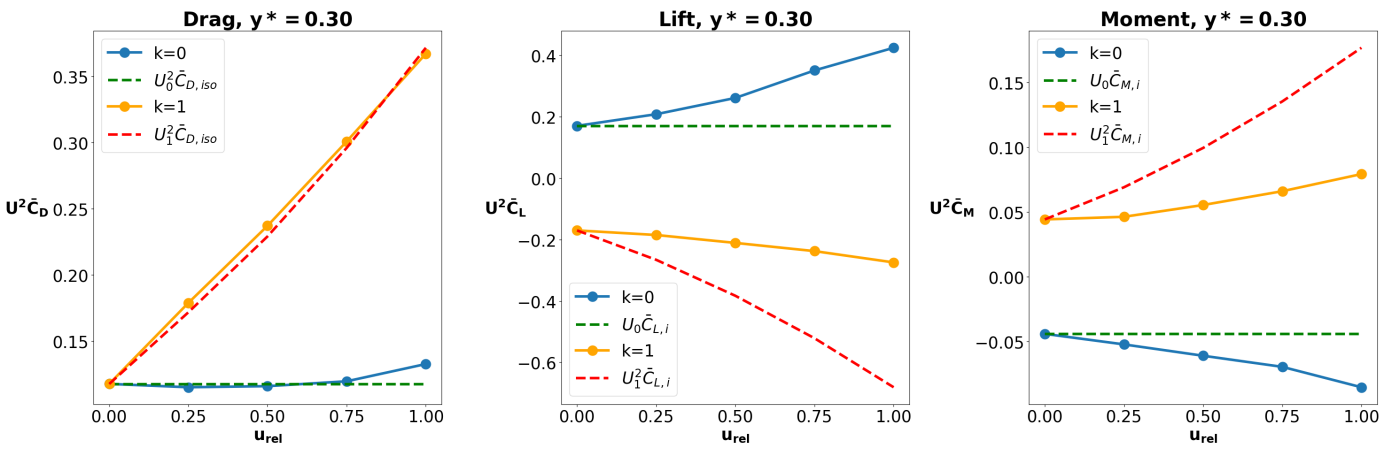

Figure 6-8: Change of average forces and moments with respect to u_{rel} during the overtaking simulations at $y^* = 0.3$. Results of $u_{rel} = 0.00$ from the stationary simulations are also included.

Full plots that include all 16 overtaking cases, both for constant u_{rel} and for constant y^*, are included in Appendix B.

6.4 Overtaking a Stationary Body

The overtaking simulations above used a fixed value of $Re_0 = 1500$ and varied Re_1 from 1500 to 3000. The simulations in this section investigated what would happen if the same values of $1500 \leq Re_1 \leq 3000$ were used, but Re_0 was set to zero. To accomplish this, a separate set of simulations were performed with the inflow absent, so that Ellipse 1 moved past a completely stationary Ellipse 0 in a free-space boundary domain. To distinguish from the overtaking simulations previously described, these simulations were referred to as the "overtaking-stationary" simulations. The domain inflow velocity was set to $U_\infty = 0$ so that Ellipse 0 was kept stationary ($Re_0 = 0$). Ellipse 1 moved at Reynolds numbers of $Re_1 = \{1500, 1875, 2250, 2625, 3000\}$. Although the relative velocity was undefined due to the fact that $U_\infty = U_0 = 0$, u_{rel} was "defined" for the overtaking-stationary case to be normalized by u_0 from the original overtaking case (i.e., $Re_0 = 1500$) to enable comparison between cases. All other parameters from the overtaking simulations remained the same, except that the delay of $t^* = 16.7$ was no longer used due to the lack of an inflow.

Figure 6-9 shows the results of the overtaking-stationary simulations at $u_{rel} = 1.00$, for all of the lateral separations ($y^* = 0.3$, 0.4, 0.5, and 0.6). Ellipse 1 saw an increase in ΔC_D throughout the maneuver. C_L was repulsive for $x^* < 0$, reaching a positive peak for Ellipse 0 just before $x^* = -0.5$ and a negative peak for Ellipse 1 (with greater magnitude) shortly thereafter. For $x^* > 0$, C_L was negative for both ellipses, with $|C_{L,0}| > |C_{L,1}|$. $C_{M,1}$ was directed bow-in for the entire simulation and peaked at $x^* = -0.33$.

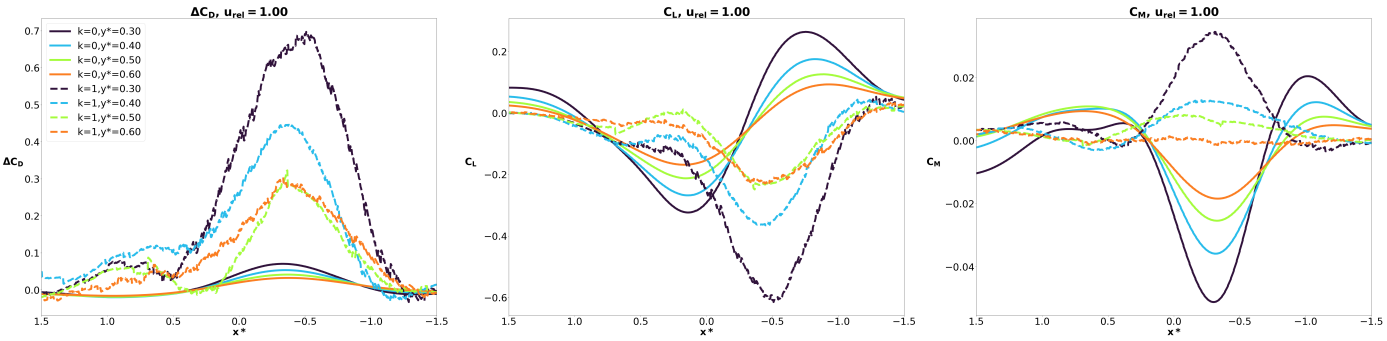

Figure 6-9: Results of $u_{rel} = 1.00$ at $y^* = 0.3$, 0.4, 0.5, and 0.6 for the overtaking-stationary simulations

Figure 6-10 shows the average forces and moments and how they changed with respect to y^* when $u_{rel} = 1.00$. The forces and moments of both ellipses generally decreased in magnitude with increasing y^*. For all simulations, the forces and moments on the faster ellipse were greater than on the slower ellipse and responded more to changes in lateral separation. It should be noted that the coefficients of Ellipse 1 appear to level off between $y^* = 0.5$ and $y^* = 0.6$, while the coefficients of Ellipse 0 continue to decrease. This was only observed at the lowest value of $u_{rel} = 1.00$; at higher u_{rel}, the coefficients of Ellipse 1 continued to decrease. The dotted line in the drag force plot shows the drag on an isolated ellipse at each corresponding velocity. The large difference between the solid $k = 1$ line and the dotted $U_1^2 \bar{C}_{D,iso}$ line shows that the drag of the overtaking ellipse was affected significantly when the other ellipse was stationary.

Features of the overtaking-stationary simulations appeared at higher relative velocities that were not observed in Figure 6-9 (constant $u_{rel} = 1.00$). Figure 6-11

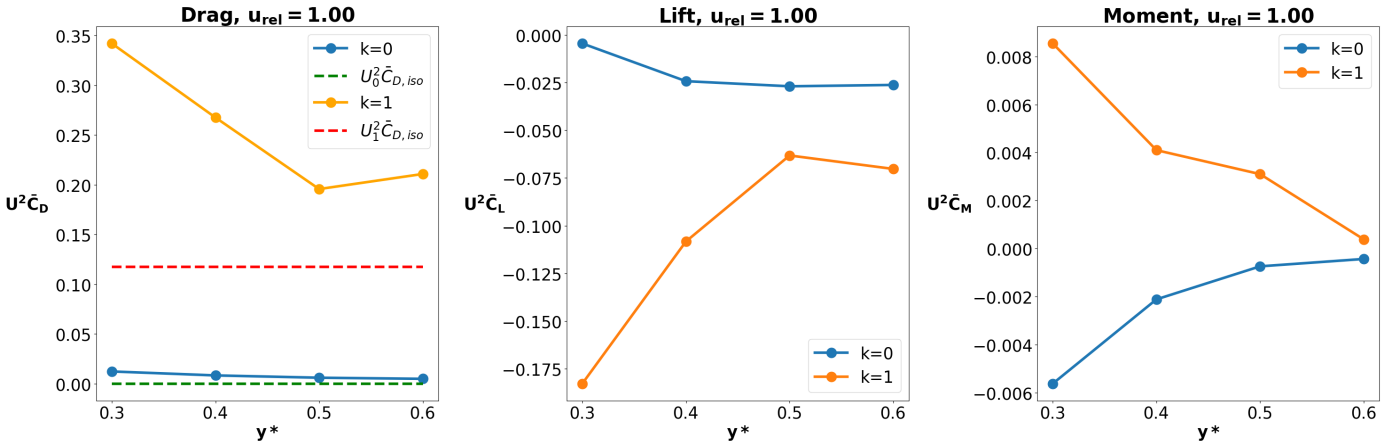

Figure 6-10: Average forces and moments with respect to y^* during the overtaking-stationary simulations at $u_{rel} = 1.00$

shows the results for a single lateral separation, $y^* = 0.3$, at all of the different relative velocities that were simulated ($u_{rel} = 1.00$, 1.25, 1.50, 1.75, and 2.00). The coefficients of Ellipse 1 were generally greater in magnitude than those of Ellipse 0, which was also observed in Figure 6-9. A difference was that at relative velocities of $u_{rel} \geq 1.25$, $\Delta C_{D,1}$ transitioned from positive to negative at $x^* = 0$. The positive and negative peaks in $\Delta C_{D,1}$ occurred at $x^* = -0.5$ and $x^* = 0.5$, respectively. C_L was repulsive ($C_{L,0} > 0$ and $C_{L,1} < 0$) for $x^* < 0$, peaking first for Ellipse 0 just before $x^* = -0.5$ and for Ellipse 1 shortly thereafter. For $x^* > 0$, C_L was attractive ($C_{L,0} < 0$ and $C_{L,1} > 0$), with $|C_{L,1}| > |C_{L,0}|$. A full transition toward attractive lift was not observed at $u_{rel} = 1.00$, since $C_{L,1}$ remained negative for $x^* > 0$. $C_{M,1}$ went from bow-in to bow-out, with the inflection point occurring at $x^* = 0$.

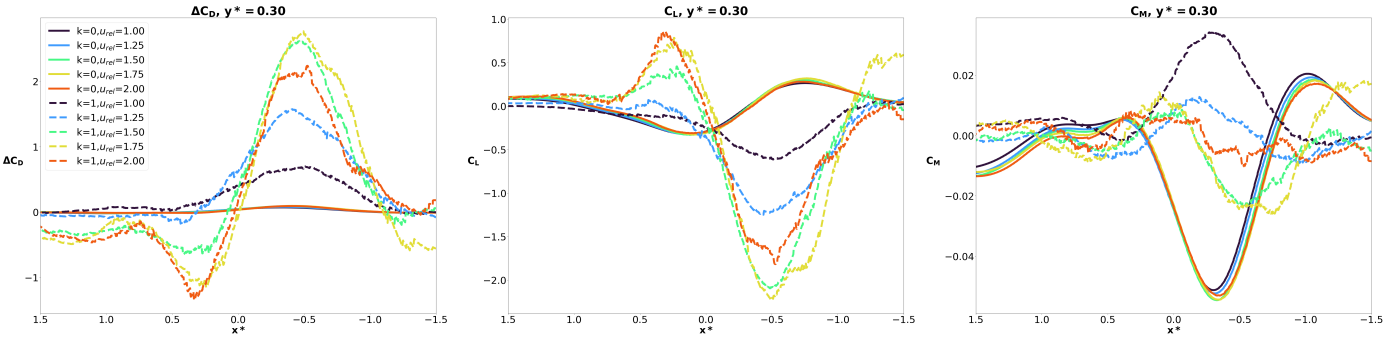

Figure 6-11: Results of $y^* = 0.3$ at $u_{rel} = 1.00$, 1.25, 1.50, 1.75, and 2.00 for the overtaking-stationary simulations

Figure 6-12 shows the average forces and moments and how they changed with respect to u_{rel} at the lateral separation $y^* = 0.3$. The forces and moments of Ellipse 0 changed little compared to those of Ellipse 1 and were smaller in magnitude. The drag and lift of Ellipse 1 increased alongside relative velocity, while the moment varied between an average of 0.009 at $u_{rel} = 1.00$ and -0.009 at $u_{rel} = 2.00$. The dotted line in the drag force plot once again shows that the presence of the stationary ellipse significantly affected the drag on the faster ellipse.

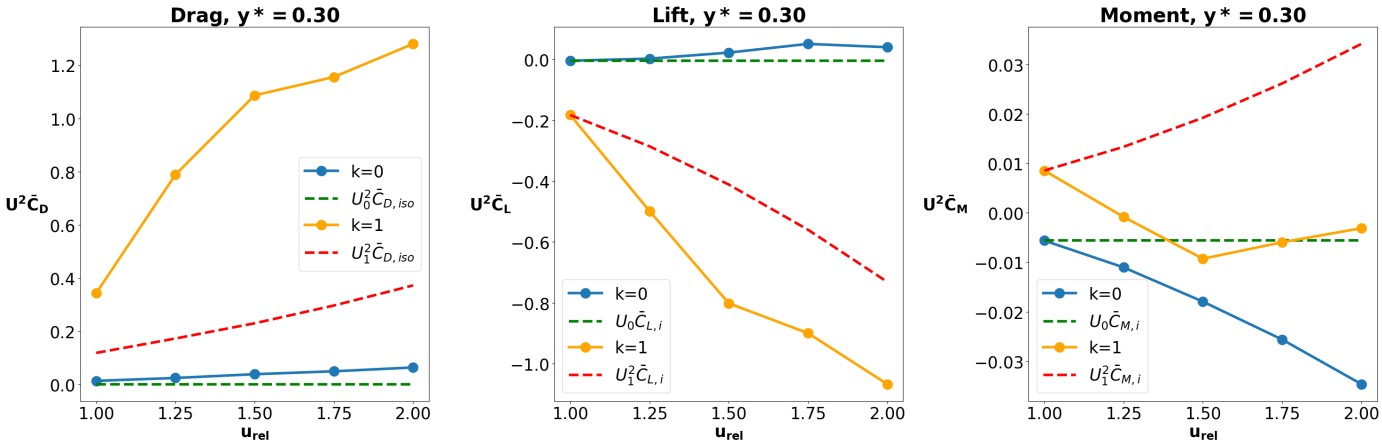

Figure 6-12: Average forces and moments with respect to u_{rel} during the overtaking-stationary simulations at $y^* = 0.3$

Full plots that include all 20 cases, both for constant u_{rel} and for constant y^*, are included in Appendix B.

Additional analysis of the results in this chapter, comparison to other studies of transient motion, and comparison between the stationary and overtaking cases are provided in Chapter 7.

THIS PAGE INTENTIONALLY LEFT BLANK

Chapter 7

Overtaking Case Analysis

This chapter continues the discussion of overtaking case simulations presented in Chapter 6 by analyzing the results of the overtaking and overtaking-stationary simulations; comparing the results to those of existing studies about transient motion; and examining the differences between the stationary and overtaking case results. An additional set of simulations were performed to observe the effect of domain width on lift interactions during an overtaking maneuver.

7.1 Overtaking Simulation Observations

The overtaking simulations (results in Section 6.3 and Appendix B) showed that the force and moment coefficients were typically greater in magnitude for the slower ellipse compared to the faster ellipse (i.e., $|\Delta C_{D,0}| > |\Delta C_{D,1}|$, $|C_{L,0}| > |C_{L,1}|$, and $|C_{M,0}| > |C_{M,1}|$). The force and moment coefficients on Ellipse 0 increased as Ellipse 1 passed with a larger relative velocity, whereas the associated coefficients on Ellipse 1 itself decreased. Increasing the relative velocity did not change the general behavior of the drag, lift, and moment, but it did increase the magnitude of the coefficients. An analysis of the drag, lift, and yaw moment interactions is provided below:

Mean Drag Effects The mean drag of the slower ellipse was roughly unaffected by the overtaking maneuver, except at $(y^*, u_{rel}) = (0.3, 1.00)$ where the mean

drag coefficient was 12.8% higher ($\Delta\bar{C}_{D,0} = 0.015$) than an isolated ellipse at $Re = 1500$. The mean drag of the faster ellipse was also largely unaffected by the maneuver. The highest $\Delta\bar{C}_{D,1}$ across an entire simulation was 0.005 at $(y^*, u_{rel}) = (0.3, 0.25)$, a 4.3% increase from an isolated ellipse at the equivalent $Re = 1875$. Figure 6-8 shows that changes in average drag were almost entirely accounted for by changes in Re (similar to an isolated ellipse) rather than by ellipse interactions.

Transient Drag Effects The drag coefficient of the slower ellipse experienced very large variations and increased alongside u_{rel}, while the drag coefficient of the faster ellipse experienced very small variations and decreased at higher u_{rel}. In Figures 6-5 and 6-7, the scale of $\Delta C_{D,0}$ (~ 0.2) is approximately ten times greater than that of $\Delta C_{D,1}$ (~ 0.02). $\Delta C_{D,0}$ experienced two distinctive phases. The first phase occurred prior to $x^* = 0$, where the slower ellipse experienced a drag increase that was over 2.5 times greater than the isolated ellipse value ($\Delta C_{D,0} = 0.186$ at $u_{rel} = 1.00$ versus $\bar{C}_{D,iso} = 0.117$ at $Re = 1500$). The second phase occurred after $x^* = 0$, where the slower ellipse experienced a drag benefit greater than the isolated ellipse value ($\Delta C_{D,0} = -0.128$ at $u_{rel} = 1.00$ versus $\bar{C}_{D,iso} = 0.117$ at $Re = 1500$). Meanwhile, $\Delta C_{D,1}$ was generally opposite in sign to $\Delta C_{D,0}$. The faster ellipse received a slight drag benefit (up to 8.5% when $\Delta C_{D,0} = -0.010$ at $u_{rel} = 1.00$) as it trailed in the area of lower pressure behind the slower ellipse. After it passed the slower ellipse, the faster ellipse experienced a slight drag augment (up to 8.5% when $\Delta C_{D,0} = 0.010$ at $u_{rel} = 1.00$) while producing a large drag benefit for the slower ellipse. The slower ellipse benefited more from being downstream of the faster ellipse, because the faster ellipse caused a greater breakdown in the momentum of the incoming flow, creating more favorable conditions (lower shear stress and lower pressure) for the slower ellipse to follow.

Lift Effects C_L was repulsive for the entire passing maneuver. The lift coefficient of the slower ellipse experienced large variations and increased alongside u_{rel},

while the lift coefficient of the faster ellipse experienced small variations and decreased at higher u_{rel}. The highest $\bar{C}_{L,0}$ for an entire simulation was 0.425 at $(y^*, u_{rel}) = (0.3, 1.00)$ (2.5 times the value at $u_{rel} = 0$), and the highest-magnitude $\bar{C}_{L,1}$ for an entire simulation was -0.119 at $(y^*, u_{rel}) = (0.3, 0.25)$ (70% of the value at $u_{rel} = 0$). The larger lift force acting on the slower ellipse meant that it would be pushed away more than the faster ellipse. Examining Figure 6-8 shows that the lift of the faster ellipse did not increase as fast expected for an isolated body at higher Re; instead, the lift of the slower ellipse increased even though it continued to move at $U_0 = 1$ for all simulations.

Moment Effects C_M was mostly driven by the lift – due to its greater magnitude on account of the elongated shape of the ellipses – and the relative position of the bodies. The drag had little impact on the yaw moment because it was smaller in magnitude than the lift. Additionally, due to the aspect ratio of the ellipses, the vertical component of the traction acted on by the drag was smaller than the horizontal component acted on by the lift. The moments were out of phase because the faster body traveled into the interactions bow-first, whereas the slower body interacted with the faster body stern-first. The largest instantaneous C_M for the ellipses occurred slightly before $x^* = 0$, with a value of -0.299 for the slower ellipse at $(y^*, u_{rel}) = (0.3, 1.00)$ and 0.098 for the faster ellipse at $(y^*, u_{rel}) = (0.3, 0.25)$.

In general, the slower ellipse experienced interaction effects more than the faster ellipse. The drag, lift, and moment coefficients of the slower ellipse were much larger, experienced greater variation with changing u_{rel}, and increased in magnitude alongside u_{rel}. Although the drag, lift, and moment of the faster ellipse increased in magnitude with u_{rel}, these increases were at or below the expected levels for an isolated ellipse at higher Reynolds numbers.

Section 7.1.1 divides the results of the overtaking simulations into regions based on the characteristics of ellipse interactions.

7.1.1 Regions of Interaction

The longitudinal positions of the overtaking case were divided into five distinct regions based on the values of the force and moment coefficients during the overtaking maneuver. The regions were observed to occur irrespective of lateral separation y^*, although the magnitude of the force and moment coefficients decreased as the ellipses were spaced further apart. Figure 7-1 shows the regions of interaction for the overtaking simulations.

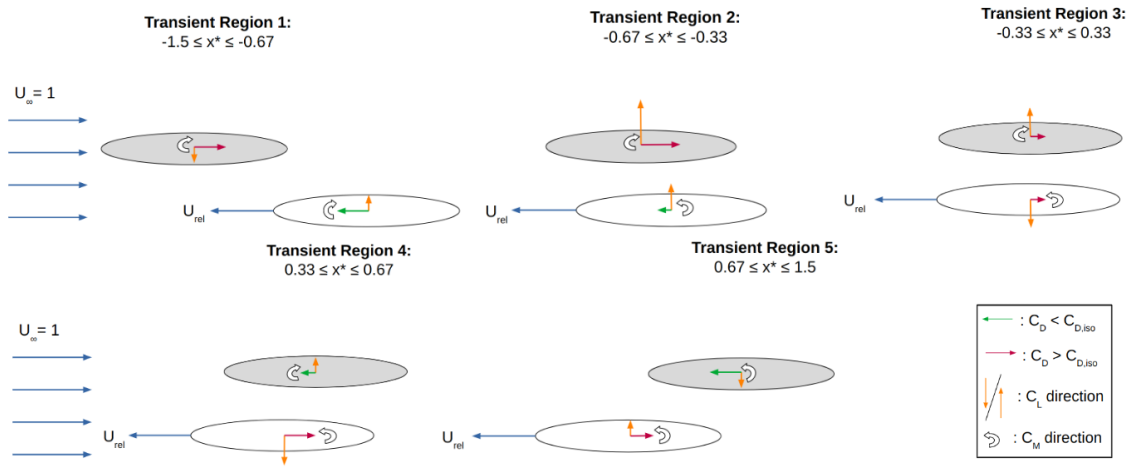

Figure 7-1: Regions of interaction for the overtaking simulations

The first interaction region occurred between $-1.50 \leq x^* \leq -0.67$. The faster ellipse experienced a slight decrease in C_D, while the slower ellipse experienced a slight increase. This "pull" effect was similar to the one observed in the echelon region during the stationary simulations. The C_L values showed a slight attraction between the ellipses due to a low-pressure region that pulled the bow of the faster ellipse and the stern of the slower ellipse toward each other. This effect also manifested in the moment of the two ellipses, which were both negative (counter-clockwise).

The second region of interaction occurred between $-0.67 \leq x^* \leq -0.33$. The drag benefit experienced by the faster ellipse in the first region became smaller as its beam passed the stern of the slower ellipse, and the slower ellipse continued to see a net increase in C_D. The lift, which previously attracted the ellipses toward each other, shifted for the slower ellipse so that it was directed upward and away from the faster

ellipse, and the C_L for both ellipses was positive. The moment of the faster ellipse shifted direction from negative to positive, as its stern was pulled toward the stern of the slower ellipse.

The third region of interaction occurred between $-0.33 \leq x^* \leq 0.33$. There was a net C_D increase for both ellipses, similar to the parallel region in the stationary simulations. The C_L of the faster ellipse changed directions from positive to negative, so that there was a net repulsion between the ellipses. C_M remained in the same direction as region 2, but increased in magnitude and reached a maximum for both ellipses.

The fourth region of interaction occurred between $0.33 \leq x^* \leq 0.67$. The slower ellipse began to experience a decrease in C_D, while C_D further increased for the faster ellipse. C_L remained repulsive, but its magnitude decreased for both ellipses. C_M remained in the same direction as regions 2 and 3, but decreased in magnitude for both ellipses.

The fifth region of interaction occurred between $0.67 \leq x^* \leq 1.50$. C_D further decreased for the slower ellipse and remained approximately the same for the faster ellipse (a net increase). The C_L of both ellipses shifted to be attractive, as it was in region 1. C_M changed directions for the slower ellipse, so that the moment of both ellipses was positive.

7.2 Overtaking-Stationary Effects

The overtaking-stationary simulations (results in Section 6.4 and Appendix B) showed the relative motion effects in isolation, since there was no inflow to represent a forward velocity by Ellipse 0. An analysis of the drag, lift, and yaw moment interactions is provided below, along with a discussion of differences from the original overtaking simulations:

Mean Drag Effects As seen in Figure 6-12, the mean drag force on the stationary ellipse was higher than expected and increased alongside u_{rel} in a way that exceeded differences in Re. Despite the ellipse being stationary, its mean drag

force at $(y^*, u_{rel}) = (0.3, 2.00)$ was more than half that of an isolated ellipse at $Re = 1500$ (0.063 versus 0.117, respectively). Changes in drag of the faster ellipse generally remained on pace with changes due to Re. $\Delta C_{D,1}$ decreased at higher u_{rel} but was consistently two to four times the value of $\bar{C}_{D,iso}$ (e.g., $\bar{C}_{D,1} = 0.227$ at $u_{rel} = 2.00$ versus $\bar{C}_{D,iso} = 0.093$ at $Re = 3000$).

Transient Drag Effects The drag coefficient of the faster ellipse experienced large variations and increased alongside u_{rel}, while the drag coefficient of the stationary ellipse was small and experienced only slight variations at different u_{rel}. During the overtaking-stationary maneuver, $\Delta C_{D,1}$ experienced an increase that peaked just prior to $x^* = 0$ at a value nearly 30 times higher than that of an isolated ellipse ($\Delta C_{D,1} = 2.765$ at $u_{rel} = 1.75$ versus $\bar{C}_{D,iso} = 0.0966$ at $Re = 2625$). As in the original overtaking simulations, there was generally an inflection point in drag near $x^* = 0$, after which the faster ellipse experienced a drag benefit. However, this inflection point did not occur at the lowest relative velocity of $u_{rel} = 1.00$, where $C_{D,1}$ remained positive and leveled out to zero instead of becoming negative (see Figure 6-9).

Lift Effects Similar to the drag coefficient, the lift coefficient of the faster ellipse experienced large variations and increased alongside u_{rel}, while the lift coefficient of the stationary ellipse was small and experienced only slight variations at different u_{rel}. The lift interactions of the overtaking-stationary case differed from the original overtaking simulations in that they occurred in two phases instead of one. A repulsive phase occurred while the faster ellipse was located downstream of the slower ellipse ($x^* < 0$). An inflection point occurred at $x^* = 0$, after which the lift became either downward for both ellipses ($u_{rel} = 1.00$ only) or attractive ($u_{rel} \geq 1.25$). The presence of two lift interaction phases with an inflection point at $x^* = 0$ did not occur during the overtaking simulations, where the lift was repulsive for the entire maneuver. The presence of an attractive region in the overtaking-stationary simulation was due to the more pronounced effect of u_{rel} when the velocity of the stationary ellipse was $u_0 = 0$. Without

an inflow present, the faster ellipse created a greater disturbance in the velocity field, making the streamlines around the faster ellipse more diverged and pushing the streamlines around the slower body closer together. This activity caused the flow around the slower body to move faster, resulting in the pressure being lower and the attractive force being greater for the stationary ellipse. The highest $\bar{C}_{L,0}$ for an entire simulation was 0.017 at $(y^*, u_{rel}) = (0.3, 1.75)$ (six percent higher than $\bar{C}_{D,0}$ for the same simulation), and the highest $\bar{C}_{L,1}$ for an entire simulation was -0.356 at $(y^*, u_{rel}) = (0.3, 1.50)$ (seven percent lower than $\bar{C}_{D,1}$ for the same simulation).

Moment Effects C_M in the overtaking-stationary simulations was driven by the magnitude of C_L, which remained the driving interaction for yaw moment over C_D, as it was in the overtaking simulations. Similar to $C_{L,1}$, $C_{M,1}$ experienced two phases: a bow-in phase for $x^* < 0$, and a bow-out phase for $x^* > 0$. The largest instantaneous C_M for the ellipses occurred slightly before $x^* = 0$, with a value of -0.055 for the slower ellipse (at $(y^*, u_{rel}) = (0.3, 1.50)$) and 0.035 for the faster ellipse (at $(y^*, u_{rel}) = (0.3, 1.00)$). These values were quite small and would not have much effect on the movement of the ellipses.

In general, an increase in relative velocity during the overtaking-stationary simulations caused the coefficients of the faster ellipse to increase in magnitude, while producing only slight variations in the coefficients of the stationary ellipse. However, the differences in the faster ellipse were largely accounted for by changes in Reynolds number, whereas the changes in the stationary ellipse were due to the flow interference from the faster ellipse. Neither of the ellipses in the overtaking-stationary simulations experienced the decreases in drag, lift, or moment coefficient that were observed for the faster ellipse during the overtaking simulations. The response to changes in lateral separation was similar to the overtaking simulations, in that the magnitudes of ΔC_D, C_L, and C_M tended to decrease with increasing y^*.

7.3 Periodic Boundary Effects

It was suspected that differences between the results of the overtaking case simulations and the ship overtaking studies could not solely be attributed to differences in Reynolds number or surface effects – but that differences in boundary conditions also played a role. The ship overtaking experiments were performed under standard wall conditions, which had the effect of creating a narrow channel (usually with a shallow draft) that constrained the flow. This effect was desirable for studies of ship maneuvering safety, as it resembled the potentially hazardous situation of ships overtaking each other in a canal or river. Although the numerical simulations of these studies could have used a wider, deeper channel, it was desirable to resemble the conditions of the experiments as closely as possible, and a larger computational domain was counterproductive to this aim – not to mention more computationally expensive. The narrow channel effect was relevant to the ship maneuvering studies, but it enforced a more constrained flow that generally does not apply to UUVs in open water but can affect their interactions in important ways.

To investigate the effect of relative motion with boundary constraints introduced, an ellipse overtaking maneuver was simulated under periodic boundary conditions using various domain widths. These simulations were known as the "moving constraint test" simulations. In the moving constraint test, there was zero inflow ($U_\infty = 0$), Ellipse 0 remained stationary ($U_0 = u_0 = 0$), and Ellipse 1 moved with a velocity of $U_1 = u_1 = 1.00$, 1.50, or 2.00. A lateral spacing of $y^* = 0.3$ was maintained between the ellipses, while the width of the domain was changed to produce different values of d_1/d_2. As with the constraint test simulations described in Section 4.3.2, d_1 represented the distance between centerlines of the ellipses, while d_2 represented the distance between an ellipse and its neighbor in the adjacent periodic cell (see Figure 7-2). The simulated values of d_1/d_2 were 1.00, 1.50, 2.00, 2.50, and 3.00.

Figure 7-3 shows the value of $\bar{C}_L$ for both ellipses with respect to d_1/d_2 at a constant lateral separation of $y^* = 0.3$ and relative velocity of $u_{rel} = 1.00$. The value depicted is from exactly halfway through the overtaking period, when the faster

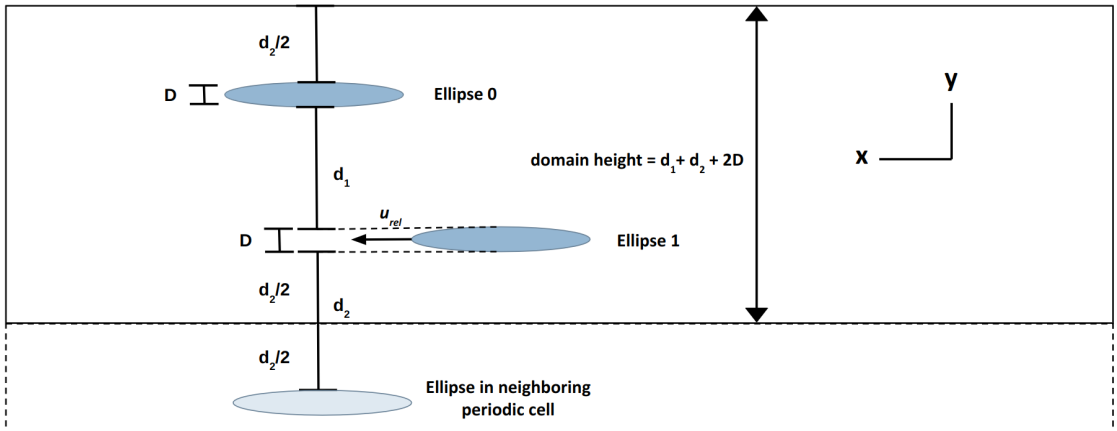

Figure 7-2: Setup of channel for moving constraint test, using periodic boundary conditions

ellipse was side-by-side with the stationary ellipse ($x^* = 0$). The lift for both ellipses was repulsive ($\bar{C}_{L,0} > 0$, $\bar{C}_{L,1} < 0$) at the smallest boundary separation ratio of $d_1/d_2 = 1.0$. When the domain was widened and the boundary separation ratio increased to $d_1/d_2 = 1.5$, the stationary ellipse was attracted to the moving ellipse (i.e., $\bar{C}_{L,0} < 0$). At this value and higher values of d_1/d_2, the ellipses were closer to each other than to the neighboring ellipses in the adjacent periodic cell, causing the interactions between ellipses to dominate over wall effects. The flow interference of the faster ellipse pushed its streamlines further apart, leading to slower flow velocity and higher pressure on the inward side and a repulsive lift force. Meanwhile, the streamlines of the slower ellipse were forced closer together, causing the flow on its inward side to move faster and creating a lower pressure (attractive force). The value of $\bar{C}_{L,0}$ became more negative (attractive) with subsequent increases in d_1/d_2, reaching a value of -0.208 at $d_1/d_2 = 3.0$. The value of $\bar{C}_{L,1}$ became more negative (repulsive) between $d_1/d_2 = 1.0$ and $d_1/d_2 = 1.5$ (going from -0.072 to -0.114), then became less negative with subsequent increases in d_1/d_2. The value of $\bar{C}_{L,1}$ never became positive (attractive) at any point in the maneuver. The lift behavior at higher relative velocities was generally the same, albeit larger in magnitude.

The results of the moving constraint test simulations showed that boundary constraints can affect the attractive or repulsive nature of lift interactions in the overtaking case. Changing the domain width had more of an impact on the lift behavior

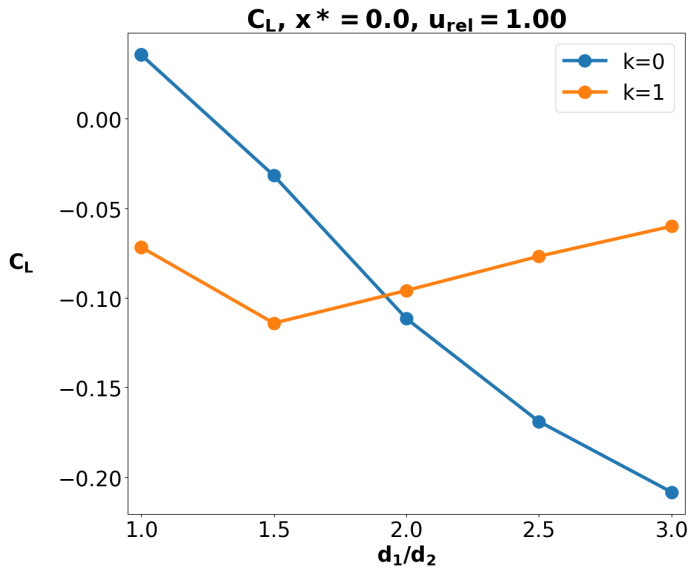

Figure 7-3: Lift behavior of ellipses (one moving, one stationary) at $x^* = 0$ under various boundary separation ratios, d_1/d_2

of the slower ellipse compared to that of the faster ellipse, due to the fact that the faster ellipse produced greater flow interference and as a result "felt" these changes to a lesser extent. This shows that when the lateral forces are of interest, it is important to consider the domain size and type of boundary when modeling an overtaking maneuver or comparing results to other transient studies.

7.4 Comparison to Existing Studies of Transient Motion

The overtaking and overtaking-stationary simulation results were compared to the results of existing literature on transient motion that were introduced in Section 1.1.3. Particular attention was paid to qualitative trends in the force and moment coefficients and how they behaved under different Reynolds numbers, boundary conditions, surface effects (where applicable), and body geometries.

The trends in drag coefficient across all of the studies and flow conditions were generally the same, with any differences attributed to variations in geometry (i.e., ships, spheroids, cylinders, or ellipses) that affected the shape of the drag interaction

regions. Quantitatively, drag coefficient values differed considerably between studies. For example, in the side-by-side configuration at $(x^*, y^*) = (0.00, 0.30)$ during the current study, there was an overall net drag increase of 17.1% for the system, compared to 4.6% at a similar configuration of $(x^*, y^*) = (0.00, 0.27)$ in Rattanasiri et al. [17]. Notable differences occurred in lift coefficient that were generally divided along the lines of Reynolds number and boundary conditions. Table 7.1 summarizes the lift behavior that was observed in each study when bodies were located in the side-by-side configuration. It also provides information about factors that may have contributed to the attractive or repulsive lift behavior – including Reynolds number, lateral separation, domain size, and boundary conditions.

The information in Table 7.1 shows that there was a similar lift behavior between the studies at high Reynolds numbers (including numerical and experimental studies) and in potential flow. In these studies, the forces and moments behaved similarly due to the bluff-body pressure effects dominating over skin friction. The turbulent wake of the bodies (ships, spheroids, etc.) contained a high amount of momentum and energy that caused the separation to occur much later than what would occur at lower Reynolds numbers. As a result, there was no high-pressure area on the inward side of the bodies to produce repulsion (which was observed in the overtaking simulations); instead, there was a high-velocity, low-pressure gap flow between the bodies that produced attraction.

The lift force observed in the overtaking-stationary simulations differed from the high-Re studies, potential flow studies, and overtaking simulations, in that there was a transition from repulsive to attractive lift at $x^* = 0$. Since there was no inflow in the overtaking-stationary simulations, the velocity of flow between the ellipses did not exceed their relative velocity, and the only interaction force present was the interference caused by the moving ellipse. The high-pressure area at the stagnation point of the moving ellipse pushed the ellipses apart for $x^* < 0$ as Ellipse 1 moved into the interaction bow-first. After Ellipse 1 passed Ellipse 0, there was a low-pressure region caused by the flow "filling in" the wake behind Ellipse 1 as it moved away, producing attraction between the ellipses. This result differed from the existing

studies – even when compared to Xiang & Faltinsen (2010) and Yu et al. (2019), who investigated a stationary ship being overtaken by a moving ship and found the side-by-side configuration to yield an attractive lateral force. However, these studies were performed using a narrow channel, which was believed to have an effect on the orientation of lift interactions (as demonstrated in the constraint test simulations in Section 4.3.2).

7.5 Comparison Between Stationary and Overtaking Cases

The stationary and overtaking cases showed the individual contributions of pressure, viscosity, and relative motion to the interactions between ellipses. The results of the stationary and overtaking simulations are compared in this section to comment on differences between the flow cases.

In lieu of differences in lateral separation, whose impact on the magnitude of force coefficients was largely intuitive (higher y^* results in diminished effects, as discussed in Chapter 6), differences in relative velocity are presented in the plots. This presentation allowed the stationary simulations to be viewed as an extension of the overtaking simulations, with $u_{rel} = 0$. The plots of the stationary and overtaking simulations are shown in Figure 7-4.

For Ellipse 0 – whose motion did not change between the stationary and overtaking cases – the drag, lift, and moment coefficients all increased alongside u_{rel}. Apart from these changes in magnitude, there was no difference in the general shape of the plots. The increase in the Ellipse 0 coefficients was attributed to additional interference from Ellipse 1 at higher relative velocities.

The plots of Ellipse 1 coefficients also maintained their general shape between the stationary and overtaking cases, but unlike Ellipse 0, the values of $C_{D,1}$ and $C_{L,1}$ tended to decrease at higher u_{rel}. Although the faster ellipse experienced greater forces, these forces did not keep pace with the inverse relationship between C_D (or

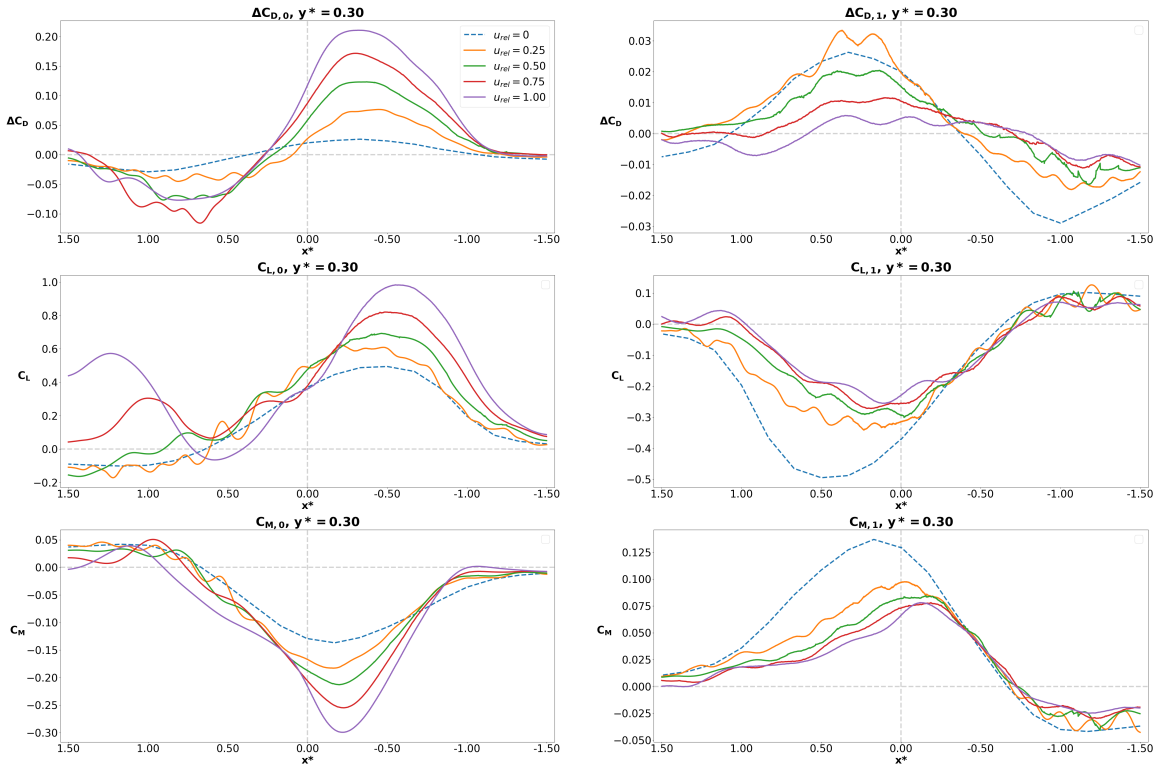

Figure 7-4: Comparison of stationary and overtaking results

C_L) and Re. In terms of force and moment coefficients, therefore, the moving ellipse experienced drag, lift, and moment interactions to a lesser extent when it moved at higher speeds.

In both the stationary and overtaking cases, the Reynolds numbers and boundary conditions were responsible for differences between the results of existing studies and those of the current study. These differences were most pronounced in the lift coefficients, as summarized by Tables 4.2 (stationary case) and 7.1 (overtaking case). The attractive force reproduced by the constraint test simulations (Section 4.3.2), which resembled the results of stationary UUV studies, was not observed in the overtaking simulations. The overtaking simulations gave a purely repulsive lift force between the ellipses. An attractive force was observed in the overtaking-stationary simulations for $x^* > 0$, but the presence of a lift transition at $x^* = 0$ was unique to these simulations.

7.6 Overtaking Case Takeaways

The overtaking case simulations characterized the ellipse interactions in a rotational, viscous flow during an overtaking maneuver. The force and moment interactions between the ellipses were mapped at several lateral separations and relative velocities and compared across different simulation parameters (overtaking and overtaking-stationary). The results were also compared to existing studies of UUVs and ships, as well to as the stationary case. The findings of the different overtaking case simulations are briefly summarized as follows:

Overtaking Under free-space boundary conditions with both ellipses moving, the upstream ellipse experienced a drag increase while the downstream ellipse experienced a drag decrease. For the slower ellipse, the mean drag was mostly unaffected by the overtaking maneuver (i.e., similar to an isolated ellipse at the same speed). Although the initial instantaneous drag increase reached more than two and a half times that of an isolated ellipse at the highest u_{rel}, this was matched by a similar drag reduction during the second half of the maneuver. The drag of the faster ellipse was relatively unaffected, both in its mean value and in its degree of variation during the maneuver. The lift interaction was repulsive for the entire overtaking maneuver. The slower ellipse experienced a significant increase in mean repulsive lift as a result of the overtaking maneuver that became greater as the overtaking speed increased (up to twice the value compared to when $u_{rel} = 0$).

Overtaking-Stationary When one ellipse was stationary, there was a net drag increase for both ellipses throughout the maneuver, and the lift transitioned from repulsive to attractive at $x^* = 0$. As the speed of the overtaking ellipse increased, the stationary ellipse experienced significant increases in its mean and instantaneous drag forces, with the mean drag reaching more than half the value of an isolated ellipse moving at $Re = 1500$. The lift force of the slower ellipse also changed significantly at higher u_{rel}, with peak and mean values similar to the drag force. While it was located downstream of the stationary ellipse, the

overtaking ellipse experienced an increase in peak drag force of up to 30 times that of an isolated ellipse at the same speed, along with an increase in mean drag by a factor of three to four at all relative velocities. The overtaking ellipse also experienced large changes in lift coefficient and mean lift during the overtaking maneuver that were similar in magnitude to the drag.

Boundary conditions and Reynolds number played a role in the differences between previous studies of transient motion and the current study. Compared to the stationary case, the behavior of the drag, lift, and moment coefficients was generally the same, albeit with changes in magnitude attributed to the relative velocity of the faster ellipse.

An important takeaway from the overtaking case results is that during an overtaking maneuver in close proximity, UUVs are subject to significant changes in lift and yaw moments due to viscous and pressure interactions between them. It is expected that these interactions tend to increase the difficulty of maneuvering and need to be corrected by steering. In general, if an overtaking maneuver is necessary, the UUVs can limit their interactive forces by passing as far apart as possible and at a low relative speed. Whether the UUVs are operated remotely by a human or are programmed to operate independently, coordination between the vessels during an overtaking maneuver is perhaps the most effective way to avoid a collision or being forced off course. This coordination requires knowledge of a UUV's own position and its position relative to surrounding UUVs, as well as providing enough space to compensate for changes in the flow field due to interaction and interference.

Table 7.1: Comparison of lateral (lift) force results of bodies in the side-by-side configuration from various overtaking studies. (N) = numerical, (A) = analytical, (E) = experimental

Study	**Model**	$\boldsymbol{Re}$	$\boldsymbol{y^*}$; **Domain** $\boldsymbol{L \times W}$	**Boundary Condition**	$\boldsymbol{C_L}$, $\boldsymbol{x^* = 0}$	$\boldsymbol{C_L}$, $\boldsymbol{\lvert x^* \rvert = 0.5}$
Current Study (N)	Overtaking simulations	$\mathcal{O}(10^3)$	$0.3 - 0.6$; $13.2L \times 6.6L$	Free	Repulsive	Attractive
Current Study (N)	Overtaking-stationary simulations	$\mathcal{O}(10^3)$	$0.3 - 0.6$; $13.2L \times 6.6L$	Free	Repulsive-Attractive Transition	Repulsive ($x^* < 0$); Attractive ($x^* > 0$)
Skejic & Faltinsen (2007) (N)	Ships	Potential Flow	~ 0.2; N/A	Free	Attractive	Repulsive
Wang (2007) (A)	Slender bodies of revolution	Potential Flow	$0.1 - 0.3$; N/A	Free	Attractive	Repulsive
Xiang & Faltinsen (2010) (N)	Ships (one stationary)	Potential Flow	~ 0.3; N/A	Free	Attractive	Repulsive
Leong et al. (2013) (N, E)	UUV and submarine	$\mathcal{O}(10^6)$	$\sim 0.4 - 0.6$; $27.8L \times 2.5L$	Standard Wall	Attractive	Repulsive
Yuan et al. (2015) (N)	Ships	$\mathcal{O}(10^6)$	$\sim 0.2 - 0.3$; $5L \times 2L$	Standard Wall	Attractive	Repulsive
Yu et al. (2019) (N, E)	Ships (one stationary)	$\mathcal{O}(10^6)$	0.3; $52.5L \times 1.7L$	Standard Wall	Attractive	Repulsive
Zhang et al. (2019a) (N)	UUV and larger UUV	$\mathcal{O}(10^6)$	$0.1 - 0.4$; $15L \times 6L$	Standard Wall	Attractive	Repulsive
Vantorre et al. (2002) (E)	Ships	$\mathcal{O}(10^6)$	$0.3 - 0.6$; $\sim 20L \times 2L$	Standard Wall	Attractive	Repulsive
Muscat-Fenech et al. (2022) (N)	Ships (Review)	$\mathcal{O}(10^6)$	Various	Various	Attractive	Repulsive

Chapter 8

Conclusions

In this study, two identical 6:1 ellipses in close proximity were investigated in side-by-side, staggered, and tandem configurations as well as in overtaking maneuvers at various speeds and lateral separations. The initial numerical simulations used a 2D, rotational, viscous flow with free-space boundary conditions and a constant-velocity inflow. Follow-on simulations explored the effects of periodic boundaries, different domain widths, and zero-velocity inflow. The goal of the simulations was to characterize the hydrodynamic interactions between ellipses and to determine the roles of viscous effects, boundary conditions, and relative motion in these interactions.

It was found that under zero relative motion (stationary case), ellipse interactions could be divided into five regions based on the change in drag coefficients of the two ellipses, as well as the net change in overall drag for the system. The results of the stationary case largely agreed with the interactions characterized by 2D cylinder studies with respect to drag and lift. Of particular interest from existing biological and UUV studies, the "echelon" position was found to produce up to a 20% drag decrease for the downstream ellipse at the cost of a similar increase in drag for the upstream ellipse. The lift was repulsive and, for the closest parallel configuration, about four times the total drag on either ellipse. Based on this result, the lift force is expected to dominate in a practical scenario, and any drag benefit will likely be significantly reduced after accounting for the UUVs maneuvering to maintain formation. Upon observing differences in repulsion and attraction between the current study and studies of ships and

UUVs in turbulent flow regimes, the role of boundary conditions was investigated. It was found that under periodic boundary conditions in the side-by-side configuration, an attractive force akin to the turbulent-study results occurred when the ellipses were placed closer to their neighboring ellipses in the adjacent cell (i.e., $d_1 > d_2$).

Introducing relative motion (overtaking case) produced different interaction behaviors compared to the stationary case, due to the changing relative positions between ellipses and the higher flow interference of the faster ellipse. The mean drag of the slower ellipse was mostly unaffected by the overtaking maneuver, but there were large variations in drag within an individual simulation – particularly at higher relative velocities. While located upstream of the faster ellipse, the slower ellipse experienced a peak drag variation (increase) of up to 2.5 times that of an isolated ellipse. This increase was matched by a similar drag decrease in the second half of the maneuver. For the faster ellipse, the mean drag was mostly unaffected by the overtaking maneuver. The drag variations within a maneuver were smaller compared to the slower ellipse, and they decreased in magnitude at higher relative velocities. The lift interaction between the ellipses was repulsive for the entire maneuver. The slower ellipse experienced a significant increase in its mean lift – up to 2.5 times the value of the stationary case – and a large peak variation that increased alongside the relative velocity. For the faster ellipse, the lift experienced a much smaller mean value and peak variation compared to the slower ellipse, and these values decreased in magnitude at higher relative velocities.

When one ellipse was stationary and the other overtook at a constant velocity, the drag variation for both ellipses remained positive throughout the maneuver. As the overtaking speed increased, the mean drag on the stationary ellipse increased significantly, reaching more than half the value of an isolated ellipse moving at $Re = 1500$. The mean drag of the overtaking ellipse increased by a factor of three to four at all relative velocities compared to an isolated ellipse. While located downstream of the stationary ellipse, the overtaking ellipse experienced a peak drag variation of up to 30 times that of an isolated ellipse. The lift interaction between the ellipses transitioned from repulsive to attractive when the moving ellipse passed abeam of

the stationary ellipse ($x^* = 0$). The lift of both ellipses changed significantly, with a mean value and peak variation that were similar in magnitude to the drag.

In general, high lift and moment coefficients were present in close proximity, pointing to the need for careful maneuvering of UUVs to avoid collision. A possible option for safe maneuvering would be for one UUV to approach the other from a steep lateral angle, so that the ellipses do not experience large changes in yaw moments that make it difficult for them to properly steer. Such an approach would also prevent one ellipse from being caught in the wake of the other and losing maneuverability.

8.1 Recommendations for Future Study

A follow-on study might use the results of the stationary and overtaking cases to determine safe and efficient procedures for refueling, docking, release, and recovery of UUVs. Such a study might consider the steepness of approach, speeds of the vehicles, and angles of attack as additional variables. The results can either be used to inform operator procedures for remotely-controlled UUVs or to inform the programming of autonomous or semi-autonomous UUVs.

Another possibility for follow-on studies would be to further generalize the results by manipulating the simulation parameters used in this study. A non-exhaustive list of options might include:

Expanded range of Reynolds numbers A substantial gap exists between the knowledge of interactions at laminar and turbulent Reynolds numbers. The simulator used for this study is currently limited to a Reynolds number of $\mathcal{O}(10^3)$, and most biological and UUV applications occur at $\mathcal{O}(10^6)$. Expanding the range of the simulator, or using a different simulator that is adapted to both transitional flow regimes and relative motion, would allow researchers to investigate changes in ellipse interactions at the intervening Reynolds numbers (i.e., $\mathcal{O}(10^4 - 10^5)$).

Ellipses of differing sizes and/or aspect ratios The results of this study could be expanded by modeling the interactions between different-sized UUV designs

or the interactions between a UUV and a much larger submarine (as in Leong et al. [10] and Randeni P. et al. [16]). It is expected that smaller length-to-width ratios would approach the solution for identical cylinders described by Zdravkovich [34], and that larger aspect ratios would begin to resemble the characteristics of steady flow past a flat plate.

Cost of Maneuvering When multiple UUVs move in close proximity in an operational environment, the interaction forces cause them to deviate from their original positions and must be counteracted by steering. Steering an ellipse by changing its angle of attack creates a corresponding change (usually an increase) in drag coefficient. A follow-on investigation might estimate the cost (in terms of additional drag) of steering the ellipses to maintain their relative positions. The investigation would begin by investigating configurations in this study that were shown to produce a drag benefit for one or both ellipses.

Attack Angle Effects The ellipse configurations included in this study could be investigated at different angles of attack relative to the incoming flow. Understanding the behavior of force interactions under these conditions is relevant to real-life UUV operations, because UUVs operate in currents that are not parallel to their path of travel. For more discussion on this topic, readers are referred to Andersson and Jiang [2], who investigated the effect of attack angle on spheroids at low Reynolds numbers and demonstrated the importance of domain size in calculating accurate force and moment coefficients.

Multiple UUVs The results of this study could be expanded by introducing an additional ellipse or ellipses to observe effects of the so-called "vee" formation, or perhaps an extended echelon or tandem configuration. One related study is from Zhang et al. [36], who investigated the hydrodynamics of multiple UUVs operating in tandem and found that the drag effects tended to be most pronounced on the first and last UUVs. It was also found that drag for the overall system tended to decrease when additional UUVs were introduced, and that occasional sharp increases in drag were attributable to areas of undesirable influence from

vorticity [36].

In addition to expanding the existing parameters included in this study, certain UUV characteristics present in most real-world designs (but omitted from this study) could be added to future investigations:

Rudders It is expected that the use of rudders for steering would change the flow characteristics behind the UUVs. UUVs that rely on a rudder for steering must also travel at a certain minimum speed to maintain steerage. A follow-on investigation might introduce rudders to the back of the ellipses to study the effect on interaction behavior. These findings could be incorporated into an analysis of maneuvering cost or attack angle effects listed above.

Propellers The force interactions that were calculated in the simulations did not account for the effects of propellers. Since propellers are used by nearly all UUVs, a future study might seek to account for propeller effects numerically (using an actuator disk model, perhaps) and/or experimentally. The presence of a propeller wake alters flow field characteristics, particularly in the tandem and staggered regions behind the upstream UUV. This alteration could affect the mutual drag benefit observed in the tandem and staggered positions during the current study. Readers are referred to Rattanasiri et al. [18] for additional discussion related to this topic area.

Fins and/or Stings Many UUV designs feature fins for stability and steering and/or a sting to promote flow attachment to the body for reduced drag. Although fins and stings were not included in this study, they affect the hydrodynamics of an individual UUV; by extension, they may also affect the interactions between two or more UUVs. A more specialized study of a specific UUV model may consider incorporating such design-specific features.

3D axisymmetric shapes The simulations could be repeated using a three-dimensional simulation with prolate spheroids to represent the UUVs. Although this study proceeded on the expectation that the 2D results would closely resemble 3D on

account of geometric axisymmetry, the use of 2D nonetheless limited the extent to which the results could be quantitatively compared to existing UUV studies, which were almost all in 3D.

Bibliography

[1] M. M. Alam, M. Moriya, and H. Sakamoto. Aerodynamic characteristics of two side-by-side circular cylinders and application of wavelet analysis on the switching phenomenon. *Journal of Fluids and Structures*, 18:325–346, July 2003.

[2] H. I. Andersson and F. Jiang. Forces and torques on a prolate spheroid: low-reynolds number and attack angle effects. *Acta Mechanica*, 230(2):431–447, 2019.

[3] I. Ashraf, H. Bradshaw, T. Ha, J. Halloy, R. Godoy-Diana, and B. Thiria. Simple phalanx pattern leads to energy saving in cohesive fish schooling. In *Proceedings of the National Academy of Sciences*, number 36 in 114, pages 9599–9604, September 2017.

[4] B. Blocken, T. Defraeye, E. Koninckx, J. Carmeliet, and P. Hespel. Cfd simulations of the aerodynamic drag of two drafting cyclists. *Computers and Fluids*, 71:435–445, November 2022.

[5] L. Chen, J. Y. Tu, and G. H. Yeoh. Numerical simulation of turbulent wake flows behind two side-by-side cylinders. *Journal of Fluids and Structures*, 18:387–403, 2003.

[6] J. Gabbard, T. Gillis, P. Chatelain, and W. M. van Rees. An immersed interface method for the 2d vorticity-velocity navier-stokes equations with multiple bodies. *Journal of Computational Physics*, 464, May 2022.

[7] S. F. Hoerner. *Fluid-Dynamic Drag*, chapter 8.1. Hoerner Fluid Dynamics, Bakersfield, CA, 1965.

[8] E. Hori. Experiments on flow around a pair of parallel circular cylinders. In *Proc. 9th Japan National Congress for Applied Mech.*, pages 231–234, Tokyo, 1959.

[9] X. Ji. An immersed interface method for the simulation of two-way coupling fluid-body problems. Presentation handout, October 2022.

[10] Z. Q. Leong, K. A. M. Saad, D. Ranmuthugala, and J. Duffy. Investigation into the hydrodynamic interaction effects on an auv operating close to a submarine. In *Proc. Pacific Int. Maritime Conf., Commercial Maritime Nav. Defence Showcase Asia-Pacific*, pages 1–11, 2013.

[11] A. F. Molland and I. K. A. P. Utama. Experimental and numerical investigations into the drag characteristics of a pair of ellipsoids in close proximity. In *Proc Instn Mech Engrs Vol 216 Part M: J Engineering for the Maritime Environment*, pages 107–115, 2002.

[12] C. D. Muscat-Fenech, T. Sant, V. V. Zheku, D. Villa, and M. Martelli. A review of ship-to-ship interactions in calm waters. *Journal of Marine Science and Engineering*, 10:1856, December 2022.

[13] S. R. Noren and E. F. Edwards. Infant position in mother-calf dolphin pairs: formation locomotion with hydrodynamic benefits. In *Marine Ecology Progress Series*, volume 424, pages 229–236, March 2011.

[14] B. L. Partridge and T. J. Pitcher. Evidence against a hydrodynamic function for fish schools. *Nature*, 279:418–419, May 1979.

[15] I. Peschard and P. Le Gal. Coupled wakes of cylinders. *Physical Review Letters*, 77:3122–3125, 1996.

[16] S. A. T. Randeni P., Z. Q. Leong, D. Ranmuthugala, A. L. Forrest, and J. Duffy. Numerical investigation of the hydrodynamic interaction between two underwater bodies in relative motion. *Applied Ocean Research*, 51:14–24, February 2015.

[17] P. Rattanasiri, P. A. Wilson, and A. B. Phillips. Numerical investigation of a fleet of towed auvs. *Ocean Engineering*, 80:25–35, February 2014.

[18] P. Rattanasiri, P. A. Wilson, and A. B. Phillips. Numerical investigation of a pair of self-propelled auvs operating in tandem. *Ocean Engineering*, 100:126–137, April 2015.

[19] G. F. Romberg, Jr. F. Chianese, and R. G. Lajoie. Aerodynamics of race cars in drafting and passing situations. In *Society of Automotive Engineers Automotive Engineering Congress*, pages 1–8, Detroit, MI, 1971.

[20] S. K. P. Sanjeevi, J. A. M. Kuipers, and J. T. Padding. Drag, lift, and torque correlations for non-spherical particles from stokes limit to high reynolds numbers. *International Journal of Multiphase Flow*, 106:325–337, May 2018.

[21] K. Shoele and Q. Zhu. Drafting mechanisms between a dolphin mother and calf. *Journal of Theoretical Biology*, 382:363–377, July 2015.

[22] R. Skejic and O. M. Faltinsen. A unified seakeeping and maneuvering analysis of two interacting ships. In *International Conference on Hydrodynamics*, pages 209–218, 2007.

[23] D. Sumner. Two circular cylinders in cross-flow: A review. *Journal of Fluids and Structures*, 26:849–899, July 2010.

[24] D. Sumner, S. S. T. Wong, S. J. Price, and M. P. Paidoussis. Fluid behavior of side-by-side circular cylinders in steady cross-flow. *Journal of Fluids and Structures*, 13:309–338, 1999.

[25] W. Tian, Z. Mao, F. Zhao, and Z. Zhao. Layout optimization of two autonomous underwater vehicles for drag reduction with a combined cfd and neural network method. *Complexity*, 2017:1–15, November 2017.

[26] M. Vantorre, E. Verzhbitskaya, and E. Laforce. Model test based formulations of ship-ship interaction forces. *Ship Technology Research*, 49:124–141, 2002.

[27] Q. X. Wang. An analytical solution for two slender bodies of revolution translating in very close proximity. *Journal of Fluid Mechanics*, 582:223–251, January 2007.

[28] Z. J. Wang, Y. Zhou, and H. Li. Flow-visualization of a two side-by-side cylinder wake. *Journal of Flow Visualization & Image Processing*, 9:123–128, 2002.

[29] D. Weihs. Hydromechanics of fish schooling. *Nature*, 241:290–291, September 1973.

[30] D. Weihs. The hydrodynamics of dolphin drafting. *Journal of Biology*, 3:8, May 2004.

[31] X. Xiang and O. M. Faltinsen. Maneuvering of two interacting ships in calm water. In *11th International Symposium on Practical Design of Ships and Other Floating Structures*, Rio de Janiero, 2010.

[32] D. Yu, L. Wang, and R. W. Yeung. Experimental and numerical study of ship-to-ship interactions in overtaking manoeuvres. In *Proceedings of the Royal Society A*, number 20180748 in 475. Royal Society, April 2019.

[33] Z. Yuan, S. He, P. Kellett, A. Incecik, O. Turan, and E. Boulougouris. Ship-to-ship interaction during overtaking operation in shallow water. *Journal of Ship Research*, 59(3):172–187, September 2015.

[34] M. M. Zdravkovich. Review of flow interference between two circular cylinders in various arrangments. *Transactions of the American Society of Mechanical Engineers*, 99:618–633, December 1977.

[35] D. Zhang, L. Chao, and G. Pan. Analysis of hydrodynamic interaction impacts on a two-auv system. *Ships and Offshore Structures*, 14(1):23–34, June 2019.

[36] D. Zhang, G. Pan, Y. Shi, P. Wang, and L. Chao. Investigation of the resistance characteristics of a multi-auv system. *Applied Ocean Research*, 89:59–70, 2019.

THIS PAGE INTENTIONALLY LEFT BLANK

Appendix A

Sample Simulation Parameters

This appendix provides examples of the inputs that were placed into each simulation – called "factory" and "settings" files – that established parameters such as the domain size, shape geometries, and fluid properties to be used in each simulation.

Aspect ratio simulation settings, here with 1:1 aspect ratio and spacing $0.30L$, where L is the original length of the ellipses (1.2).

```
obstacle ellipse % type of obstacle (shape) that was used
    xpos      1.6 % x-position, with x=0 at the left boundary
    ypos      3.43 % y-position, with y=0 at the bottom boundary
    rx        0.1 % x-radius
    ry        0.1 % y-radius
    theta0    0.0 % angle of attack


obstacle ellipse   % second ellipse
    xpos     1.6
    ypos     3.07
    rx       0.1
    ry       0.1
    theta0   0.0

SETTINGS=" "
```

```
SETTINGS+="␣–study␣fixed" % all shapes are fixed in the domain
SETTINGS+="␣–bpdx␣102" % points per horizontal grid unit
SETTINGS+="␣–bpdy␣51" % points per vertical grid unit
SETTINGS+="␣–maxextent␣13.0" % total size of the domain
SETTINGS+="␣–safetyfactor␣0.7"
SETTINGS+="␣–tmax␣60" % duration of the simulation, in seconds
SETTINGS+="␣–tprint␣1.00"
SETTINGS+="␣–tsave␣0.01"
SETTINGS+="␣–nu␣8.000e–4" % kinematic viscosity
SETTINGS+="␣–Uinfx␣1.0" % velocity of incoming horizontal flow
SETTINGS+="␣–Uinfy␣0.0" % velocity of incoming vertical flow
SETTINGS+="␣–freestream␣bump" % uses free stream bump
SETTINGS+="␣–Ubump␣0.0" % horizontal velocity bump (none here)
SETTINGS+="␣–Vbump␣0.50" % max vertical bump velocity
SETTINGS+="␣–Tbump␣1.2" % time of velocity bump peak
SETTINGS+="␣–Wbump␣1.0"
SETTINGS+="␣–bOutflow␣1" % graceful exit of vorticity
SETTINGS+="␣–ramptime␣0.005" % flow startup
SETTINGS+="␣–rampsize␣1e–3"
SETTINGS+="␣–tol␣1e–9" % tolerance of calculations
SETTINGS+="␣–nRecycle␣60"
```

Constraint test simulation settings, here with $d_1/d_2 = 0.36$. The domain size was kept the same, and the ellipses were re-positioned between simulations (with respect to y) so that different values of d_1/d_2 could be attained.

```
obstacle ellipse
    xpos      1.60
    ypos      0.68 % changed to create different d1/d2
    rx        0.6
    ry        0.1
    theta0    0.0

obstacle ellipse
    xpos     1.60
    ypos     0.32 % changed to create different d1/d2
    rx       0.6
    ry       0.1
    theta0   0.0

SETTINGS=""
SETTINGS+="␣--study␣fixed"
SETTINGS+="␣--bpdx␣102"
SETTINGS+="␣--bpdy␣8" % narrow y-domain
SETTINGS+="␣--maxextent␣13.0"
SETTINGS+="␣--safetyfactor␣0.7"
SETTINGS+="␣--tmax␣40.0" % large tmax to achieve steady-state
SETTINGS+="␣--tprint␣1.00"
SETTINGS+="␣--tsave␣0.01"
SETTINGS+="␣--nu␣8.000e-4"
SETTINGS+="␣--Uinfx␣1.0"
SETTINGS+="␣--Uinfy␣0.0"
SETTINGS+="␣--freestream␣bump"
```

```
SETTINGS+="␣–Ubump␣0.0"
SETTINGS+="␣–Vbump␣0.50"
SETTINGS+="␣–Tbump␣1.2"
SETTINGS+="␣–Wbump␣1.0"
SETTINGS+="␣–bPeriodic␣1" % periodic boundaries
SETTINGS+="␣–bOutflow␣0"
SETTINGS+="␣–ramptime␣0.005"
SETTINGS+="␣–rampsize␣1e–3"
SETTINGS+="␣–tol␣1e–9"
SETTINGS+="␣–nRecycle␣60"
```

Simulation settings for the periodic mapping simulations, using a single ellipse as the unit cell (axis-aligned). The domain width was set so that the longitudinal spacing between ellipses would be $x^* = -1.50$ and the lateral spacing between ellipses would be $y^* = 0.6$.

```
obstacle ellipse
    xpos      0.90
    ypos      0.36
    rx        0.6
    ry        0.1
    theta0    0.0

SETTINGS=""
SETTINGS+=" --study fixed"
SETTINGS+=" --bpdx 20"
SETTINGS+=" --bpdy 8"
SETTINGS+=" --maxextent 1.8"
SETTINGS+=" --safetyfactor 0.7"
SETTINGS+=" --tmax 60"
SETTINGS+=" --tprint 1.00"
SETTINGS+=" --tsave 0.01"
SETTINGS+=" --nu 8.000e-4"
SETTINGS+=" --Uinfx 1.0"
SETTINGS+=" --Uinfy 0.0"
SETTINGS+=" --freestream bump"
SETTINGS+=" --Ubump 0.0"
SETTINGS+=" --Vbump 0.50"
SETTINGS+=" --Tbump 1.2"
SETTINGS+=" --Wbump 1.0"
SETTINGS+=" --bPeriodic 1"
SETTINGS+=" --ramptime 0.005"
```

```
SETTINGS+="␣-rampsize␣1e-3"
SETTINGS+="␣-tol␣1e-9"
SETTINGS+="␣-nRecycle␣60"
```

Simulation settings for the periodic mapping simulations, using an ellipse pair as the unit cell (staggered). The domain width was set so that the longitudinal spacing between ellipses would be $x^* = -1.50$ and the lateral spacing between ellipses would be $y^* = 0.6$.

```
obstacle ellipse
    xpos      0.90
    ypos      1.08
    rx        0.6
    ry        0.1
    theta0    0.0

obstacle ellipse
    xpos     2.70
    ypos     0.36
    rx       0.6
    ry       0.1
    theta0   0.0

SETTINGS=""
SETTINGS+=" --study fixed"
SETTINGS+=" --bpdx 40"
SETTINGS+=" --bpdy 16"
SETTINGS+=" --maxextent 3.6"
SETTINGS+=" --safetyfactor 0.7"
SETTINGS+=" --tmax 60"
SETTINGS+=" --tprint 1.00"
SETTINGS+=" --tsave 0.01"
SETTINGS+=" --nu 8.000e-4"
SETTINGS+=" --Uinfx 1.0"
SETTINGS+=" --Uinfy 0.0"
```

```
SETTINGS+="␣-freestream␣bump"
SETTINGS+="␣-Ubump␣0.0"
SETTINGS+="␣-Vbump␣0.50"
SETTINGS+="␣-Tbump␣1.2"
SETTINGS+="␣-Wbump␣1.0"
SETTINGS+="␣-bPeriodic␣1"
SETTINGS+="␣-ramptime␣0.005"
SETTINGS+="␣-rampsize␣1e-3"
SETTINGS+="␣-tol␣1e-9"
SETTINGS+="␣-nRecycle␣60"
```

Simulation settings for an isolated ellipse in a free stream at different flow velocities, here with $U_\infty = 1.00$. The only variable that changed between simulations was U_∞, which was also set to values of 1.25, 1.50, 1.75, and 2.00.

```
obstacle ellipse
    xpos      2.00
    ypos      3.35
    rx        0.6
    ry        0.1
    theta0    0.0

SETTINGS=""
SETTINGS+=" --study moving"
SETTINGS+=" --bpdx 60"
SETTINGS+=" --bpdy 30"
SETTINGS+=" --maxextent 13.4"
SETTINGS+=" --safetyfactor 0.7"
SETTINGS+=" --tmax 36.0"
SETTINGS+=" --tprint 0.50"
SETTINGS+=" --tsave 0.01"
SETTINGS+=" --nu 8.000e-4"
SETTINGS+=" --Uinfx 1.0" % independent variable
SETTINGS+=" --Uinfy 0.0"
SETTINGS+=" --freestream bump"
SETTINGS+=" --Ubump 0.0"
SETTINGS+=" --Vbump 0.5"
SETTINGS+=" --Tbump 1.2"
SETTINGS+=" --Wbump 1.0"
SETTINGS+=" --bOutflow 1"
SETTINGS+=" --ramptime 0.005"
SETTINGS+=" --rampsize 1e-3"
```

```
SETTINGS+="␣-tol␣1e-9"
```

Moving constraint test simulations with periodic boundary conditions, here using $d_1/d_2 = 1.0$, $y^* = 0.3$, and $u_{rel} = 1.00$.

```
obstacle ellipse
    xpos      2.60
    ypos      0.54
    rx        0.6
    ry        0.1
    theta0    0.0


obstacle rampup_ellipse
    xpos     4.40
    ypos     0.18
    rx       0.6
    ry       0.1
    theta0   0.0
    Ubx      1.00
    Uby      0.0
    wb       0.0
    T        3.00
    delay    0.0

SETTINGS=""
SETTINGS+=" --study moving"
SETTINGS+=" --bpdx 164"
SETTINGS+=" --bpdy 8"
SETTINGS+=" --maxextent 15.8"
SETTINGS+=" --safetyfactor 0.7"
SETTINGS+=" --tmax 6.6"
SETTINGS+=" --nsave 100"
SETTINGS+=" --tprint 1.00"
```

```
SETTINGS+="␣-nu␣8.000e-4"
SETTINGS+="␣-Uinfx␣0.0"
SETTINGS+="␣-Uinfy␣0.0"
SETTINGS+="␣-bPeriodic␣1"
SETTINGS+="␣-ramptime␣0.005"
SETTINGS+="␣-rampsize␣1e-3"
SETTINGS+="␣-tol␣1e-9"
```

Overtaking-stationary simulations with free boundary conditions, here using the combination of $(y^*, u_{rel}) = (0.30, 1.00)$.

```
obstacle ellipse
    xpos      2.60 % stationary for the whole simulation
    ypos      4.13 % changed between simulations
    rx        0.6
    ry        0.1
    theta0    0.0


obstacle rampup_ellipse
    xpos     4.40 % position when "transient region" begins
    ypos     3.77 % changed between simulations
    rx       0.6
    ry       0.1
    theta0   0.0
    Ubx      1.00 % velocity of overtake; changed between simulations
    Uby      0.0
    wb       0.0
    T        3.00 % time used to ramp up the ellipse velocity
    delay    0.0 % simulations started right away

SETTINGS=""
SETTINGS+=" --study moving"
SETTINGS+=" --bpdx 102"
SETTINGS+=" --bpdy 51"
SETTINGS+=" --maxextent 15.8"
SETTINGS+=" --safetyfactor 0.7"
SETTINGS+=" --tmax 6.6"
SETTINGS+=" --tprint 1.00"
SETTINGS+=" --tsave 0.01"
```

```
SETTINGS+="␣-nu␣8.000e-4"
SETTINGS+="␣-Uinfx␣0.0" % zero inflow velocity
SETTINGS+="␣-Uinfy␣0.0"
SETTINGS+="␣-bPeriodic␣0"
SETTINGS+="␣-bOutflow␣1" % free outflow boundary
SETTINGS+="␣-ramptime␣0.005"
SETTINGS+="␣-rampsize␣1e-3"
SETTINGS+="␣-tol␣1e-9"
```

Finding the resolution for two identical ellipses, here with the resolution of 172 ppl that was chosen for follow-on simulations.

```
obstacle ellipse
    xpos      1.0
    ypos      2.18
    rx        0.6
    ry        0.1
    theta0    0.0


obstacle ellipse
    xpos      1.0 % side-by-side configuration
    ypos      1.82 % lateral spacing y*=0.3 apart
    rx        0.6
    ry        0.1
    theta0    0.0

SETTINGS=""
SETTINGS+=" --study fixed"
SETTINGS+=" --bpdx 36" % changed between simulations
SETTINGS+=" --bpdy 18" % set to 1/2 bpdx
SETTINGS+=" --maxextent 8.0"
SETTINGS+=" --safetyfactor 0.7"
SETTINGS+=" --tmax 35.0"
SETTINGS+=" --tprint 1.00"
SETTINGS+=" --tsave 0.01"
SETTINGS+=" --nu 1.600e-3"
SETTINGS+=" --Uinfx 2.0" % overtaking speed is limiting case
SETTINGS+=" --Uinfy 0.0"
SETTINGS+=" --freestream bump"
SETTINGS+=" --Ubump 0.0"
```

```
SETTINGS+="␣–Vbump␣1.0"
SETTINGS+="␣–Tbump␣1.2"
SETTINGS+="␣–Wbump␣1.0"
SETTINGS+="␣–bOutflow␣1"
SETTINGS+="␣–ramptime␣0.005"
SETTINGS+="␣–rampsize␣1e–3"
SETTINGS+="␣–tol␣1e–9"
SETTINGS+="␣–nRecycle␣60"
```

Finding the domain size for two identical ellipses, here with the domain size of 9 lengths behind the ellipses, which was chosen for follow-on simulations. Note that the viscous mapping simulations used the same factory and settings as below, except that the x- and y-positions of the ellipses were changed to produce the desired relative configurations, and adjustments were made to maintain consistent resolution and domain length behind the trailing ellipse.

```
obstacle ellipse
    xpos      1.6
    ypos      3.43
    rx        0.6
    ry        0.1
    theta0    0.0

obstacle ellipse
    xpos      1.6 % side-by-side configuration
    ypos      3.07 % lateral spacing y*=0.3
    rx        0.6
    ry        0.1
    theta0    0.0

SETTINGS=""
SETTINGS+=" --study fixed"
SETTINGS+=" --bpdx 58" % maintained resolution of 172 ppl
SETTINGS+=" --bpdy 29"
SETTINGS+=" --maxextent 13.00" % changed between simulations
SETTINGS+=" --safetyfactor 0.7"
SETTINGS+=" --tmax 25.0"
SETTINGS+=" --tprint 1.00"
SETTINGS+=" --tsave 0.01"
SETTINGS+=" --nu 1.600e-3"
```

```
SETTINGS+="␣-Uinfx␣2.0"
SETTINGS+="␣-Uinfy␣0.0"
SETTINGS+="␣-freestream␣bump"
SETTINGS+="␣-Ubump␣0.0"
SETTINGS+="␣-Vbump␣0.75"
SETTINGS+="␣-Tbump␣1.2"
SETTINGS+="␣-Wbump␣1.0"
SETTINGS+="␣-bOutflow␣1"
SETTINGS+="␣-ramptime␣0.005"
SETTINGS+="␣-rampsize␣1e-3"
SETTINGS+="␣-tol␣1e-9"
SETTINGS+="␣-nRecycle␣60"
```

Finding the resolution for a single ellipse in a viscous free stream, here with the resolution of 154 ppl that was chosen for follow-on simulations.

```
obstacle ellipse
    xpos      1.0
    ypos      2.0
    rx        0.6
    ry        0.1
    theta0    0.0

SETTINGS=""
SETTINGS+=" --study fixed"
SETTINGS+=" --bpdx 32" % changed to produce different resolutions
SETTINGS+=" --bpdy 16" % set to 1/2 bpdx
SETTINGS+=" --maxextent 8.0"
SETTINGS+=" --safetyfactor 0.7"
SETTINGS+=" --tmax 15.0"
SETTINGS+=" --tprint 1.00"
SETTINGS+=" --tsave 0.01"
SETTINGS+=" --nu 1.600e-3"
SETTINGS+=" --freestream bump"
SETTINGS+=" --Uinfx 2.0"
SETTINGS+=" --Uinfy 0.0"
SETTINGS+=" --Ubump 0.0"
SETTINGS+=" --Vbump 1.0"
SETTINGS+=" --Tbump 1.2"
SETTINGS+=" --Wbump 1.0"
SETTINGS+=" --bOutflow 1"
SETTINGS+=" --ramptime 0.005"
SETTINGS+=" --rampsize 1e-3"
SETTINGS+=" --tol 1e-9"
```

```
SETTINGS+="␣--nRecycle␣60"
```

Finding the domain size for a single ellipse in a viscous free stream, here with the domain size of 9 lengths behind the ellipse, which was chosen for follow-on simulations.

```
obstacle ellipse
    xpos      1.60
    ypos      3.25
    rx        0.6
    ry        0.1
    theta0    0.0

SETTINGS=""
SETTINGS+="␣--study␣fixed"
SETTINGS+="␣--bpdx␣50" % resolution of 154 ppl
SETTINGS+="␣--bpdy␣25" % set to 1/2 bpdx
SETTINGS+="␣--maxextent␣13.00" % changed between simulations
SETTINGS+="␣--safetyfactor␣0.7"
SETTINGS+="␣--tmax␣40.00"
SETTINGS+="␣--tprint␣1.00"
SETTINGS+="␣--tsave␣0.01"
SETTINGS+="␣--nu␣1.600e-3"
SETTINGS+="␣--Uinfx␣2.0"
SETTINGS+="␣--Uinfy␣0.0"
SETTINGS+="␣--freestream␣bump"
SETTINGS+="␣--Ubump␣0.0"
SETTINGS+="␣--Vbump␣0.5"
SETTINGS+="␣--Tbump␣1.2"
SETTINGS+="␣--Wbump␣1.0"
SETTINGS+="␣--bOutflow␣1"
SETTINGS+="␣--ramptime␣0.005"
SETTINGS+="␣--rampsize␣1e-3"
SETTINGS+="␣--tol␣1e-9"
```

```
SETTINGS+="␣-nRecycle␣60"
```

Factory and settings for the overtaking simulations, where relative motion was introduced between the ellipses inside of a viscous, constant-velocity flow with free boundaries. Here, the case of $(y^*, u_{rel}) = (0.30, 0.25)$ was simulated.

```
obstacle ellipse
    xpos      2.60 % constant position with respect to frame
    ypos      4.13 % centered in the vertical domain
    rx        0.6
    ry        0.1
    theta0    0.0


obstacle rampup_ellipse
    xpos     4.40 % position of ellipse at the start of the transient region
    ypos     3.77 % separation of y*=0.30, changed between simulations
    rx       0.6
    ry       0.1
    theta0   0.0
    Ubx      0.25 % additional velocity for Ellipse 1
    Uby      0.0
    wb       0.0
    T        3.00 % three seconds for ramp-up of ellipse velocity
    delay    20.00 % delay so that steady-state could be reached


SETTINGS=""
SETTINGS+=" --study moving"
SETTINGS+=" --bpdx 72"
SETTINGS+=" --bpdy 36"
SETTINGS+=" --maxextent 15.8"
SETTINGS+=" --safetyfactor 0.7"
SETTINGS+=" --tmax 37.4"
SETTINGS+=" --tprint 0.50"
```

```
SETTINGS+="␣-tsave␣0.01"
SETTINGS+="␣-nu␣8.000e-4"
SETTINGS+="␣-Uinfx␣1.0" % both ellipses moving forward
SETTINGS+="␣-Uinfy␣0.0"
SETTINGS+="␣-freestream␣bump"
SETTINGS+="␣-Ubump␣0.0"
SETTINGS+="␣-Vbump␣0.5"
SETTINGS+="␣-Tbump␣1.2"
SETTINGS+="␣-Wbump␣1.0"
SETTINGS+="␣-bOutflow␣1"
SETTINGS+="␣-ramptime␣0.005"
SETTINGS+="␣-rampsize␣1e-3"
SETTINGS+="␣-tol␣1e-9"
```

Appendix B

Overtaking Case Plots

Plots of all 16 cases of the overtaking simulations: Figure B-1 compares the results at different y^* when u_{rel} is kept constant, and Figure B-2 shows the results at different u_{rel} for a constant y^*.

Plots of all 20 cases of the overtaking-stationary simulations: Figure B-3 compares the results at different y^* when u_{rel} is kept constant, and Figure B-4 shows the results at different u_{rel} for a constant y^*.

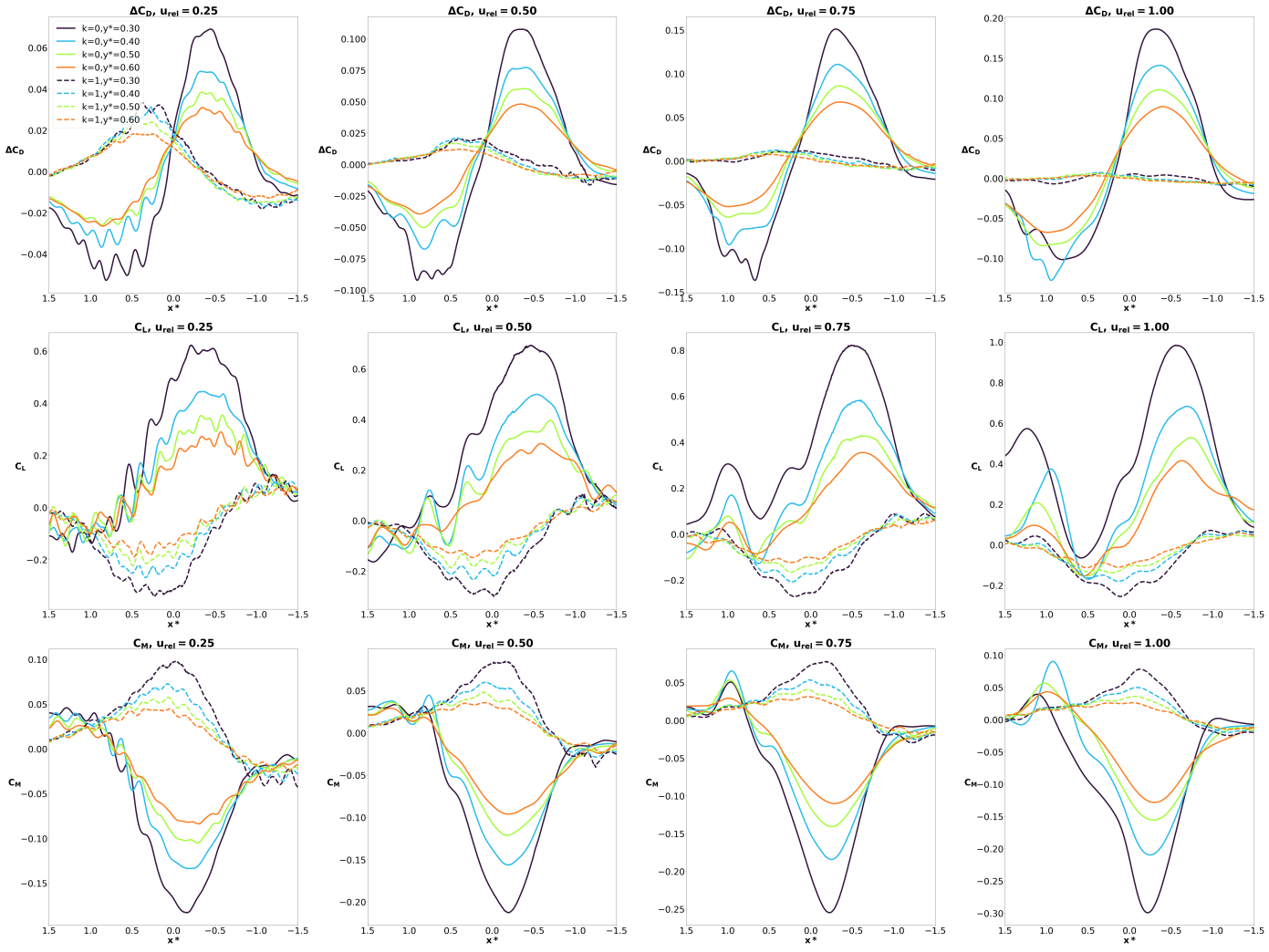

Figure B-1: Full overtaking simulation results with constant u_{rel}

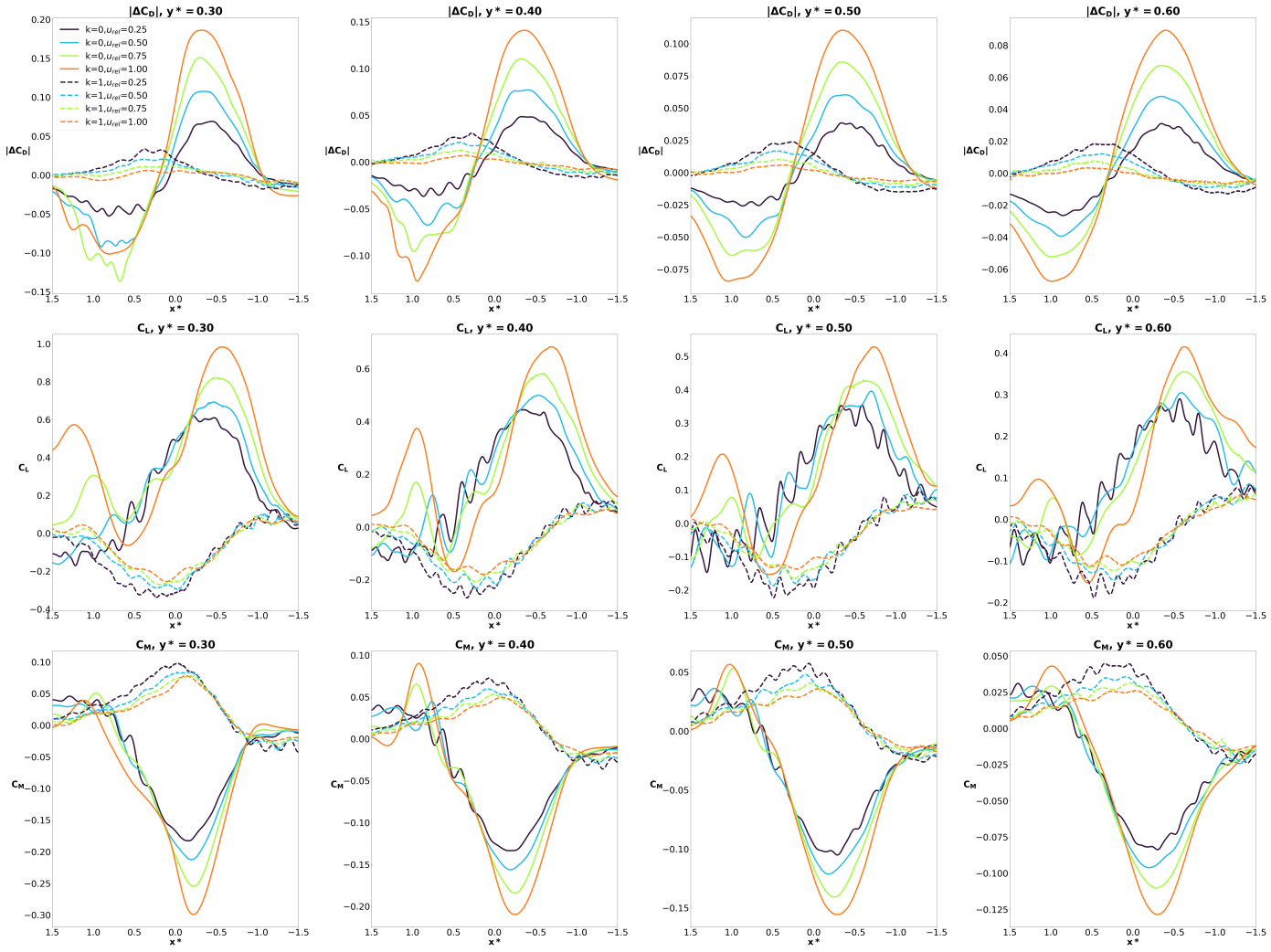

Figure B-2: Full overtaking simulation results with constant y^*

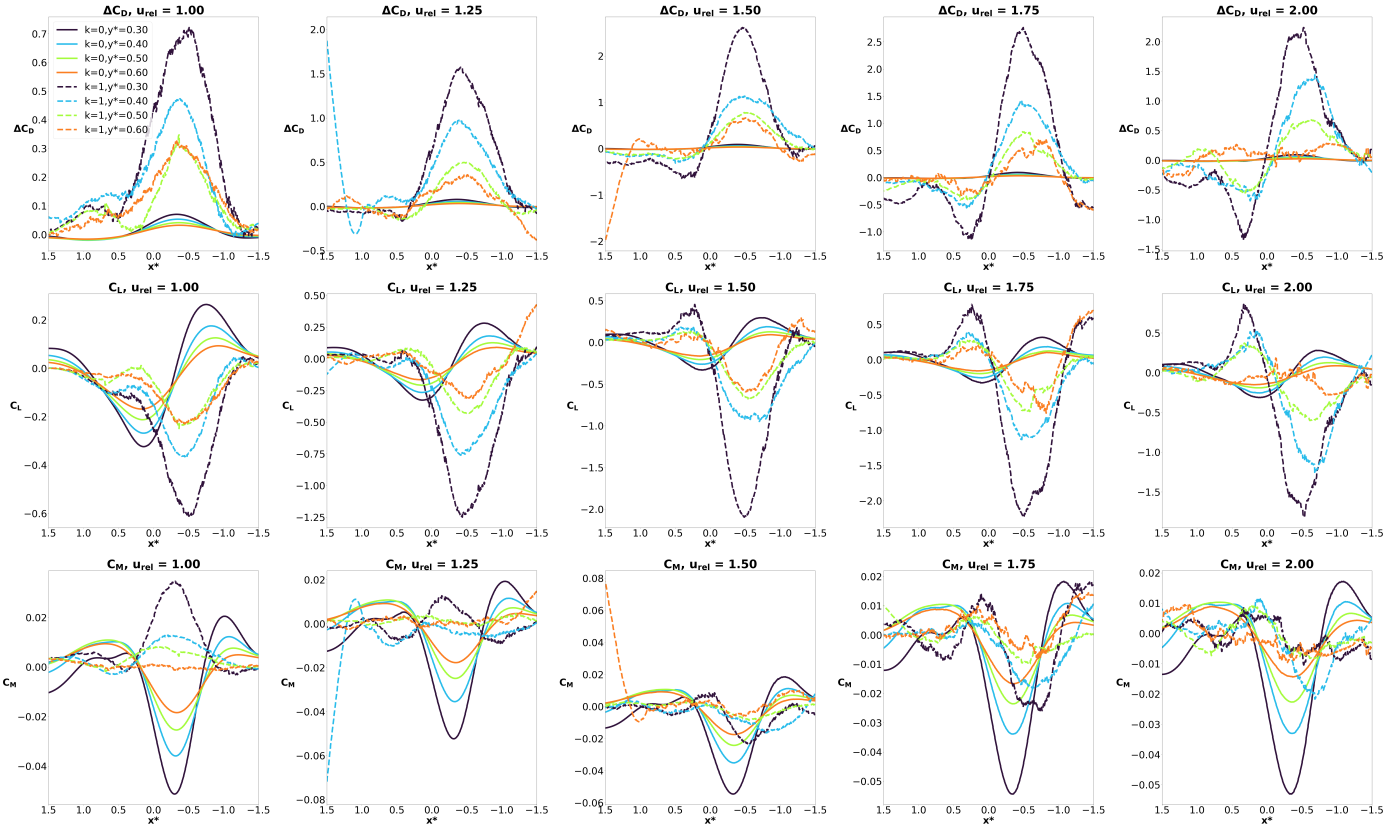

Figure B-3: Full overtaking-stationary simulation results with constant u_{rel}

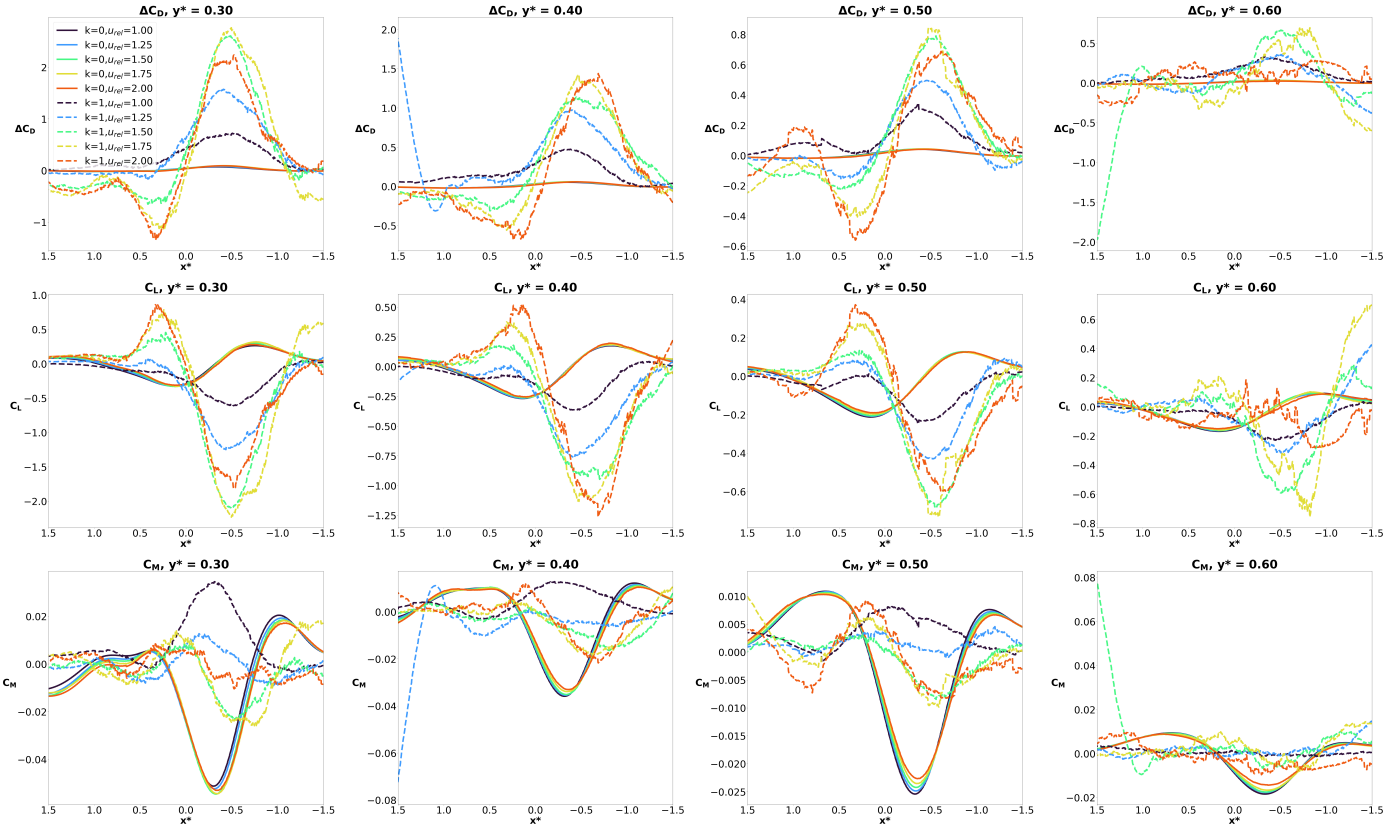

Figure B-4: Full overtaking-stationary simulation results with constant y^*